UNIVERSITÀ DEGLI STUDI DI NAPOLI 'FEDERICO II'

Scuola Politecnica e delle Scienze di Base

Ph.D. School in Chemical Sciences

XXXI – Cycle

Smart High-Throughput Experimentation

Antonio Vittoria

Supervisor: Assessor:

Prof. Vincenzo Busico   *Prof. Riccardo Tesser*

Ph.D. School Coordinator:

Prof. Luigi Paduano

2015-2018

Abstract

Chemistry in general is not an exact science. Chemical catalysis, moreover, is a purely kinetic phenomenon. This translates into the fact that discovering and even optimizing a catalyst for a desired application heavily relies on trial-and-error, and serendipitous advances are not rare.

This PhD project aimed to improve the effectiveness of a trial-and-error approach to olefin polymerization catalysis, one of the most important chemical technologies, by means of High Throughput Experimentation (HTE) methodologies. The project was hosted at the Laboratory of Stereoselective Polymerizations (LSP) of the Federico II University, which is world-leading in HTE catalyst screenings with optimization purposes, and sponsored by HTExplore srl, an academic spin-off of LSP delivering HTE services to polyolefin producers. The general objective was to introduce protocols for 'smart' applications of the existing HTE workflow of LSP to complex chemical problems in polyolefin catalysis. In particular, methods for the rapid and accurate determination of the Quantitative Structure-Activity Relationship (QSAR) of representative molecular or heterogeneous catalyst formulations were implemented as the basis for statistical modeling with predictive ability.

The HTE toolkit is the subject of **Chapter 2**. Due to the extensive miniaturization and robotic automation, a HTE platform is not a push-button setup, and a complete HTE workflow may include several platforms and a number of integrated analytical tools amenable to high-throughput operation, so as not to create bottlenecks. At several industrial laboratories throughput was admittedly traded for accuracy, and a comparatively coarse HTE screening is still followed by

finer evaluations with conventional methods in larger scale. LSP's choice was different, and major efforts were undertaken, also in the framework of this project, in order to bring the HTE workflow to the precision and accuracy of conventional tools, for the polymerization part as well as at the polymer characterization part.

Chapter 3 illustrates a systematic and thorough investigation of $MgCl_2$-supported Ziegler-Natta (ZN) catalyst systems, which monopolize the industrial production of isotactic polypropylene. These systems are complex formulations in which the catalytic phase, consisting of $TiCl_n$ species chemisorbed on nanostructured $MgCl_2$, is modulated by means of one or more organic electron donors co-adsorbed with the Ti compound(s) and playing a role similar to the ancillary ligands in molecular catalysts. The study was aimed to sort out the relationships between the composition of the precatalyst, that of the activated solid obtained by reacting the former with an Al-alkyl cocatalyst, and the *stereo*selectivity observed in the homopolymerization of propene in hydrocarbon slurry. The work was a collaboration with the research center of SABIC at Geleen (Netherlands), where applied mathematicians took care of the highly complex 'black-box' QSAR modeling part (out the scope of the present project, and therefore not included in the thesis).

Chapter 4 is dedicated to the quantitative determination of the *regio*selectivity for the aforementioned ZN catalysts. This question is extremely challenging, because the few regioirregular 2,1 enchainments of the monomer (less than 1‰) are difficult to detect by ^{13}C NMR, and at the same time of the utmost importance because they govern key aspects of polymerization kinetics such as 'dormancy' and response to H_2 as a chain transfer agent.

Chapter 5 deals with the optimization of C_2-symmetric bis(indenyl) *ansa*-zirconocene catalysts for applications in propene homopolymerization. This was part of a broader collaborative project with the research groups of Prof. Alexander Voskoboynikov at Moscow State University and Prof. Alceo Macchioni at the University of Perugia, sponsored by the Dutch Polymer Institute (DPI). The experimental QSAR database was used as the input of a simple 'black-box' QSAR model making use of a set of descriptors developed ad-hoc for organometallic catalysts. Such descriptors, quantifying relevant electronic and steric properties of the catalyst precursors and of plausible models of catalytically active species, were calculated by means of theoretical methods based on Density Functional

Theory (DFT), and turned out to be extremely effective, thus ending up with a very simple mathematical QSAR expression.

Chapter 6 demonstrates how HTE can also be addressed to unravel the molecular kinetics of highly complex *catalytic processes*. The synthesis of olefin block copolymers (OBC) by means of tandem catalysis under Coordinative Chain Transfer regime, also known as 'Chain Shuttling', was taken as a convenient case history. Disclosed more than 10 years ago by Dow Chemical, the process has become commercial, and its theoretical principles are well-understood. Yet, applying said principles to the details of specific cases is complicated; as a matter of fact, prior to our investigation average block lengths, numbers, and distributions thereof for commercial OBC grades were not available in the public domain. A systematic HTE exploration of the process variables space led rapidly to an unambiguous description of OBC microstructure and architecture, and an (ex-post) simple explanation of their physico-chemical properties.

The main conclusions of the project are presented in **Chapter 7**. In our opinion, it is unquestionable that smart HTE methodologies are eye-openers in the study of organometallic catalysis, and that – not surprisingly – many long-standing problems can be easily solved as soon as adequate experimental information becomes available. On the other hand, it is also fair to admit that not all problems can be addressed with the HTE workflow implemented at LSP. One example is the determination of the fraction of active metal in an organometallic catalyst, which is always lower than its analytical concentration. The final **Appendix** to the thesis is dedicated to a Chromophore Quench Labeling approach to said problem for one of the ZN catalysts discussed in Chapters 3 and 4. The experiments were carried out in the research group of Prof. Clark Landis (University of Wisconsin at Madison), during a 3-month stage. Apart from the intrinsic interest of the results, the topic is stimulating because it may represent a new frontier for HTE; indeed, the design of selective labels of growing and 'dormant' polymer chains for use in a HTE polymerization platform is a challenge that we are already considering to take in the near future.

Table of Contents

1. Scope, Objectives, and Layout of the Thesis

The general aim of this PhD project was the implementation of advanced methods for the heuristic exploration of industrially relevant olefin polymerization catalysts and processes by means of High Throughput Experimentation (HTE).

The vast majority of chemical and biochemical reactions, including those exploited in industry, are catalytic. A good catalyst is one which enhances by several orders of magnitude the rate of a *desired* reaction, which in most cases means that some kind of *selectivity* is required. An extreme case are *enantio*selective reactions, hugely important in the pharma industry; on the other hand, the quest for *chemo*selective, *regio*selective and/or *stereo*selective catalysts is widespread in chemistry in general.

Whereas the definition of catalysis is univocal, the working principles are differentiated. In this project the focus was on organometallic species of transition elements, used ubiquitously in industrial organic chemistry to activate unsaturated molecules such as e.g. olefins in a variety of processes including hydrogenation, hydroformylation, metathesis, polymerization and a number of isomerizations. The substrate(s) are π-acidic electron donors which bind to a coordinatively unsaturated transition metal center (M) and undergo activation by back-donation and/or charge separation(s) at the active site (typically a M-C or M-H σ-bond). The inherent reactivity of M is modulated by electronic and steric

effects, and in principle can be tailored to a desired application by optimizing the ancillary ligand frame of a molecular catalyst, or the local environment of the active surface(s) in a heterogeneous catalyst by means of proper adsorbates. Unfortunately, catalyst *design* (meaning the rational implementation of a novel catalytic species with a desired performance) is not yet at hands; as a matter of fact, many claims of successful achievements in the scientific literature have rather been shown to be ex-post re-visitations of serendipitous discoveries.

One reason is that, even for simple molecular catalysts operating in homogeneous phase, the catalytic cycle only represents a small part of the overall chemistry going on in the system. A good example is olefin hydrogenation mediated by Rh-based catalysts. The initial discovery that $(PPh_3)_3RhCl$ (Ph = Phenyl) in methanol solution can change into a competent catalyst for the hydrogenation of alkenes was made by Wilkinson[1,2] long before the many simultaneous equilibria of Figure 1.1 were recognized and thoroughly elucidated by Halpern.[3] Ironically, one of the conclusions of this later study was that the contamination of the system by O_2 favors the generation of the active species **2** from the precursor **1** due to the oxidation of PPh_3 to $OPPh_3$; in fact, this led Wilkinson to largely overestimate k_1 in Figure 1.1.

Quantitative studies like that in Figure 1.1 are rare. As a matter of fact they are only possible when the catalytic species is a well-defined molecular entity, and its functioning is (or can be made) slow enough (say, Turn Over Frequency (TOF) ≈ 1 s^{-1} or below) to intercept and characterize all reactive intermediates, as well as 'dormant' and inactive species. With few exceptions, industrially relevant catalysts for large-volume applications feature much larger TOF values ($>10^3$ s^{-1}), but even with 'slow' catalysts of interest for fine chemistry key aspects of the inner working can be difficult or impossible to trace.
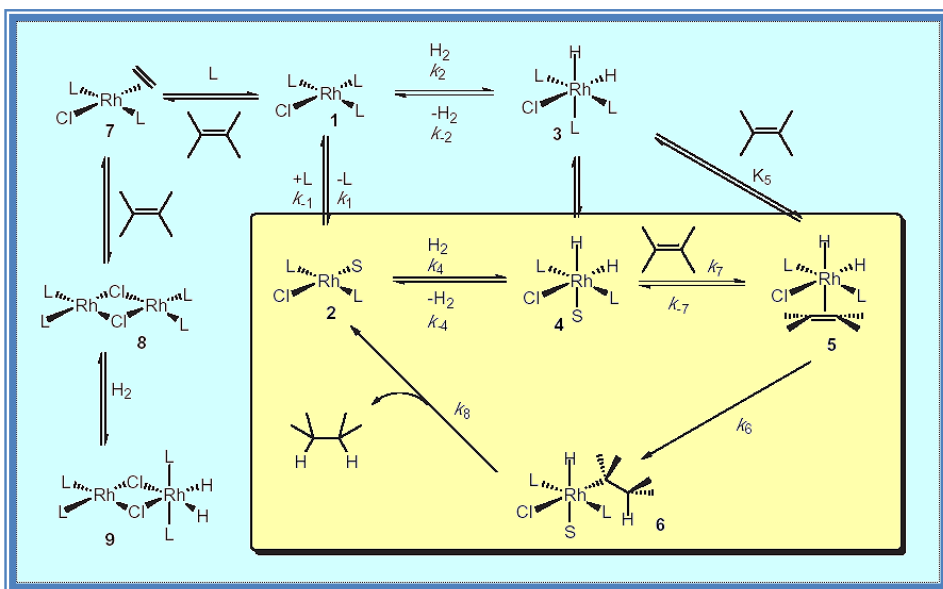
Figure 1.1. The chemistry of and around catalytic alkene hydrogenation with Wilkinson's catalyst (L = triphenylphosphine; S = methanol). The catalytic cycle is included in the yellow box. All specific rates indicated in the figure have been quantified.[3]

Another example taken from Rh-based catalysis is the chiral homologue of Wilkinson's catalyst shown in Figure 1.2, disclosed by Knowles for the enantioselective synthesis of L-DOPA (the first enantiopure drug for the treatment of Parkinson's disease) by asymmetric hydrogenation of methyl acetamidocinnamate (MAC).[4,5]

All key intermediates in the two competing diastereoisomeric hydrogenation cycles (Figure 1.3) have been identified, and the overall mechanism is now very well-understood.[6,7] Yet, the exact steric contacts between the prochiral substrate and the chiral ancillary ligand framework of the Rh center responsible for the measured enantiomeric excess (e.e. = 94%) in the rate-limiting transition state (TS) remain unknown. In fact, the experimental $\Delta\Delta G^{\#}$ of $\approx$2 Kcal mol^{-1} results from a summation of several non-bonded interactions in the Rh coordination sphere, each of which is well-below the error bar of state-of-the-art Quantum Mechanics (QM) modeling calculations ($\pm$2 Kcal mol^{-1}). This is not an isolated case.
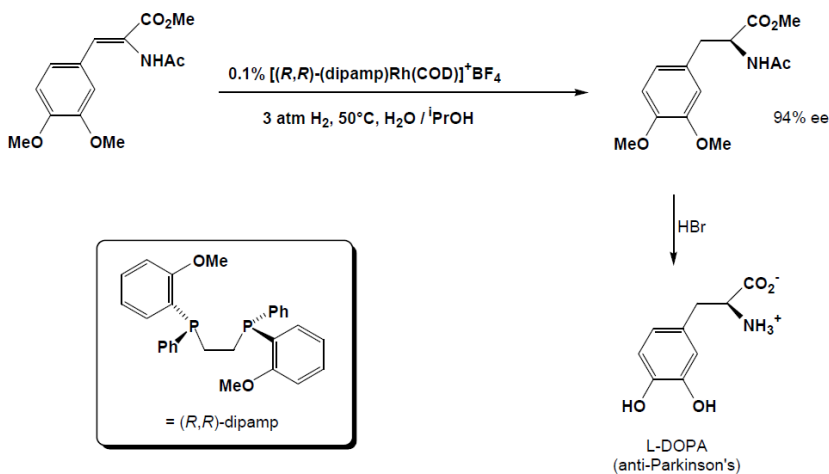
Figure 1.2. The enantioselective synthesis of L-DOPA by asymmetric hydrogenation of MAC mediated by Rh(DiPAMP).
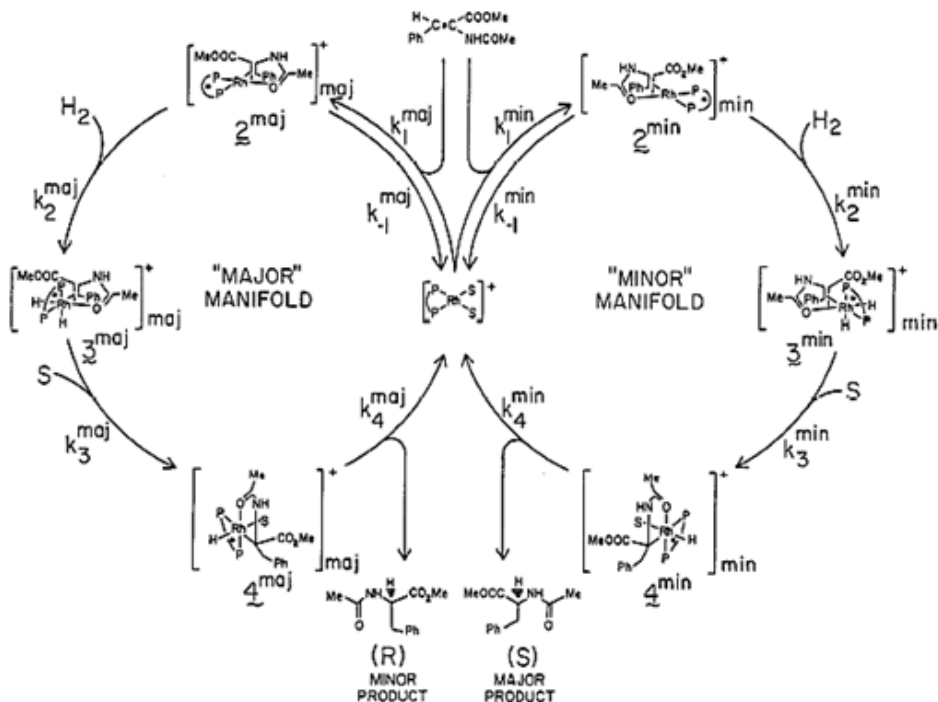
Figure 1.3. The competing diastereomeric cycles of the asymmetric hydrogenation of methyl Z-acetoamidocinnamate with Rh(DIPAMP).

With heterogeneous catalysts, whose active species are transition metal atoms exposed on the surface of defective crystallites, the challenge is further complicated by the ill-defined nature of the active centers.

All this considered, it cannot be surprising that practically all known selective catalysts have been discovered by means of trial-and-error or – even – serendipitously, and catalyst research in an industrial environment entails the fast exploration of the variables space so as to locate a convenient solution for the problem of interest, with scientific understanding playing a very limited role. The ability to perform a large number of reliable experiments in a short time with some kind of parallelization is key to this strategy. Until the end of the last millennium, the experimentation was carried out in conventional batch or semi-batch reactors by human operators. More recently, the advent of process automation has led to a so-called High Throughput Experimentation (HTE) approach, that is one in which highly miniaturized reactors are operated in parallel or rapid-sequence mode by robots. Typical HTE platforms can run 10^2-10^4 experiments per day with working volumes of a few mL or even less.[8]

Two severe drawbacks of HTE are technical complexity and high investment and operating costs. Until now, this has limited diffusion to large chemical companies; among these, polyolefin producers have been pioneers,[9,10] which can be easily understood in view of the gigantic scale of their market (Figure 1.4).
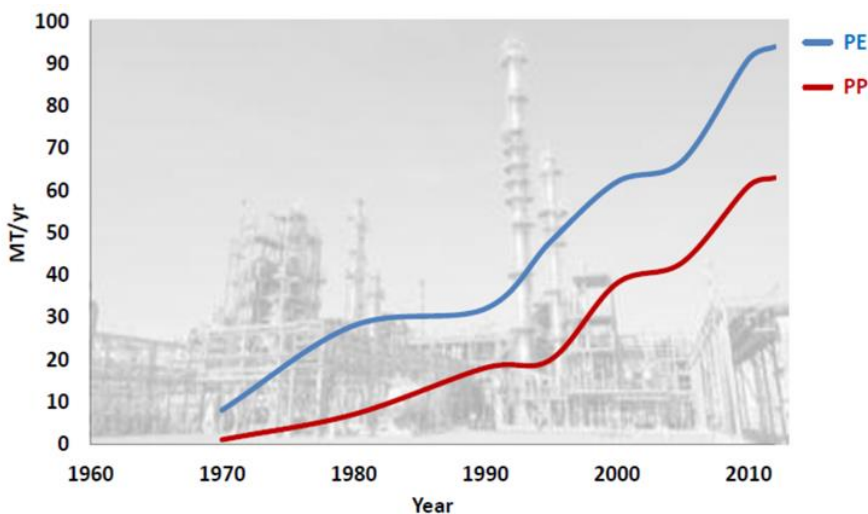
Figure 1.4. The global market of polyethylene (PE) and polypropylene (PP).

Early applications were mainly targeted to catalyst *discovery*. A seminal workflow implemented in the late 1990s by Symyx Technologies and Dow Chemical in the framework of a strategic alliance is shown in Figure 1.5.[9,10] A comparatively coarse 'primary' screening of large libraries of candidate systems ($\approx 10^3$ experiments per day, ≈ 1 mL working volume per experiment) was followed by the structural amplification of 'hits' and a finer 'secondary' screening for the identification of 'leads' ($\approx 10^2$ experiments per day, ≈ 10 mL working volume per experiment). The final structural amplification and optimization of 'leads' was carried out with conventional methods.
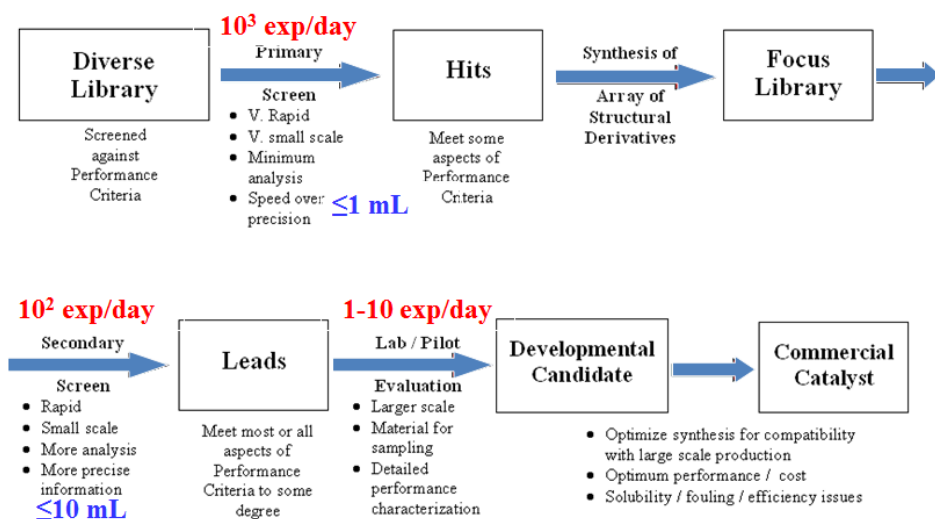
Figure 1.5. The HTE workflow for polyolefin catalyst discovery implemented by Symyx Technologies and Dow Chemical.

This strategy turned out to be effective (as a matter of fact, Dow Chemical has vastly innovated its catalyst portfolio in the last two decades), but also highly resource-intensive, particularly in the substantially 'blind' primary screening stage.

Despite the apparent simplicity of the poly-insertion reaction, the chemistry of catalytic olefin polymerization can also be extremely complicated. Just as an example, on inspection of Figure 1.6 it is easy to capture the similarity between the case of propene polymerization mediated by metallocene catalysts and that of alkene hydrogenation illustrated in Figure 1.1. On the other hand, even at very low temperature competent olefin polymerization catalysts have TOF values $>10^3$

s^{-1}, and classical studies like those previously discussed in relation with Figures 1.1 and 1.3 are unfeasible. This hampers a deterministic approach not only to catalyst discovery, but also to the seemingly simpler task of catalyst *optimization*.
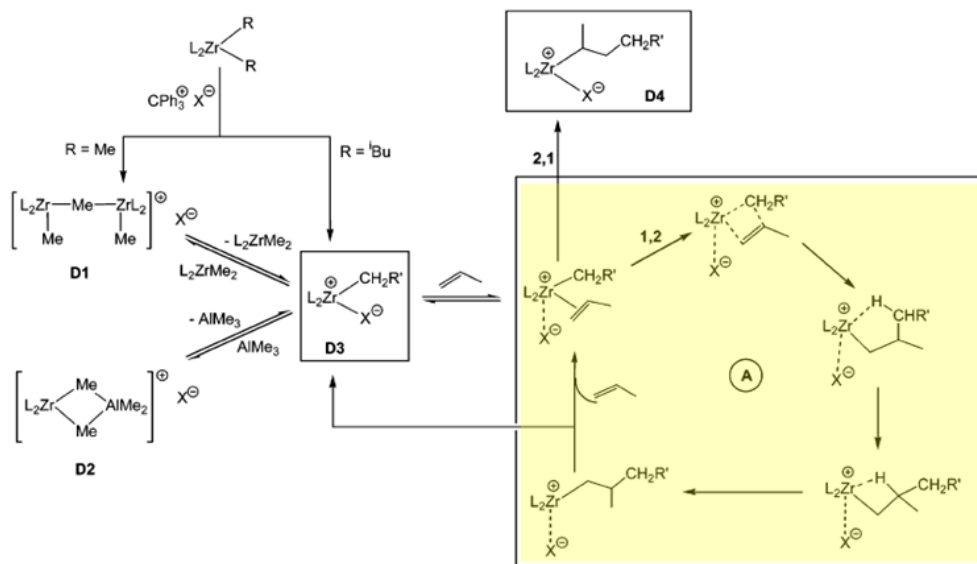
Figure 1.6. The chemistry of and around catalytic propene polymerization with a metallocene catalyst (L = e.g. h^5-cyclopentadienyl). The catalytic cycle is included in the yellow box. D1-D4 species are all 'dormant'.

A possible strategy is to utilize experimental Quantitative Structure-Activity Relations (QSAR) databases as input for statistical models with predictive ability (Figure 1.7). Like other regression models, QSAR regression models relate a set of 'predictor' variables (X) to the potency of the response variable (Y). The predictors consist of physico-chemical properties or theoretical molecular descriptors of chemicals; the response variable, in turn, typically is some kind of activity of the chemicals. When physico-chemical properties or structures are expressed by numbers, one can find a mathematical relationship between them and the response variable, that is the QSAR. After a proper validation, said mathematical expression can be used to predict the response of other chemical structures, provided that the applicability domain is accurately verified.
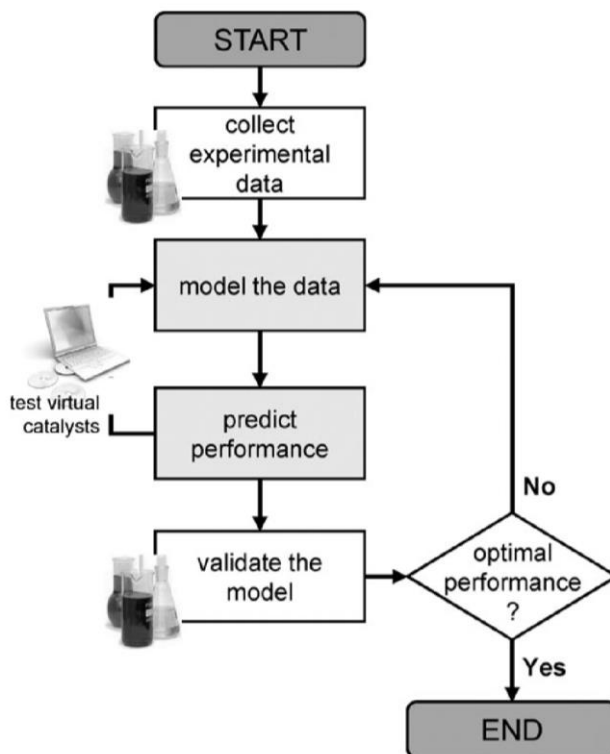
Figure 1.7. Typical layout of a combined experimental/computational QSAR HTE workflow for catalyst optimization.[11]

It is worthy to note at this point that QSAR models can be of 'black-box' or 'clear-box' type. The former belong in the wider class of 'Black-Boxes', representing any device, system, model, process or object which converts a series of input into one or more outputs with no knowledge of its internal workings. In the absence of a thorough knowledge/understanding of the system to be investigated, which is often the case with organometallic catalysts as was discussed before, this type of models relying on an empirical/statistical basis represents the only viable option. The mathematical QSAR expression of a 'black-box' model is usually very complex, because a large set of generic descriptors is necessary to reproduce the experimental data. Therefore, it is mandatory to build, train and validate the model on a correspondingly large database, so as to reduce the error and avoid overfitting. With a proper design, HTE tools and methods are ideally suited to address this question.

The Laboratory of Stereoselective Polymerizations (LSP) of the Federico II University, in association with its academic spin-off HTExplore s.r.l., is one of the

very few academic groups operating comprehensive HTE workflows for organometallic catalysis. In particular, LSP pioneered the application of integrated experimental/computational HTE methodologies for catalyst optimization studies. In the framework of long-term collaborations with leading HTE tool manufacturers (Symyx Technologies) and polyolefin producers (Dow Chemical, SABIC), the LSP Team demonstrated that state-of-the-art secondary screening platforms can be utilized to work out the kinetic behavior of molecular and heterogeneous olefin polymerization catalysts with up to a 10^2-fold throughput intensification compared with conventional bench reactors, without trading for precision and accuracy. Integration with high-end polymer characterization tools amenable to operation in high-throughput mode, such as Gel Permeation Chromatography (GPC), analytical Crystallization Elution Fractionation (A-CEF), and high-temperature cryoprobe NMR spectroscopy, led to the first HTE workflow for the rapid buildup of high-quality QSAR databases in polyolefin catalysis. The approach covers the polymer knowledge and value chains from catalytic synthesis down to full microstructural assessment, and can be utilized to develop predictive QSAR models (Figure 1.8).
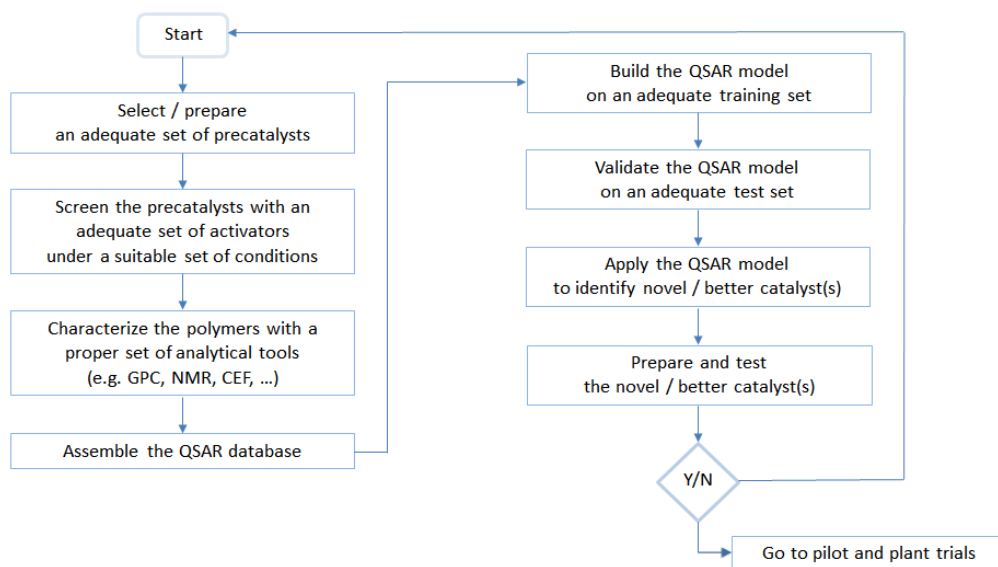
Figure 1.8. The proprietary polyolefin HTE workflow at LSP/HTExplore.

The main goal of the present PhD project, that was funded by HTExplore and hosted at LSP, is the implementation of 'smart' HTE protocols for catalyst optimization programs. The various chapters of the Thesis explain how this general objective was achieved for several classes of olefin polymerization catalysts.

The HTE toolkit is the subject of **Chapter 2**. Due to the extensive miniaturization and robotic automation, a HTE platform is not a push-button setup, and a complete HTE workflow may include several platforms and a number of integrated analytical tools amenable to high-throughput operation, so as not to create bottlenecks. At several industrial laboratories throughput was admittedly traded for accuracy, and a comparatively coarse HTE screening is still followed by finer evaluations with conventional methods in larger scale. LSP's choice was different, and major efforts were undertaken in order to bring the HTE workflow to the precision and accuracy of conventional tools, for the polymerization part as well as at the polymer characterization part. The present project contributed to achieve further advances in this respect.

Chapter 3 illustrates a systematic and thorough investigation of $MgCl_2$-supported Ziegler-Natta (ZN) catalyst systems, which monopolize the industrial production of isotactic polypropylene. These systems are complex formulations in which the catalytic phase, consisting of $TiCl_n$ species chemisorbed on nanostructured $MgCl_2$, is modulated by means of one or more organic electron donors co-adsorbed with the Ti compound(s) and playing a role similar to the ancillary ligands in molecular catalysts. The study was aimed to sort out the relationships between the composition of the precatalyst, that of the activated solid obtained by reacting the former with an Al-alkyl cocatalyst, and the *stereo*selectivity observed in the homopolymerization of propene in hydrocarbon slurry. The study was performed in collaboration with the research center of SABIC at Geleen (Netherlands), where applied mathematicians took care of the highly complex 'black-box' QSAR modeling part (out the scope of the present project, and therefore not included in the thesis).

Chapter 4 is dedicated to the quantitative determination of the *regio*selectivity for the aforementioned ZN catalysts. This question is extremely challenging, because the few regioirregular 2,1 enchainments of the monomer (less than 1‰) are difficult to detect by ^{13}C NMR, and at the same time of the utmost importance because they govern key aspects of polymerization kinetics such as 'dormancy' and response to H_2 as a chain transfer agent.

Chapter 5 deals with the optimization of C_2-symmetric bis(indenyl) *ansa*-zirconocene catalysts for applications in propene homopolymerization. The study was part of a broader collaborative project with the research groups of Prof. Alexander Voskoboynikov at Moscow State University and Prof. Alceo Macchioni at the University of Perugia, sponsored by the Dutch Polymer Institute (DPI). The experimental QSAR database was used as the input of a simple 'black-box' QSAR model making use of a set of descriptors developed ad-hoc for organometallic catalysts. Such descriptors, quantifying relevant electronic and steric properties of the catalyst precursors and of plausible models of catalytically active species, were calculated by means of theoretical methods based on Density Functional Theory (DFT), and turned out to be extremely effective, thus ending up with a very simple mathematical QSAR expression.

Chapter 6 demonstrates how HTE can also be addressed to unravel the molecular kinetics of highly complex *catalytic processes*. The synthesis of olefin block copolymers (OBC) by means of tandem catalysis under Coordinative Chain Transfer regime, also known as 'Chain Shuttling', was taken as a convenient case history. Disclosed more than 10 years ago by Dow Chemical, the process has become commercial, and its theoretical principles are well-understood. Yet, applying said principles to the details of specific cases is complicated; as a matter of fact, prior to our investigation average block lengths, numbers, and distributions thereof for commercial OBC grades were not available in the public domain. A systematic HTE exploration of the process variables space led rapidly to an unambiguous description of OBC microstructure and architecture, and an (ex-post) simple explanation of their physico-chemical properties.

The main conclusions of the project are presented in **Chapter 7**. In our opinion, it is unquestionable that smart HTE methodologies are eye-openers in the study of organometallic catalysis, and many long-standing problems turn out to be easy to solve as soon as adequate experimental information becomes available. On the other hand, it is also fair to admit that not all problems can be addressed with the HTE workflow implemented at LSP. One example is the determination of the fraction of active metal in an organometallic catalyst, which is always lower than its analytical concentration (Figures 1.1 and 1.6). The final **Appendix** to the thesis is dedicated to a Chromophore Quench Labeling approach to said problem for one of the ZN catalysts discussed in Chapters 3 and 4. The experiments were carried out in the research group of Prof. Clark Landis (University of Wisconsin at Madison), during a 3-month stage. Apart from the intrinsic interest of the results,

the topic is stimulating because it may represent a new frontier for HTE; indeed, the design of selective labels of growing and 'dormant' polymer chains for use in a HTE polymerization platform is a challenge that we are already considering to take in the near future.

Parts of this thesis have already being published[12–15], or are ready for submission.[16–18]

References

(1)   Young, J. F.; Osborn, J. A.; Jardine, F. H.; Wilkinson, G. Hydride Intermediates in Homogeneous Hydrogenation Reactions of Olefins and Acetylenes Using Rhodium Catalysts. *Chem. Commun.* **1965**, No. 7, 131. https://doi.org/10.1039/C19650000131.

(2)   Osborn, J. A.; Jardine, F. H.; Young, J. F.; Wilkinson, G. The Preparation and Properties of Tris(Triphenylphosphine)Halogenorhodium(I) and Some Reactions Thereof Including Catalytic Homogeneous Hydrogenation of Olefins and Acetylenes and Their Derivatives. *J. Chem. Soc. A Inorganic, Phys. Theor.* **1966**, *566* (1966), 1711. https://doi.org/10.1039/j19660001711.

(3)   Halpern, J. Mechanistic Aspects of Homogeneous Catalytic Hydrogenation and Related Processes. *Inorganica Chim. Acta* **1981**, *50*, 11–19. https://doi.org/10.1016/S0020-1693(00)83716-0.

(4)   Vineyard, B. D.; Knowles, W. S.; Sabacky, M. J.; Bachman, G. L.; Weinkauff, D. J. Asymmetric Hydrogenation. Rhodium Chiral Bisphosphine Catalyst. *J. Am. Chem. Soc.* **1977**, *99* (18), 5946–5952. https://doi.org/10.1021/ja00460a018.

(5)   Knowles, W. S. Asymmetric Hydrogenation. *Acc. Chem. Res.* **1983**, *16* (3), 106–112. https://doi.org/10.1021/ar00087a006.

(6)   Gridnev, I. D.; Imamoto, T. On the Mechanism of Stereoselection in Rh-Catalyzed Asymmetric Hydrogenation: A General Approach for Predicting the Sense of Enantioselectivity. *Acc. Chem. Res.* **2004**, *37* (9), 633–644. https://doi.org/10.1021/ar030156e.

(7)   Noyori, R.; Yamakawa, M.; Hashiguchi, S. Metal–Ligand Bifunctional Catalysis: A Nonclassical Mechanism for Asymmetric Hydrogen Transfer between Alcohols and Carbonyl Compounds. *J. Org. Chem.* **2001**, *66* (24), 7931–7944. https://doi.org/10.1021/jo010721w.

(8)   *High-Throughput Screening in Heterogeneous Catalysis*; Hagmeyer, A., Strasser, P., Volpe, A. F., Eds.; Wiley-VCH Verlag GmbH & Co. KGaA: Weinheim, FRG, 2004. https://doi.org/10.1002/3527604103.

(9)   Peil, K. P.; Neithamer, D. R.; Patrick, D. W.; Wilson, B. E.; Tucker, C. J. Applications of High Throughput Research at the Dow Chemical Company. *Macromol. Rapid Commun.* **2004**, *25* (1), 119–126. https://doi.org/10.1002/marc.200300160.

(10)   Chum, P. S.; Swogger, K. W. Olefin Polymer Technologies-History and Recent Progress at The Dow Chemical Company. *Prog. Polym. Sci.* **2008**, *33* (8), 797–819. https://doi.org/10.1016/j.progpolymsci.2008.05.003.

(11)   Maldonado, A. G.; Rothenberg, G. Predictive Modeling in Homogeneous Catalysis : A Tutorial W. **2010**, 1891–1902. https://doi.org/10.1039/b921393g.

(12)   Vittoria, A.; Meppelder, A.; Friederichs, N.; Busico, V.; Cipullo, R. Demystifying Ziegler-Natta Catalysts: The Origin of Stereoselectivity. *ACS Catal.* **2017**, *7* (7), 4509–4518. https://doi.org/10.1021/acscatal.7b01232.

(13)   Zaccaria, F.; Vittoria, A.; Correa, A.; Ehm, C.; Budzelaar, P. H. M.; Busico, V.; Cipullo, R. Internal Donors in Ziegler-Natta Systems: Is Reduction by AlR_3 a Requirement for Donor Clean-Up? *ChemCatChem* **2018**, *10* (5), 984–988.

https://doi.org/10.1002/cctc.201701422.

(14)   Ehm, C.; Vittoria, A.; Goryunov, G. P.; Kulyabin, P. S.; Budzelaar, P. H. M.; Voskoboynikov, A. Z.; Busico, V.; Uborsky, D. V; Cipullo, R. Connection of Stereoselectivity, Regioselectivity, and Molecular Weight Capability in *rac*-R′$_2$Si(2-Me-4-R-Indenyl)$_2$ZrCl$_2$ Type Catalysts. *Macromolecules* **2018**. https://doi.org/10.1021/acs.macromol.8b01546.

(15)   Vittoria, A.; Busico, V.; Cannavacciuolo, F. D.; Cipullo, R. Molecular Kinetic Study of "Chain Shuttling" Olefin Copolymerization. *ACS Catal.* **2018**, *8* (6), 5051–5061. https://doi.org/10.1021/acscatal.8b00841.

(16)   Cipullo, R.; Busico, V.; Vittoria, A. Stereoselectivity of Regioirregular 2,1 Insertion in Ziegler-Natta Propene Polymerization Catalysis. To be submitted.

(17)   Vittoria, A.; Busico, V.; Cipullo, R. A HTE Protocol for Regioselectivity Measurements in Ziegler-Natta Propene Polymerization Catalysis. To be submitted.

(18)   Cipullo, R.; Meppelder, A.; Friederichs, N.; Busico, V.; Vittoria, A. Demystifying Ziegler-Natta Catalysts: Regioselectivity and Hydrogen Response. To be submitted.

2. The Integrated HTE Polyolefin Workflow

2.1. Introduction

The first applications of HTE in polyolefin catalysis date back to the late 1990s. As was noted in Chapter 1, the leading workflow was developed in collaboration by Symyx Technologies and Dow Chemical, with the aim to accelerate catalyst *discovery*.[1] To this end, the strategy was to carry out a very large number of polymerization experiments in a suitably small scale and rapid sequence mode under robotic control, with the ability to assess in semi-quantitative fashion catalyst productivity and, to some extent, polymer composition and microstructure without introducing bottlenecks. With reference to Figure 1.5, in the primary screening phase an easy-to-handle liquid olefin (namely 1-octene) was polymerized in large arrays of small glass vials (0.25 mL working volume), and catalytic activity was estimated by spotting the released reaction heat with IR sensors. Highly active catalysts ('hits') were moved to the secondary screening phase, where ethene or propene were homopolymerized or copolymerized under pressure with 1-octene in arrays of 48 or 96 mini-reactors (5-6 mL working volume each), and the polymers characterized by means of Rapid-GPC for average molecular weight (MW) and molecular weight distribution (MWD), and IR on cast films for composition (ethene/1-octene copolymers) or stereoregularity

(polypropylene). Catalysts yielding polymers with interesting properties ('leads') where then moved on to a conventional optimization stage.

The LSP researchers were exposed to the Symyx/Dow approach in the framework of collaborations with both companies. They noted that the secondary screening platform (Symyx Parallel Pressure Reactor, PPR48) was amenable to a conceptually different utilization, that is the rapid exploration of catalyst and polymer variables hyperspaces aimed to assemble comprehensive QSAR databases of use in HTE catalyst *optimization* cycles under the guidance of an appropriate statistical model. To this end, they integrated off-line a PPR48 setup with an array of high-end polymer characterization tools compatible with high-throughput operation, including Gel Permeation Chromatography (GPC, to measure MW and MWD), automatic Crystallization Elution Fractionation (CEF, to measure the distribution of crystallinity), and ^{1}H and ^{13}C NMR (for a full assessment of the microstructure). This challenge, undertaken in the late 2000s, took several years and a structural collaboration with the technology staff of HTExplore.

The present PhD project contributed to the success of the endeavor by implementing, benchmarking and validating 'smart' HTE protocols for the application of the comprehensive HTE workflow to several different olefin polymerization catalysts and processes of industrial interest.

This Chapter is a compact description of the polyolefin (PO) workflow operating at LSP/HTExplore. It may be worthy to note that such a workflow represents the current state-of-the-art worldwide. A list of the HTE platforms and off-line integrated tools is given in Table 2.1. The main technical features and representative protocols are illustrated in the following sections. In particular, Section 2.2 introduces the olefin polymerization workflow configuration (taking the homopolymerization of propene as a convenient example), whereas Section 2.3 is dedicated to the (pre)catalyst activation workflow configuration.

2.2. The 'Olefin Polymerization' workflow configuration

The main platforms and units in this workflow are listed in Table 2.1.

Table 2.1. List of the main HTE platforms and off-line integrated tools in the workflow.

Part/Function	Unit Operation	Platform/Analytical Tool
Catalyst Screening	Taring/Weighing	Mettler-Toledo Bodhan Balance Automator
	Olefin Polymerization	Freeslate PPR48
	Polymer Drying	Genevac EZ-2 Plus Drying Station
		Martin Christ RVC 2-33 CDplus [2x]
Polymer Characterization	GPC Analysis	Freeslate Rapid GPC
	Crystallization Elution Fractionation	Polymer Char A-CEF [2x]
	$^1H/^{13}C$ NMR Analysis	Bruker Avance III 400 spectrometer with high-temperature cryoprobe and robotic pre-heated sample changer
	Parallel Computation	Cluster of Intel Xeon Processor (256 cpu's)

2.2.1. Freeslate Parallel Pressure Reactor (PPR48)

All olefin polymerization experiments of this project were carried out using a robotically operated Freeslate (former Symyx) parallel pressure reactor (PPR) setup[2,3], featuring 48 reaction cells (each of 5-6 mL working volume), with individual on-line control, arrayed in six 8-cell modules integrally contained in a glovebox environment (Figure 2.1). Each module can be operated between 40 and 200°C (±0.1°C), and 20 and 495 psi (±1 psi), with efficient magnetically coupled mechanical stirring (up to 800 rpm). Solution or slurry polymerization reactions are run in semi-continuous mode. Two Vortex stir plates (800 rpm), each fitted with a rack for 6×8 1.2 mL vials or 2×5 8.0 mL vials, accommodate the catalyst system components (e.g. precatalysts, cocatalysts, activators, modifiers, scavengers, etc) which can be pre-contacted at the glove-box temperature (25°C). The injection system consists of a dual-arm robot adopting different technologies for catalyst solutions and slurries, with specialized needles and injectors. The slurry needle, in particular, is designed so as to penetrate the gas cap of the

reaction cells and dispense the catalyst slurry directly into the liquid phase (Figure 2.2); this ensures a highly accurate and precise dosing. Solvents, diluents and monomers are fed through syringe pumps (liquids) or direct lines with solenoid valves plumbed to the individual cells (gases).

The PPR software enables the operator to change the Design of Experiment (DoE) of the planned set of 48 polymerization experiments ('Library') during execution. To take full advantage of this option a rapid-sequence injection mode was adopted with a delay between consecutive catalyst injections long enough to assess the early phases of each experiment before launching the following one. A detailed illustration of the software package and commands was reported before.[4]
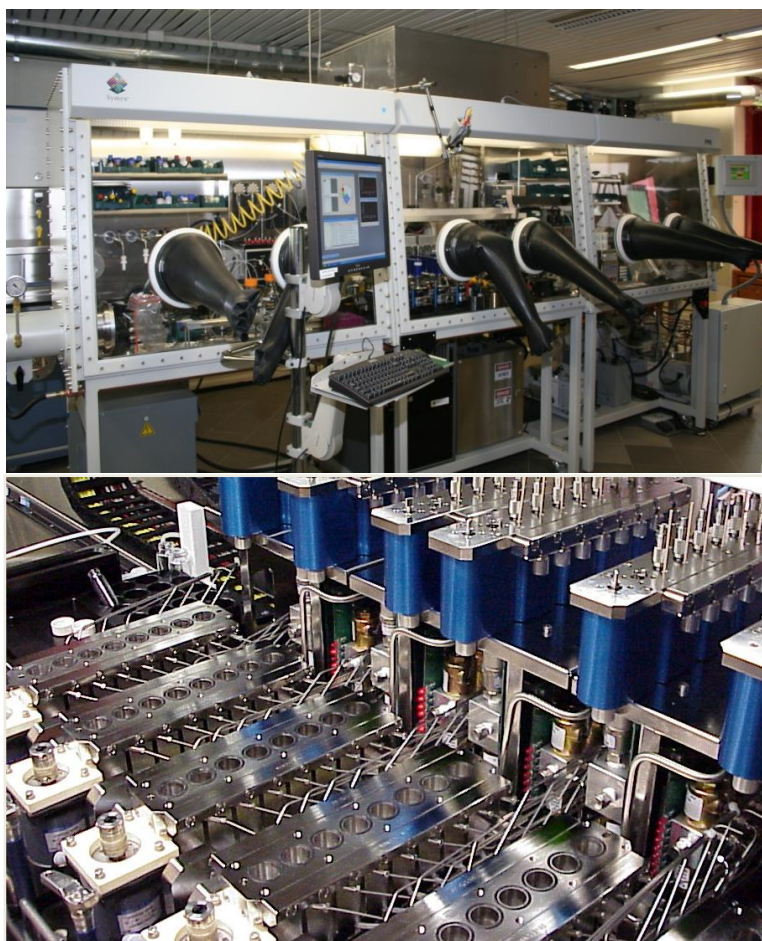
Figure 2.1. Overall view of the Freeslate PPR48 setup (top), and close-up of the 6 reaction modules with the 48 mini-reactors (bottom).
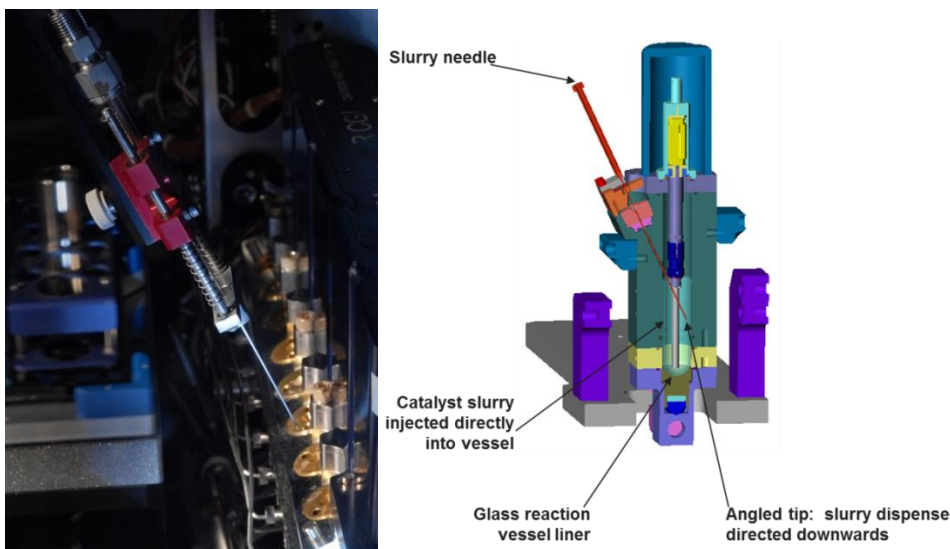
Figure 2.2. Close-up of the PPR slurry injection needle (left), and schematics of needle and injector port (right).

2.2.2. Polymerization protocols

In this section we describe the optimized operating protocol for propene homopolymerization, as a convenient example. Adaptations to different cases will be highlighted in the following chapters.

Prior to the execution of a library, the PPR modules undergo 'bake-and-purge' cycles overnight (8 h at 90-140°C with intermittent dry N_2 flow), to remove any contaminants and left-overs from previous experiments. After cooling to glove-box temperature, the module stir tops are taken off, and the 48 cells are fitted with disposable 10 mL glass inserts (pre-weighed in a Mettler-Toledo Bohdan Balance Automator) and polyether ether ketone (PEEK) stir paddles. The stir tops are then set back in place, and the cells are loaded with the appropriate amounts of (a) heptane diluent, (b) AlEt$_3$ (TEA) scavenger, and (c) H$_2$ (used as a chain transfer agent to control polymer molecular weight), thermostated at the desired temperature, and brought to the operating pressure with propene. At this point, the catalyst injection sequence is started; aliquots of (a) a heptane 'chaser', (b) a solution of TEA/alkoxysilane cocatalyst in heptane (pre-contacted in a 1.2 mL glass vial for 1.5 min), (c) a slurry of the precatalyst and (d) a heptane 'buffer', all

separated by nitrogen gaps, are uploaded into the slurry needle and subsequently injected into the cell of destination, thus starting the reaction. This is left to proceed under stirring (800 rpm) at constant temperature and pressure with continuous feed of propene on demand for a desired time (usually 30 or 60 min), and quenched by over-pressurizing the cell with 50 psi (3.4 bar) of dry air (preferred over other possible catalyst quenchers because in case of cell or quench line leakage oxygen is promptly detected by the dedicated glove-box sensor). Once all cells have been quenched, the modules are cooled down and vented, the stir-tops are removed, and the glass inserts containing the reaction phases are taken out and transferred to a centrifugal evaporator (Genevac EZ-2 Plus or Martin Christ RVC 2-33 CDplus), where all volatiles are distilled out and the polymers are thoroughly dried overnight.

Reaction yields are double-checked against on-line monomer conversion measurements (Figure 2.3) by robotically weighing the dry polymers while still in the reaction vials, subtracting the pre-recorded tare. Polymer aliquots are then sent to the characterizations.
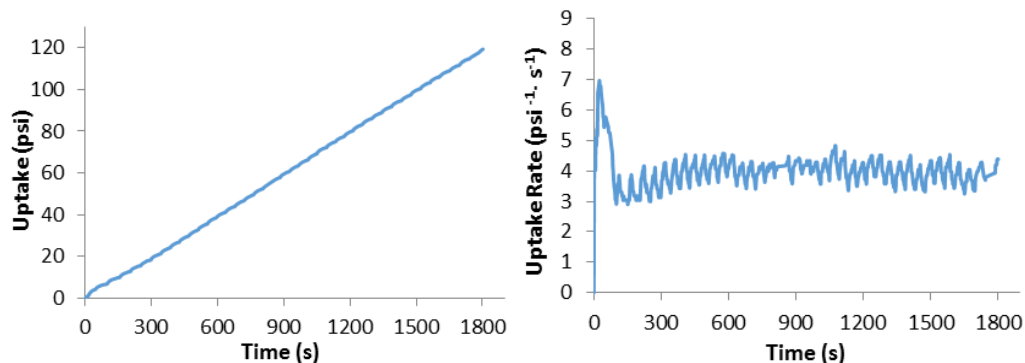
Figure 2.3. Typical profiles of propene uptake (left) and uptake rate (right) vs reaction time for a polymerization experiment performed in the Freeslate PPR48 setup.

It has been demonstrated that, despite the extensive miniaturization, a properly operated PPR platform can yield kinetic information on olefin polymerization reactions with similar precision and accuracy compared with those of conventional bench reactors, combined with up to a 48-fold throughput intensification.[2–4]

2.2.3. Polymer characterization tools and protocols

Accelerating polymer characterizations so as to accommodate the throughput of the PPR48 setup was all but a simple task. The typical yields of PPR cells are in the range of 0.1 to 0.3 g, whereas most available methods for the assessment of ethene-based and propene-based materials require larger amounts (from several grams for the sophisticated determinations at academic labs to some kilograms for the cheaper ASTM measurements used routinely in industrial labs for quality control). Moreover, all said methods take longer than what is necessary for integration with a HTE platform.[5]

This challenge was successfully met by LSP with a smart adaptation and customization of commercial instruments. All polymer samples produced in this project were characterized by means of high-temperature GPC, analytical crystallization elution fractionation (A-CEF), and ^{1}H and ^{13}C NMR spectroscopy.

GPC curves were recorded with a Freeslate Rapid GPC setup (Figure 2.4), equipped with a set of 2 mixed-bed Agilent PLgel 10 μm columns and a Polymer Char IR4 detector. The upper deck of the setup features a sample dissolution station for up to 48 samples in 10 mL magnetically stirred glass vials. With robotic operation, pre-weighed polymer amounts (typically 1 to 4 mg) were dissolved in proper volumes of orthodichlorobenzene (ODCB) containing 0.40 mg mL^{-1} of 4-methyl-2,6-di-*tert*-butyl-phenol (butylhydroxytoluene, BHT) stabilizer, so as to obtain solutions at a concentration of 0.5 to 1.0 mg mL^{-1}.

After 2 h at 150°C under gentle stirring to ensure complete dissolution, the sample array was transferred to a thermostated bay at 145°C, and the samples were sequentially injected into the column line at 145°C and a flow rate of 1.0 mL min^{-1}. In post-trigger delay operation mode, the analysis time was 12.5 min per sample. Calibration was carried out with the universal method, using 10 monodisperse polystyrene samples (M_n between 1.3 and 3700 KDa). Before and after each campaign, samples from a known PP batch produced with an *ansa*-zirconocene catalyst were analyzed for a consistency check. The analysis time was less than 15 min.

Figure 2.4 Overall view of the Freeslate Rapid GPC setup (top), and close-up of the robotic sample preparation deck (bottom).

Analytical Crystallization Elution Fractionation (A-CEF)[6] curves were collected with a Polymer Char A-CEF setup (Figure 2.5), equipped with an autosampler (42 wells), an IR5 detector and a dual capillary viscometer detector. With robotic operation, pre-weighed polymer samples (typically 8-16 mg) were dissolved in ODCB added with 0.40 mg mL^{-1} of BHT stabilizer, so as to achieve a concentration of 2.0 mg mL^{-1}. After 90 min at 150°C under vortexing in sealed vials to ensure complete dissolution, the samples were sequentially charged into the injection loop, where they were held at 95°C for 5 min and then moved into the column. The crystallization step entailed an 8.0°C/min cooling ramp down to 35°C at a flow rate of 0.24 mL min^{-1}; 1 min after reaching 35°C, sample elution was started, with a 4°C min^{-1} heating ramp up to 150°C at a flow rate of 1.0 mL min^{-1}. The analysis time was 60 min for ethene and propene homopolymers, 90 min for less crystalline copolymers.

Figure 2.5. Overall view of the Polymer Char Analytical CEF setup.

Quantitative ^{1}H and ^{13}C NMR spectra at 400 MHz and 100 MHz respectively were recorded with a Bruker Avance III 400 spectrometer (Figure 2.6) equipped with a 5 mm high-temperature cryoprobe and a robotic sample changer with pre-heated carousel (24 positions).

The samples (~30 mg) were dissolved at 120°C in tetrachloroethane-1,2-d_2 (0.7 mL) added with 0.40 mg mL^{-1} of BHT stabilizer, and loaded in the carousel maintained at the same temperature. The spectra were taken sequentially with automated tuning, matching and shimming. Operating conditions were: [^{1}H NMR] 90° pulse; 2.0 s acquisition time; 10 s relaxation delay; 16–32 transients; [^{13}C NMR]: 45° pulse; 2.3 s acquisition time; 5.0 s relaxation delay; 400 to 3K transients (depending on the polymer sample nature and on the microstructural information needed).

Broad-band proton decoupling was achieved with a modified WALTZ16 sequence (BI_WALTZ16_32 by Bruker). Whenever needed, spectral simulation was carried out using the SHAPE2004 software package (M. Vacatello, Federico II University of Naples).

Figure 2.6. Overall view of the Bruker Avance III 400 NMR spectrometer (top), and close-up of the pre-heated robotic sample-changer (bottom).

Thanks to the superior Signal-to-Noise ratio of the used high-temperature cryoprobe (approximately 10-fold larger than for a standard probe), the analysis time for quantitative ^{13}C NMR measurements was in the range of 15 to 60 min.

In total, the aforementioned characterizations make use of roughly 50 mg of polymer cumulatively.

2.2.4. Workflow benchmarking

The rapid characterization measurements described in the previous section were carefully benchmarked against conventional ones.

The Standard Deviation (SD) for Rapid GPC determinations of M_n and M_w turned out to be <15%, which is within good practice specifications of the technique.[7]

A-CEF analyses are very accurate as well: the reproducibility of the temperatures corresponding to elution peak maxima ($T_{el,max}$) was typically within 1°C. On the other hand, A-CEF was used in this project for unprecedented measurements, such as the quantitation of the poorly stereoregular ('atactic') by-product in raw ZN-PP samples. This is normally done by means of solvent fractionation methods; in particular, the 'Xylene-Soluble (XS) Index' is defined as the weight fraction of polymer that does not precipitate after complete dissolution of the sample in hot xylene followed by slow cooling to room temperature.[5] Alternatively, the so-called 'Index of Isotacticity (II)' is the polymer fraction that does not dissolve upon exhaustive extraction in a suitable boiling solvent (usually heptane).[8–10] Measuring XS or II on ZN i-PP with standard methods,[5,11] including automated ones, takes too long and/or requires several grams of sample (which cannot be produced in a PPR cell). We saw the commercial launch of an A-CEF setup by Polymer Char as a tremendous opportunity; this equipment indeed operates on small polymer amounts (10−20 mg), and features a comparatively short analysis time.[6] A typical A-CEF elution curve of an industrial ZN-PP sample is shown in Figure 2.7.
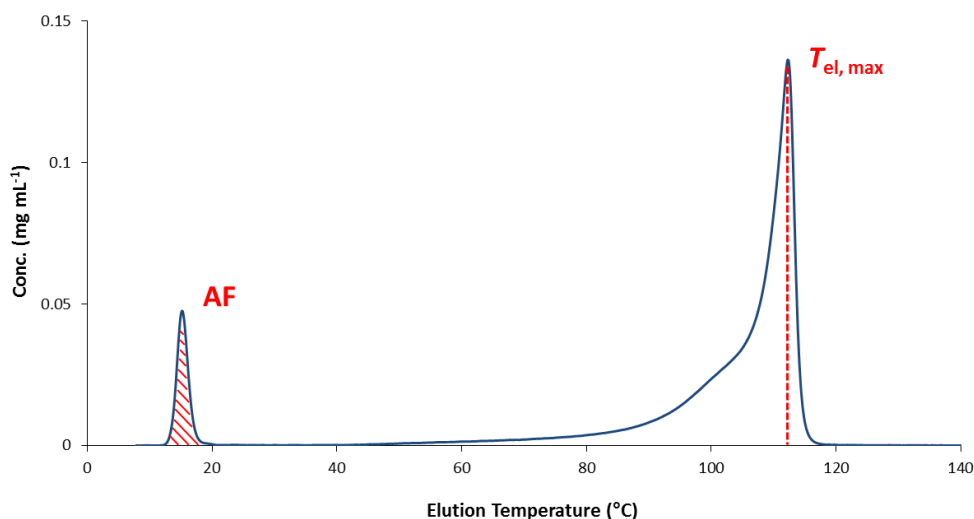
Figure 2.7. CEF curve of a typical iPP sample.

The so-called A-CEF 'Amorphous Fraction (AF)',[6] that is the polymer fraction eluted at room temperature before the temperature ramp is started, should correspond to the XS fraction. Indeed, we found a remarkably good linear correlation ($R^2 = 0.995$) between XS and AF measurements for a set of commercial

ZN-PP samples for which the XS Index had been determined independently (Figure 2.8).
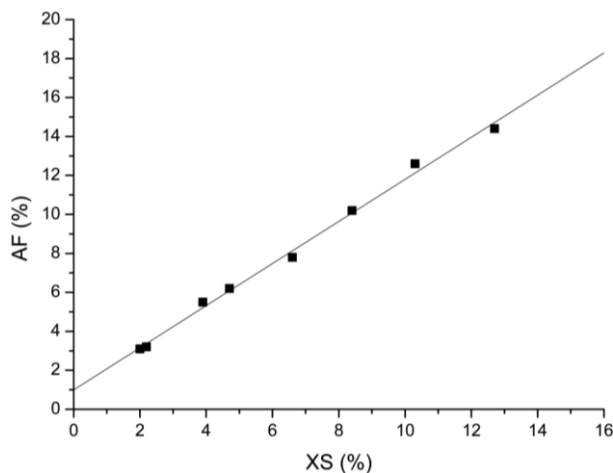
Figure 2.8. Correlation plot between AF (measured by A-CEF) and XS Index for a set of commercial ZN i-PP samples with variable degree of stereoregularity.

From Figure 2.8 it is possible to notice a slight shift of the correlation line from the origin, possibly originated by kinetic effects on polymer crystallization in the two different methods. By systematically exploring the crystallization and elution conditions, the A-CEF analysis time was reduced down to 60 min per PP sample. On a suitable validation set, the absolute standard deviation (aSD) of AF turned out to be as low as aSD = 0.3%, which compares well with what is typically observed when measuring XS with automated equipment.[12,13]

The A-CEF curve (Figure 2.7) also yields information on the crystallinity distribution in a semicrystalline polyolefin sample. For ZN-PP in particular, $T_{el,max}$ is expected to correlate in a first approximation with the degree of isotacticity of the highly crystalline fraction,[6,10] at least for samples with average molecular weight high enough for commercial application. How to achieve quantitative information on said fraction (conventionally referred to as 'isotactic') at PPR scale is another complicated question, because preparative solvent fractionation of raw samples is unfeasible for the small amount and the long experiment time.

Another important achievement in this respect was the implementation of a smart ^{13}C NMR method for measuring the stereoregularity of the 'isotactic' ZN-PP fraction on raw samples in high-throughput mode. In general terms, rapid [13]C

NMR polyolefin characterizations have become feasible after the introduction of high-temperature cryoprobes.[14,15] As already noted, the ca. 10-fold increase in S/N ratio of these probes compared with that of conventional ones translates into a 10^2-fold decrease of experiment time for a desired S/N value. Using 5 mm OD tubes (favored in the present project over 10 mm ones because they require only 20–30 mg of sample per analysis and therefore are compatible with PPR yields), a quantitative ^{13}C NMR PP spectrum suitable for stereosequence determinations can be recorded in about 15 min of accumulation (200 transients), and after 60 min of accumulation (800 transients) peaks down to ~0.1% of the total integral can be measured with good accuracy (Figure 2.9).

The standard practice to estimate the average degree of isotacticity of a ZN-PP sample is to measure the relative abundance of isotactic pentad ([*mmmm*], Figure 2.10) in the methyl region of the ^{13}C NMR spectrum of the xylene-insoluble (XI) fraction.[5,9-11] In the present work, we proposed an alternative method that makes use of a methyl peak which does not receive an appreciable contribution from the XS fraction.

1	*mmmmmm*	9	*mrrrrr*
2	*mmmmmr*	10	*rrrrrr*
3	*mmmmrr*	11	*rrrrmr+mrrrmr*
4	*rrmmrr*	12	*rrrrmm+mrrrmm*
5	*mmmrrm*	13	*rmrrmr*
6	*mmrm+rrrmr*	14	*mmrrmr*
7	*rrmrmr*	15	*mmmrrmmr*
8	*mrmrmm*	16	*mmmrrmmm*
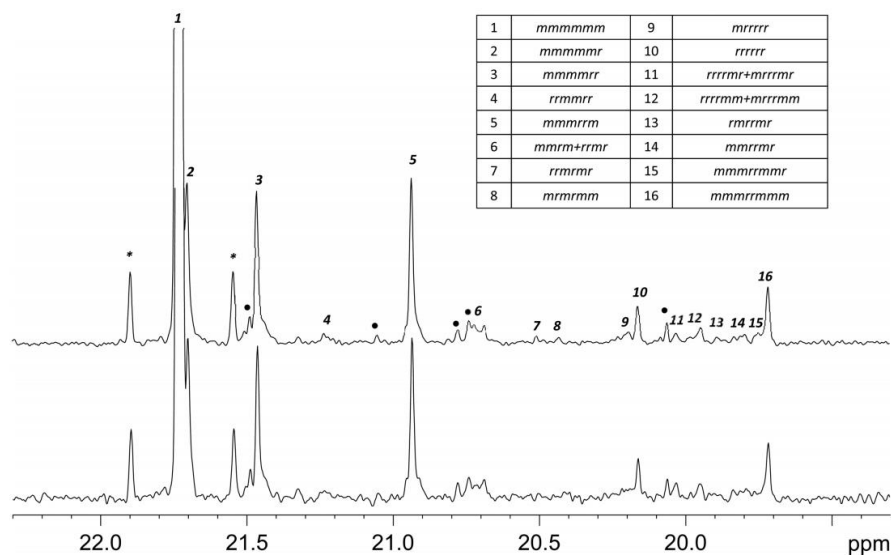
Figure 2.9. Methyl region of the ^{13}C NMR spectra of a representative ZN i-PP sample recorded as described. Top: 800 transients (60 min experiment time). Bottom: 200 transients (15 min experiment time). The chemical shift scale is in ppm downfield of TMS. Resonance assignment is based on the literature.[10] [13]C satellites of the *mmmmmm* peak are denoted with an asterisk (*); peaks arising from chain ends are labeled with the '•' symbol.

Based on the results of spectral simulations according to a three-site stochastic model (that will be described in detail in Chapter 3),[10,16] a convenient choice is the peak of the *mmmrrmmm* nonad (Figure 2.10); indeed, the relative abundance of this sequence (which corresponds to the concentration of isolated stereodefects in long isotactic strands)[10] is practically unaffected by the presence of the XS fraction even in case of poorly stereoregular samples (Table 2.2).
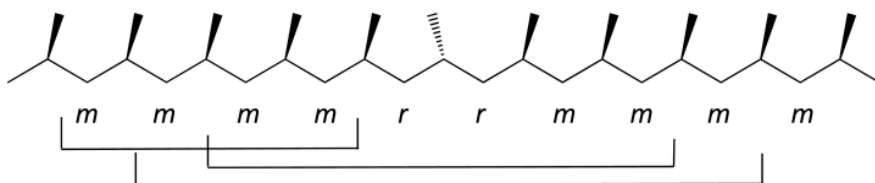
Figure 2.10. Saw-horse representation of an isotactic PP strand containing an isolated stereodefect according to the enantiomorphic-site statistics.[10]

Table 2.2. Fractional abundances of various steric n-ads for isotactic PP samples (fractions) with different degrees of stereoregularity[a] according to a three-site statistical model.[10,16]

n-ad	raw sample, $w_1 = 1.00$	raw sample, $w_1 = 0.97$	raw sample, $w_1 = 0.95$	raw sample, $w_1 = 0.93$
mmmm	0.975	0.955	0.941	0.927
mrrm	0.005	0.007	0.008	0.009
mmrrmm	0.005	0.006	0.007	0.007
mmmrrmmm	0.005	0.006	0.006	0.006

[a] w_1 = weight fraction of the XI fraction ($\sigma_1 = 0.995$); $0.65(1 - w_1)$ = weight fraction of poorly isotactic sequences ($\sigma_2 = 0.85$); $0.35(1 - w_1)$ = weight fraction of syndiotactic sequences ($P_r = 0.80$)

The value of [*mmmrrmmm*] can be measured with high precision by spectral simulation of the *mmrrmm* methyl region[10] (Figure 2.11). On a ZN-PP sample validation set, we measured aSD = 0.03% for [*mmrrmm*] and 0.02% for [*mmmrrmmm*]. From the latter, the corresponding value of [*mmmm*] can be calculated in a straightforward manner using the enantiomorphic-sites statistics:[10] [*mmmrrmmm*] = $\sigma^8(1 - \sigma)$, [*mmmm*] = σ^5 where σ is the enantioselectivity of 1,2 propene insertion.
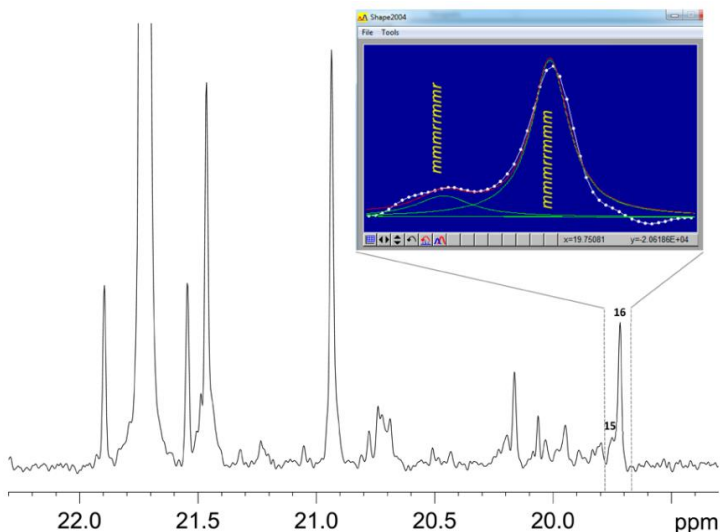
Figure 2.11. Methyl region of the ^{13}C NMR spectrum (800 transients) of a representative ZN-PP sample, and simulation of the *mmrrmm* resonance aimed to evaluate the fractional abundance of the *mmmrrmmm* nonad (see text).[10] The chemical shift scale is in ppm downfield of TMS. For peak assignment, see Figure 2.9.

When the aforementioned methods are applied for the characterization of 48 PP samples (one full PPR library), the turnaround times (TOT) are 12 h for Rapid-GPC, 12-24 h for ^{13}C NMR, 48 h for A-CEF. It is important to notice that a typical PPR48 library consists of 24 duplicate polymerization experiments, and that duplicate samples feature practically identical A-CEF curves and ^{13}C NMR spectra. Therefore, our characterization protocol entails the characterization of all 48 samples by Rapid-GPC, and of one polymer sample per duplicate pair by A-CEF and ^{13}C NMR; this corresponds to a TOT of 24 h. The independent duplicate values of catalyst productivity (R_p), and polymer M_n, and M_w, provide an indication of library reliability, whereas the low error bars of A-CEF and ^{13}C NMR guarantee a robust evaluation of catalyst stereoselectivity (polymer stereoregularity) even with single measurements.

2.3. The '(Pre)catalyst Activation' workflow configuration

The main platforms and units in this workflow are listed in Table 2.3- Some are in common with the olefin polymerization workflow configuration (Section 2.2), but here they are utilized specifically for studies of ZN-PP catalyst system activation.

Table 2.2. List of the main HTE platforms and off-line integrated tools in the workflow.

Part/Function	Unit Operation	Platform/Analytical Tool
Parallel Organic and Organometallic synthesis		Freeslate Extended Core Module
Product Characterization	Product Drying in N_2 Atmosphere	Savant™ Speedvac™ SPD121P centrifugal evaporator
	Elemental Analysis	Agilent 700 series ICP-OES setup
	NMR Analysis	Bruker Avance DRX 400 spectrometer
	HTE GC Analysis	Agilent GC System 7890A
Computational Modeling	Parallel Computation	Cluster of DELL Power Edge M610 Blade Servers (192 cpu's)
		Cluster of Intel Xeon Processor (256 cpu's)

2.3.1. Freeslate Extended Core Module (XCM) platform

This platform (Figure 2.12) is a state-of-the-art setup for parallel organic and organometallic synthesis. Housed in a triple high-performance MBraun LabMaster glove-box, it enables the robotic handling, weighing and dispensing of solid, liquid and slurry air/moisture-sensitive compounds according to fully automated protocols. The main features are:

– Two independent robotic arms bearing a vial gripper (right arm), and dedicated needles for handling solutions (right arm) and slurries (left arm)

– Heated/cooled reaction decks (arrays of 96x1 mL, 24x4 mL, 24x8 mL, 8x20 mL vials with individual magnetic stirring)

– Internal deck-integrated analytical balance (Sartorius WZ614-CW), with ion-suppressor system

- Powdernium™ Automated Powder Dosing System
- Savant™ Speedvac™ SPD121P centrifugal evaporator
- Solvent purification system (MBraun SPS-800, integrated off-line)
- Two high pressure reactors (arrays of 96x1.0-1.2 mL, 25 bar max operation pressure at 200°C, with individual magnetic stirring), for primary screening purposes
- Freeslate LEA software package (PPR Client®, Library Studio®, PolyView®, Epoch®, Impressionist®);
- Renaissance Application Server
- Oracle Database Server

Figure 2.12. Overall view of the Freeslate Extended Core Module™ setup (top), and close-up of the reaction deck (bottom).

2.3.2. (Pre)catalyst activation protocol

The main application of this workflow in the context of the present project was the investigation of ZN precatalyst activation. Typical precatalysts are solid phases of composition $MgCl_2/TiCl_4/ID$, where ID = Internal Donor is an organic Lewis base (e.g. an ester or an ether). They are activated by reaction with a soluble AlR_3/ED cocatalyst, with ED = External Donor, another Lewis base (typically an alkylalkoxysilane). The process is primarily meant to alkylate and reduce the chemisorbed $TiCl_4$ species to $TiCl_2R$ ones; on the other hand, it also leads to the chemisorption of Al species and of part of the ED, particularly in case the ID is reactive with AlR_3 and is extracted from the solid phase.[17,18] A HTE protocol was implemented in order to follow the changes in solid catalyst composition associated with the aforementioned reaction.

In a typical library of experiments, an array of up to 24 8-mL vials, pre-treated for at least 12 h at 200°C under vacuum, are fitted with Parylene™ coated magnetic mini-stir bars, and placed into a 6x4 rack, which is then positioned in a deck bay. In each vial, a 25±1 mg aliquot of $MgCl_2/TiCl_4/ID$ precatalyst is suspended in heptane, and added with aliquots of $AlEt_3$ (TEA) and (where applicable) ED solutions in heptane solutions (generally [Al]/[Ti] = 25; [Al]/[ED] = 10 or 20). The vials are capped, and the catalyst system is left to react for a desired time and temperature under magnetic stirring (800 rpm), after which stirring is stopped and a cold quench is performed by manually transferring the vials into a metal plate kept at -15°C. The vials are then subjected to centrifugation in a Savant SPD121P centrifugal evaporator, re-configured in another deck bay, and uncapped. The supernatants are aspirated robotically (3.6 mL per vial) and transferred to 4 mL vials, which are capped and stored. The solid phases, in turn, are robotically washed twice with 3.6 mL of heptane and once with 3.6 mL of pentane, and finally dried in the centrifugal evaporator for 10 h at 50°C. The obtained samples of dried solid phase and liquid phase are now available for characterizations.

2.3.3. (Pre)catalyst characterization tools and protocols

The dry solid phases recovered after activation were dissolved in methanol-d_4 (1.00 mL). For each solution, 0.60 mL were analyzed by ^{1}H NMR to determine ID and ED amounts, whereas 0.40 mL were dried again, mineralized, and analyzed by Inductively Coupled Plasma Optical Emission Spectrometry (ICP-OES) for Mg, Ti and Al.

Quantitative ^{1}H NMR analyses were performed with a Bruker Avance DRX 400 spectrometer operating at 400 MHz. Acquisition conditions were: 5 mm probe; acquisition time, 3.0 s; relaxation delay, 5.0 s; pulse angle, 90°; spectral width, 10 ppm; 16 transients. Resonance assignment was based on the literature, and preliminary ^{1}H NMR characterizations of the neat donor molecules. A typical ^{1}H NMR spectrum is shown in Figure 2.13. Quantitative determinations were based on peak integration against that of an aliquot of acetonitrile used as internal standard (methyl peak at $\delta = 2.05$ ppm downfield of TMS).
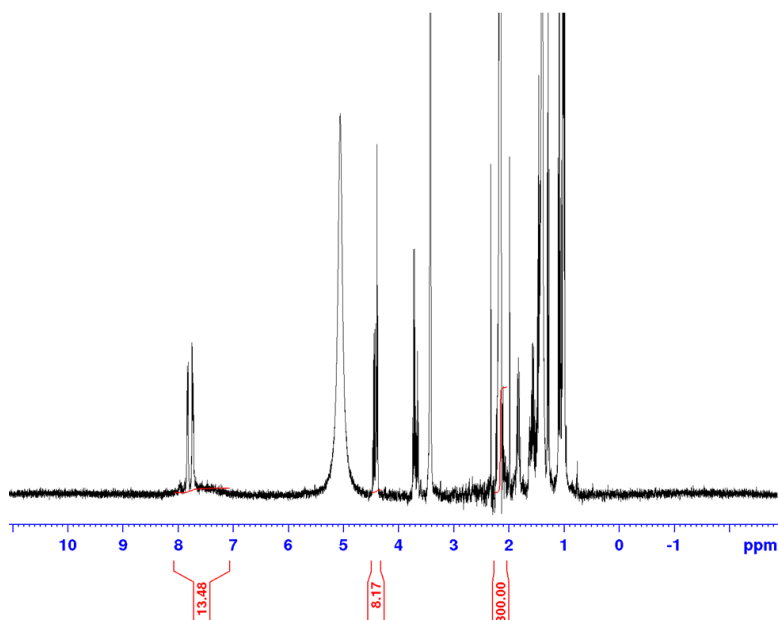
Figure 2.13. ^{1}H NMR spectrum of a methanol-d_4 solution of the solid phase recovered after activating a $MgCl_2/TiCl_4/DBP$ precatalyst with TEA (DBB = dibutylphthalate).

ICP-OES analyses are carried out using an Agilent 700 series spectrometer (Figure 2.14), on water solutions of the solid phases treated in sequence with 2.0 mL of concentrated H_2SO_4, 2.0 mL of concentrated HNO_3, and (when needed) 2.0 mL of 30 vol% H_2O_2 (total time 16 h). The spectrometer was calibrated using commercial standard solutions (metal concentrations in the 1-100 ppm range).

Figure 2.14. ICP-OES Agilent 700 series setup.

References

(1)   *High-Throughput Screening in Heterogeneous Catalysis*; Hagmeyer, A., Strasser, P., Volpe, A. F., Eds.; Wiley-VCH Verlag GmbH & Co. KGaA: Weinheim, FRG, 2004.

(2)   Busico, V.; Pellecchia, R.; Cutillo, F.; Cipullo, R. High-Throughput Screening in Olefinpolymerization Catalysis: From Serendipitous Discovery towards Rational Understanding. *Macromol. Rapid Commun.* **2009**, *30* (20), 1697–1708.

(3)   Beigzadeh, D. Application of Polymerization Kinetic Modeling in High-Throughput Screening of Catalyst Systems for Productivity. *Macromol. React. Eng.* **2007**, *1* (3), 331–337.

(4)   Rongo, L. PhD Thesis: Ziegler-Natta Catalysts: Mechanistic Study via High Throughput Screening Methodologies, Federico II University of Naples, 2013.

(5)   Pasquini, N. *Polypropylene Handbook, 2nd Ed.*; Hanser Publisher: Munich, 2005.

(6)   Monrabal, B.; Romero, L. Separation of Polypropylene Polymers by Crystallization and Adsorption Techniques. *Macromol. Chem. Phys.* **2014**, *215* (18), 1818–1828.

(7)   D'Agnillo, L.; Soares, J. B. P.; Penlidis, A. Round-Robin Experiment in High-Temperature Gel Permeation Chromatography. *J. Polym. Sci. Part B Polym. Phys.* **2002**, *40* (10), 905–921.

(8)   Cecchin, G.; Morini, G.; Piemontesi, F. Ziegler-Natta Catalysts. In *Kirk-Othmer Encyclopedia of Chemical Technology*; Seidel, A., Ed.; John Wiley & Sons, Inc.: Hoboken, NJ, 2007; pp 502–554.

(9)   Kaminsky, W. *Polyolefins : 50 Years after Ziegler and Natta I, Polyethylene and Polypropylene*; 2013; Vol. 257.

(10)   Busico, V.; Cipullo, R. Microstructure of Polypropylene. *Prog. Polym. Sci.* **2001**, *26* (3), 443–533.

(11)   Cecchin, G.; Morini, G.; Piemontesi, F.; Seidel, A. . *Kirk-Othmer Encyclopedia of Chemical Technology*; Wiley Interscience: New York, 2007; p Vol. 26.

(12)   See, for Example, Http://Www.Polymerchar.Com/Crystex.

(13)   Busico, V.; Cipullo, R.; Mingione, A.; Rongo, L. Accelerating the Research Approach to Ziegler–Natta Catalysts. *Ind. Eng. Chem. Res.* **2016**, *55* (10), 2686–2695.

(14)   Zhou, Z.; Kümmerle, R.; Stevens, J. C.; Redwine, D.; He, Y.; Qiu, X.; Cong, R.; Klosin, J.; Montañez, N.; Roof, G. 13C NMR of Polyolefins with a New High Temperature 10mm Cryoprobe. *J. Magn. Reson.* **2009**, *200* (2), 328–333.

(15)   Zhou, Z.; Stevens, J. C.; Klosin, J.; KUmmerle, R.; Qiu, X.; Redwine, D.; Cong, R.; Taha, A.; Mason, J.; Winniford, B.; et al. NMR Study of Isolated 2,1-Inverse Insertion in Isotactic Polypropylene. *Macromolecules* **2009**, *42* (6), 2291–2294.

(16)   Busico, V.; Cipullo, R.; Monaco, G.; Talarico, G.; Vacatello, M.; Chadwick, J. C.; Segre, A. L.; Sudmeijer, O. High-Resolution ^{13}C NMR Configurational Analysis of Polypropylene Made with $MgCl_2$ -Supported Ziegler–Natta Catalysts. 1. The "Model" System $MgCl_2/TiCl_4$ −2,6-Dimethylpyridine/$Al(C_2H_5)_3$. *Macromolecules* **1999**, *32* (13), 4173–4182.

(17)   Noristi, L.; Barbè, P. C.; Baruzzi, G. Effect of the Internal/External Donor Pair in High-Yeld Catalysts for Propylene Polymerization, 1. Catalysts-Cocatalyst Interactions. *Makromol. Chem.* **1991**, *192*, 1115–1127.
(18)   Barbè, P. C.; Cecchin, G.; Noristi, L. . *Adv. Polym. Sci.* **1986**, *81*, 1–81.

3. Stereoselectivity of ZN catalysts for PP

3.1. Introduction

Polyethylene (PE) and polypropylene (PP) are the 1st and the 2nd largest volume polymer on the global market, respectively.[1] The current yearly demand of PE is about 110 million tons, and that of PP exceeds 60 million tons. Overall, they represent more than 50% by weight of all large-volume plastics, and despite the growing concerns for the spread of plastic wastes in the environment there is no sign that the industrial scenario may change drastically in the next one or two decades.

Both polymers are aliphatic hydrocarbons, and as such a number of chemical and physical properties are similar. Yet, the presence of a methyl branch in the monomeric unit of PP has dramatic consequences on how the polymer is made and applied. As a matter of fact, the skeletal C atoms bearing the branch are chirotopic, and their relative configurations dictate the extent to which the polymer is able to crystallize, and the physical and application properties that can follow.

As is well-known, with the only exception of Low-Density Polyethylene (LDPE) which is obtained with a radical process, PE and PP based materials are produced with the mediation of transition metal catalysts. At odds with the case of PE, where the discovery of countless molecular catalysts of metallocene and 'post-metallocene' nature able to copolymerize ethene and higher 1-alkenes has

boosted the market of so-called Linear Low-Density Polyethylene (LLDPE), PP catalysis is much more conservative, and over 98% of PP-based materials are produced with heterogeneous Ti-based catalyst systems that are closely related to the original ones invented by Ziegler and Natta in 1953-1954. The desired stereostructure for the homopolymer is isotactic (i.e. perfectly regioregular with all stereogenic C atoms featuring the same relative configuration), and practically all chemical elaborations of the catalysts over the last 60 years have been aimed to approach as much as possible this ideal configuration.

The first two generations of ZN catalysts consisted of $TiCl_3$ in one of its 'violet' crystalline modifications (α, γ, δ) with a layer structure, in combination with an Al-alkyl cocatalyst (e.g. $AlEt_3$).[2,3] Stereoselectivity was the consequence of a peculiar layered crystal lattice with chirotopic Ti both in the bulk and on the side edges of the structural layers. The latter, in particular, exposed linear arrays of enantiomorphous Ti atoms amenable to Cl/R metathesis with the Al-alkyl compound.[4–6] Elegant experimental[7] and computational[8,9] studies highlighted the surface constraints on the thus formed Ti-alkyl species, conformationally locked at the first C-C bond so as to define chiral pockets in which the two propene enantiofaces could be discriminated at the insertion step.[5,10] A seminal model of catalytic species was introduced by Corradini (Figure 3.1).[11]

The main pitfall of those early catalysts was the rather low productivity, making it necessary to remove the acidic Ti-Cl residues from the polymer with cumbersome and expensive post-reaction procedures. Supporting the active Ti species on an inert matrix looked like a logical solution.[3,4]
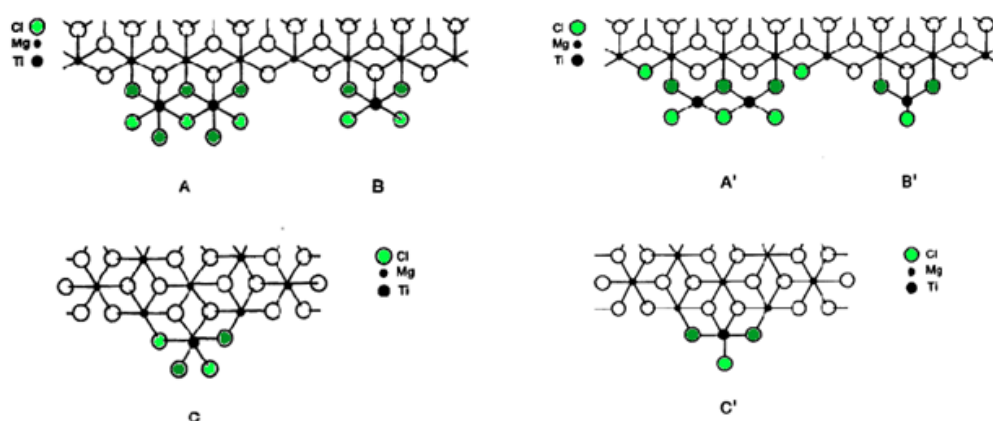
Figure 3.1. Epitaxial models of Ti_xCl_{4x} (A–C) and Ti_xCl_{3x} (A'–C') species on lateral $MgCl_2$ crystal terminations, according to Corradini et al.[11]

Supported homologues with greatly improved performance, but also much more complex formulations, were introduced in the 1970s.[3-5] MgCl$_2$ was serendipitously identified as the best-working support for TiCl$_4$ (the Ti precursor of largest use).[3] The addition of certain donor compounds as powerful stereoselectivity enhancers (Table 3.1), at the precatalyst preparation stage ('Internal Donors', IDs) or in combination with the AlR$_3$ activator ('External Donors', EDs), was also a trial-and-error achievement.[3,4]

Table 3.1. Typical formulations and performance of ZN catalyst systems for iPP production.[3,4]

Generation	Internal Donor, ID	External Donor, ED	Productivity[a]	I.I.[b]	M_w/M_n
Third	Aromatic monoester (e.g. ethylbenzoate)	Aromatic monoester (e.g. methyl-*p*-toluate)	0.5-0.8	>95	6-9
Fourth	Aromatic diester (e.g. dibutylphthalate)	Alkoxysilane (e.g. R^{1}R^{2}Si(OMe$_2$))	1-2	>98	6-8
Fifth	2,2'-dialkyl-1,3-dimethoxypropane	Alkoxysilane (e.g. R^{1}R^{2}Si(OMe$_2$))	>2	>97	4-6
Sixth	Aliphatic diester (e.g. dialkylsuccinate)	Alkoxysilane (e.g. R^{1}R^{2}Si(OMe$_2$))	1-2	>97	>8

[a] 10^3 kg(PP) g(Ti)$^{-1}$. [b] 'Index of Isotacticity' in wt.-%.

Understanding the reason(s) for this extraordinary performance was, and still is, very challenging, and originated the reputation of 'black-boxes' for these systems. The similarity between the crystal lattices of MgCl$_2$ and TiCl$_3$ stimulated the idea of an epitaxial relationship between at least part of the TiCl$_x$ adsorbates and the MgCl$_2$ substrate.[4,11-13] Unfortunately, rather than representing a constructive input, this hypothesis triggered decades of flawed mechanistic speculations, including that of a competition between TiCl$_4$ and the donors for selective chemisorption on the support.[4,11-13] MgCl$_2$(10l) crystal terminations, exposing pentacoordinated Mg, have long been claimed to host Ti$_2$Cl$_8$ adducts that, once activated by an AlR$_3$, would mimic the active sites of authentic TiCl$_3$ catalysts. MgCl$_2$(110) terminations, in turn, featuring tetracoordinated Mg and as such more acidic, were postulated to be preferred targets for donor binding, and home to non-stereoselective sites only. The successful introduction, in the 1990s, of 2,2-dialkyl-1,3-dimethoxypropanes as a class of IDs especially prone to chelate tetracoordinated Mg, thus supposedly hampering TiCl$_4$ interaction with

MgCl$_2$(110) facets,[3,4,14] was presented as a compelling demonstration of the hypothesis, and – even – as an achievement of molecular design.[14,15]

It was only several years later that more critical analyses of the experimental data and Quantum Mechanics (QM) modeling studies disproved the concept of MgCl$_2$(10l) and MgCl$_2$(110) as 'good' and 'bad' surfaces, respectively. As a matter of fact, it became impossible to ignore the unambiguous evidence that donor molecules have a direct and specific impact on polymer microstructure,[16] and therefore are, if not part of the catalytic species, at least at non-bonded contact with them.[13] Several independent Density Functional Theory (DFT) calculations, in turn, concluded that Ti$_2$Cl$_8$ adsorbates on MgCl$_2$(10l)-like edges are not stable,[17,18] and lately that TiCl$_4$ chemisorption is only feasible in mononuclear form on MgCl$_2$(110)-like edges.[19,20]

The current view is that the role of donors in MgCl$_2$-supported ZN catalyst systems is twofold:

i) Stabilize the primary particles by strong chemisorption, lowering their surface energy.[21–23] Mg/donor mole ratios in the range of 10 to 20 are not unusual,[3,4] which points to lateral dimensions of the structural layers of only few unit cells,[21,24] and values of surface area in excess of 150 m^2 g^{-1} (unattainable for binary MgCl$_2$/TiCl$_4$ particles because TiCl$_4$ adsorption is too weak[19]).

ii) Impart the necessary steric hindrance to the inherently chiral but otherwise too open catalytic species, very much alike ancillary ligands in molecular catalysts.[13] A qualitative model for this function, which is a re-visitation of Corradini's model for TiCl$_3$ catalysts (Figure 3.1), has been proposed in the late 1990s (Figure 3.2).[25] This 3-site model still accounts for all known factual observations, including the stereoblock architecture of (part of) the polymer.[13] In brief, it has been demonstrated that some PP chains contain, in addition to long and almost perfect isotactic sequences, short sequences of lower stereoregularity – either poorly isotactic ('isotactoid') or syndiotactic. The (reversible) desorption of one or two donor molecules from the surface next to the catalytic species provides a simple and plausible explanation for the observed changes in stereoselectivity.

Figure 3.2. Dynamic 3-site model of catalytic species for MgCl2-supported ZN catalysts. Species **C1**, **C2**, **C3** would be responsible for (highly) isotactic, isotactoid, and syndiotactic chain propagation, respectively. **L1** and **L2** are surface Cl atoms or chemisorbed LB molecules.

Although in principle one single donor might exert both aforementioned functions (i.e., surface stabilization and steric modulation of the catalytic pocket), in most cases the ID and ED roles are differentiated (Table 3.1).[3,4,13] Surface stabilization is important already at the stage of primary particle formation; this usually entails chlorination of a Mg precursor compound with excess $TiCl_4$ in the presence of the ID, which requires that the latter compounds are mutually unreactive. For the modification of the catalytic species, on the other hand, a proper steric demand, the preference for chemisorption on Mg rather than Ti, and the lack of reactivity with AlR_3 are equally important conditions. Some well-functioning IDs (e.g. dialkylphthalates) react irreversibly with the AlR_3 activator, and are extracted from the solid catalyst during polymerization;[3,4,26,27] therefore, they need to be replaced by an ED. By far the most widely used EDs are sterically demanding alkoxysilanes;[3] these are poorly reactive with AlR_3 compounds, but do react with $TiCl_4$, which prevents their use as IDs.

While the above general picture is sound, what is still missing is an adequate understanding of the details that would enable true catalyst design. In particular, how the catalytic species look like and what determines their diverse behaviors in the different catalyst generations remain largely unanswered questions. In this sense, the aforementioned black-box perception is justified, but can now be amended by means of HTE explorations.

In Section 3.2, the results of an extensive and thorough study of fourth-, fifth- and sixth-generation ZN PP catalysts (Table 3.1), used in combination with $AlEt_3$ (TEA) and an array of alkoxysilane EDs with large structural diversity, are

presented and discussed. The investigation, carried out with the advanced HTE tools and methods illustrated in Chapter 2,[28] consisted of two parts. In a first part, catalyst performance (in terms of polymerization behavior and polymer properties) was determined using a fully automated secondary screening platform with 48 mini-reactors (Freeslate PPR48), integrated with a polymer characterization workflow including Gel Permeation Chromatography (GPC), analytical Crystallization Elution Fractionation (A-CEF), and ^{13}C NMR spectroscopy. In a second part, another HTE platform (Freeslate Core Module) was used to follow the evolution in composition of the activated solid catalysts under conditions closely mimicking those of application. The main goal was to highlight the QSAR of the investigated catalyst formulations as far as the stereoselectivity is concerned. Thanks to a database of extraordinary and unprecedented width and depth for a single investigation, a high-definition picture of the screened systems was obtained, enabling to highlight for the first time important details of their inner workings. In particular, the delicate relationship between surface coverage at saturation and lateral steric pressure on the stereoselectivity of the catalytic species was explored, and the roles of chemisorbed donors and Al-alkyl species on said parameters for different formulations (i.e. catalyst surface distributions) were clarified; this is very important for further progress.

The scope of surface modification by reactive/labile IDs was also explored (Section 3.3). In particular, for ester-ID-containing catalysts, a systematic and thorough kinetic investigation was carried out for the reaction between TEA and the ID, in solution as well as after chemisorption on the catalyst surface. It may be worth recalling here that a recent REACH ban on dialkylphthalates for toxicity issues has generated a growing market demand for their replacement as IDs;[1] considering that fourth-generation ZN systems are the working horses of PP industry,[3] the question is of high relevance and calls for urgent attention.

Most of the results reported in the following sections have been published.[29,30] Parts of text, tables and figures are reproduced with permission by the publishers.

3.2. A QSAR HTE study of ZN PP catalysts in action

3.2.1. The catalyst systems

The four ZN catalysts selected for this study (Table 3.2) belong in the three latest generations of commercial relevance (Table 3.1).[3,4] Catalyst **C1** (ID = dibutylphthalate) is a widely used fourth-generation representative.[3,4] Catalysts **C2** (ID = 2,2-diisobutyl-1,3-dimethoxypropane) and **C3** (ID = 2,2-dimethyl-1,3-dimethoxypropane) are members of the fifth generation; the former found industrial application, whereas the latter is poorly stereoselective[14,15] but very interesting from a mechanistic standpoint, as we shall see in following sections. Catalyst **C4** (ID = 2,3-diisopropyldiethylsuccinate) was chosen as an example of the sixth generation, the most recent and also the least described in the scientific literature.[3] Alkoxysilane EDs are employed with all three generations (Table 3.1), even though fifth-generation systems may also be used without.[3,4,14] The ED set screened in the present study (Table 3.3) included dimethoxy-, trimethoxy- and triethoxysilanes bearing linear, branched and cyclic substituents with different steric demand; three of them (namely, **ED1**-**ED3**) were selected as 'minimal structures' for comparative purposes, whereas the remaining five (**ED4-ED8**) are applied commercially.

Table 3.2. Compositions of the screened (pre)catalysts.

Code	Internal Donor (ID)	Ti (wt%)	Mg (wt%)	ID (wt%)
C1	Dibutylphthalate	2.0	18.6	11.5
C2	2,2-Diisobutyl-1,3-dimethoxypropane	2.7	18.4	13.2
C3	2,2-Dimethyl-1,3-dimethoxypropane	2.1	19.1	9.3
C4	2,3-Diisopropyldiethylsuccinate	2.4	19.2	9.5

Table 3.3. The set of screened alkoxysilane EDs.

ED1 Dimethyldimethoxy-	ED2 Propyltrimethoxy-	ED3 Propyltriethoxy-	ED4 Cyclohexylmethyldimethoxy-
ED5 Diisobutyldimethoxy-	ED6 Diethylaminotriethoxy-	ED7 Diisopropyldimethoxy-	ED8 Dicyclopentyldimethoxy-
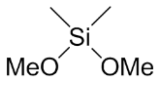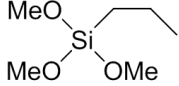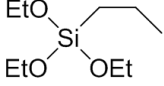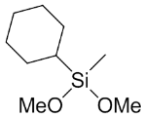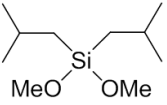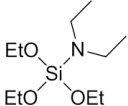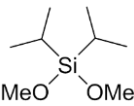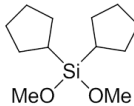
3.2.2. Propene polymerization screening

In total, 132 duplicate pairs of slurry propene homopolymerization experiments were run under the same conditions (T = 70°C, $p(C_3H_6)$ = 4.5 bar, $p(H_2)$ = 0.20 bar, [Al]/[Ti] = 160, t = 30 min), except for the [ED]/[Al] ratio that was varied stepwise ([ED]/[Al] = 0, 0.025, 0.050, 0.10, 0.20). The polymerizations were carried out according to the protocol described in Section 2.3.2. Catalyst deactivation was always negligible, and polymerization kinetics could be simply quantified in terms of average catalyst productivity (R_p, in kg(PP) g(catalyst)$^{-1}$ h^{-1}). Polymer molecular weight, crystallinity and stereosequence distributions were determined by Rapid-GPC, analytical Crystallization Elution Fractionation (A-CEF), and quantitative ^{13}C NMR spectroscopy, all applied in HTE mode with protocols specifically implemented for use downstream of the PPR48 platform as described in Chapter 2.[28] In particular, the Amorphous Fraction (AF) measured by A-CEF was used as a replacement of the Xylene-Soluble (XS) Fraction, difficult to obtain rapidly and reliably in PPR48 scale; the two methods were shown to correlate nicely (see Section 2.3.4, Figure 2.8).[28] The concentration of stereodefects in the isotactic fraction, in turn, was obtained from the ^{13}C NMR spectra of raw samples, by measuring the fractional amount of the *mmmrrmmm* nonad in the methyl region (Section 2.3.4, Figure 2.11).[13,28] For selected PP samples, the *mrrm* pentad and

rrrrrr heptad were also quantified to reveal the presence of stereoblock chains.[13,25]

The full results of the polymerization screening are reported in Tables A3.1-A3.4 (Appendix at the end of this Chapter). An excerpt for all catalyst systems at [ED]/[Al] = 0.10 is given in Table 3.4 (A-D) and Figures 3.3, 3.4. The three catalyst generations are known to yield polymers with different and characteristic M_w/M_n ranges (Table 3.1);[3,4] the obtained results are in line with that. The propensity to undergo ED modification was also idiosyncratic: very high for catalyst **C1**, moderate for catalyst **C4**, almost negligible for catalysts **C2** and **C3**. We will comment extensively on the overall results in general, and on the latter aspect in particular, in a subsequent section.

Table 3.4. Polymerization results for catalysts **C1**-**C4**-AlEt$_3$/**EDx** at [ED]/[Al] = 0.10.

							Catalyst C1		
EDx	R_p (Kg g^{-1} h^{-1})	M_n (KDa)	M_w (KDa)	M_w/M_n	AF (%)	$T_{el,max}$ (°C)	[*mmmrrmmm*] (%)	[*mrrm*] (%)	[*rrrrrr*] (%)
None	7.2	17	103	6.1	15.2	113.2	0.90	2.1	1.3
	7.9	18	103	5.7	11.9	113.0	0.92	2.0	1.3
ED1	6.3	29	175	6.0	6.3	112.9	1.12	2.0	0.4
	5.0	29	175	6.0	7.3	113.1	1.06	1.9	0.5
ED2	5.0	42	222	5.3	3.3	115.8	0.48	1.0	0.3
	5.5	29	229	7.8	3.5	115.9	0.49	0.9	0.2
ED3	5.2	30	180	6.0	4.8	115.5	0.49	0.9	0.4
	6.3	26	145	5.5	4.4	115.6	0.48	1.0	0.3
ED4	8.3	42	257	6.1	4.3	116.2	0.41	1.0	0.3
	6.4	32	284	8.8	3.8	116.2	0.47	1.0	0.3
ED5	7.2	38	251	6.6	4.7	116.3	0.46	0.8	0.3
	8.3	41	242	5.9	3.6	116.3	0.40	0.8	0.3
ED6	4.8	25	198	7.9	5.2	116.4	0.43	1.0	0.4
	5.1	25	177	7.2	5.5	116.4	0.43	0.9	0.4
ED7	6.7	40	319	8.0	3.2	117.4	0.30	0.7	0.2
	7.1	39	313	8.0	3.6	117.5	0.29	0.6	0.2
ED8	8.7	45	393	8.8	3.0	117.9	0.26	0.6	0.2
	7.6	46	399	8.7	3.0	117.8	0.29	0.6	0.2

						Catalyst C2			
EDx	R_p **(Kg g^{-1} h^{-1})**	M_n **(KDa)**	M_w **(KDa)**	M_w/M_n	**AF (%)**	$T_{el,max}$ **(°C)**	**[*mmmrrmmm*] (%)**	**[*mrrm*] (%)**	**[*rrrrrr*] (%)**
None	11.1	27	124	4.6	3.9	114.0	0.75	1.3	0.1
	10.7	33	162	4.9	4.4	113.7	0.67	1.3	0.1
ED1	11.2	32	157	4.9	3.5	113.5	0.66	1.1	0.2
	8.8	33	173	5.3	4.1	113.6	0.65	1.1	0.1
ED2	7.8	32	169	5.3	2.8	114.3	0.56	1.0	0.1
	6.5	32	164	5.2	2.4	114.2	0.55	1.0	0.1
ED3	10.4	34	185	5.5	3.6	114.4	0.65	1.0	<0.1
	8.9	32	169	5.3	3.6	114.1	0.57	1.0	0.2
ED4	10.1	35	157	4.5	3.7	114.1	0.52	1.0	0.1
	10.1	35	161	4.6	2.9	114.2	0.53	1.0	0.1
ED5	9.2	35	194	5.6	3.1	114.1	0.58	1.0	0.1
	7.1	26	144	5.6	3.4	113.9	0.55	1.0	0.1
ED6	9.5	34	179	5.2	3.7	113.5	0.56	1.0	0.1
	9.6	34	205	6.0	4.4	112.8	0.47	0.9	0.2
ED7	10.6	29	166	5.8	3.6	114.0	0.55	1.0	0.1
	5.9	33	168	5.1	4.9	113.8	0.58	1.0	0.1
ED8	10.8	38	189	5.0	3.6	114.6	0.60	1.0	0.2
	10.0	33	180	5.5	3.8	114.3	0.53	0.9	0.1

						Catalyst C3			
EDx	R_p **(Kg g^{-1} h^{-1})**	M_n **(KDa)**	M_w **(KDa)**	M_w/M_n	**AF (%)**	$T_{el,max}$ **(°C)**	**[*mmmrrmmm*] (%)**	**[*mrrm*] (%)**	**[*rrrrrr*] (%)**
None	6.0	19	87	4.7	19.4	109.7	1.63	3.5	0.8
	5.9	28	105	3.7	18.2	110.0	1.53	3.0	0.6
ED1	4.7	21	104	4.9	14.8	110.5	1.33	2.6	0.6
	4.0	22	108	5.0	15.0	110.4	1.35	2.5	0.4
ED2	3.5	23	101	4.3	12.7	111.1	1.33	2.4	0.5
	3.8	21	109	5.1	10.1	111.2	1.17	2.4	0.5
ED3	4.5	22	122	5.6	12.3	110.9	1.24	2.4	0.5
	4.7	18	96	5.4	13.2	110.9	1.24	2.4	0.5
ED4	5.0	22	110	5.0	13.6	111.2	1.18	2.4	0.5
	5.0	20	99	4.9	12.9	111.0	1.22	2.5	0.5
ED5	4.5	24	114	4.7	12.5	110.9	1.28	2.4	0.5
	4.9	22	105	4.7	12.4	110.9	1.39	2.5	0.5
ED6	4.1	23	110	4.7	12.7	111.1	1.29	2.3	0.6
	4.5	28	114	4.1	12.3	111.4	1.16	2.1	0.4
ED7	4.1	21	103	4.9	14.5	111.4	1.28	2.4	0.5
	4.8	25	108	4.3	13.3	111.7	1.19	2.5	0.5
ED8	4.8	23	113	5.0	12.5	110.9	1.14	2.4	0.5
	4.3	23	112	4.9	13.2	110.8	1.15	2.5	0.5

				Catalyst C4					
EDx	R_p (Kg g^{-1} h^{-1})	M_n (KDa)	M_w (KDa)	M_w/M_n	AF (%)	$T_{el,max}$ (°C)	[*mmmrrmmm*] (%)	[*mrrm*] (%)	[*rrrrrr*] (%)
None	4.0	16	103	6.5	9.9	115.0	0.70	1.6	0.6
	4.8	15	124	8.1	9.6	115.2	0.78	1.5	0.7
ED1	5.1	16	134	8.3	8.5	115.2	0.78	1.6	0.6
	4.9	17	135	7.8	9.0	115.1	0.81	1.6	0.7
ED2	4.8	18	139	7.7	5.0	115.3	0.53	1.1	0.3
	5.1	20	152	7.6	5.1	115.8	0.50	1.0	0.3
ED3	5.2	18	167	9.1	5.9	115.9	0.57	1.1	0.6
	5.7	19	143	7.7	5.6	115.8	0.53	1.1	0.5
ED4	6.3	20	182	9.3	5.6	116.1	0.54	1.1	0.5
	6.3	19	180	9.5	6.0	116.2	0.51	0.9	0.4
ED5	5.9	20	175	9.0	6.0	115.9	0.52	0.9	0.5
	6.9	20	168	8.6	5.7	116.3	0.51	0.9	0.4
ED6	5.1	18	155	8.7	7.1	116.3	0.45	0.9	0.4
	5.1	18	153	8.6	6.3	116.4	0.48	1.0	0.4
ED7	6.0	22	174	8.0	5.9	116.7	0.40	1.0	0.3
	6.2	20	171	8.6	5.1	116.7	0.42	0.9	0.3
ED8	7.2	23	274	12.1	5.5	117.2	0.37	0.8	0.3
	6.1	19	250	13.2	5.1	117.2	0.39	0.9	0.3
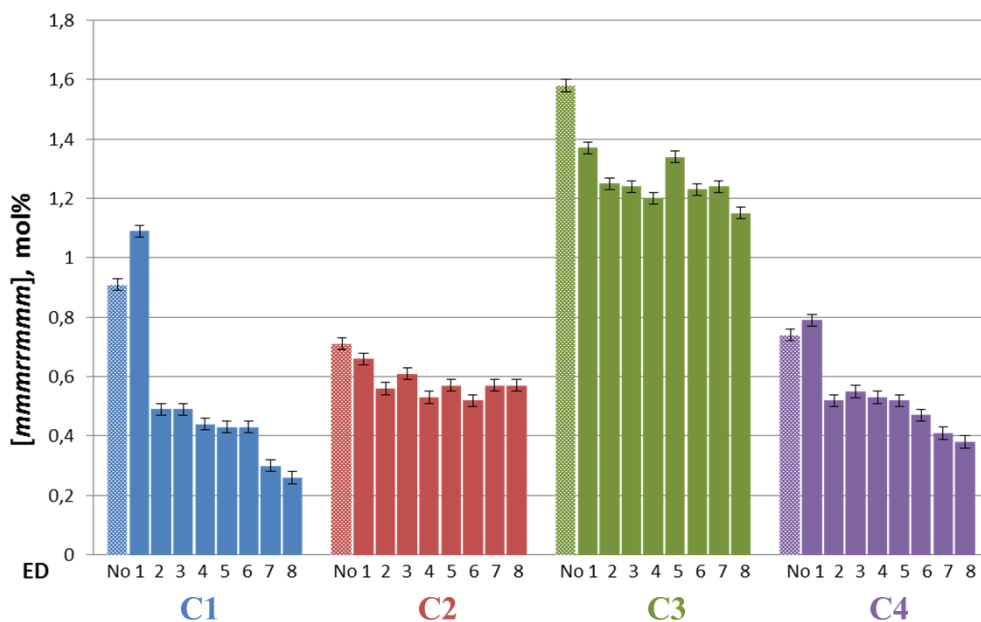
Figure 3.3. Normalized fraction of the *mmmrrmmm* nonad[13,28] for the i-PP samples of Table 3.4.
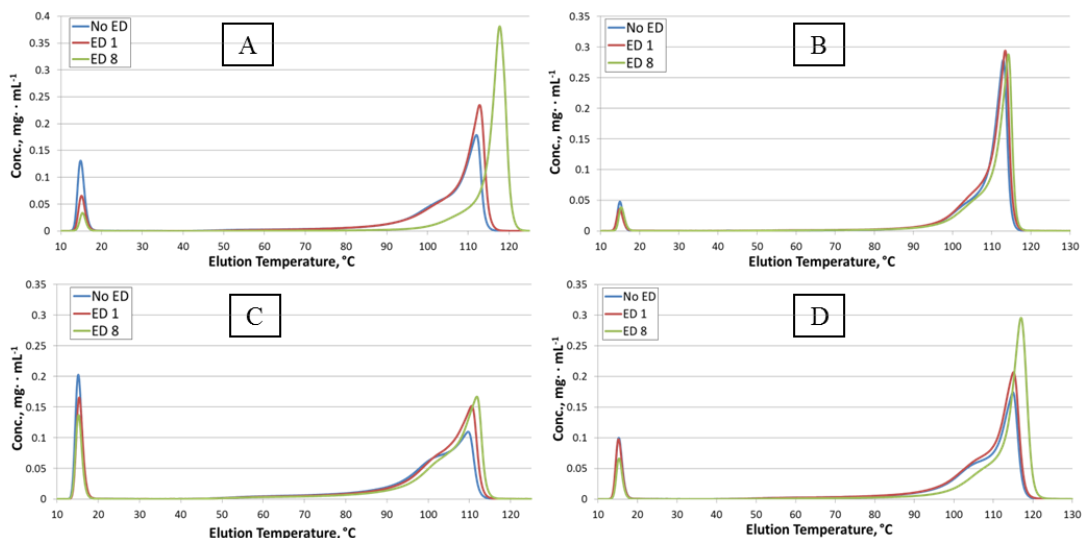
Figure 3.4. Overlay of the A-CEF elution curves for representative polymers obtained with catalysts **C1** (A), **C2** (B), **C3** (C), and **C4** (D) in combination with different AlEt$_3$(/**EDx**) mixtures.

3.2.3. Precatalyst activation and active catalyst composition screening

In parallel with the polymerization screening, the evolution of catalyst composition, in terms of Ti, Al, ID and ED contents, following the reaction of all four catalysts with AlEt$_3$(/ED) in heptane slurry was investigated under conditions similar to those of application (see §2.4.2 for experimental details). For this study, two EDs largely differing in steric bulk were selected, namely dimethyldimethoxysilane (**ED1**) and dicyclopentyldimethoxysilane (**ED8**); the [ED]/[Al] ratio was set at a value of 0.10 (i.e., the same used for the experiments in Table 3.4). The other experimental conditions were T = 70°C, [Al]/[Ti] = 25, t = 30 min. Looking at the results, reported in Table 3.5 and Figure 3.5, the following facts should be noted:

[a] Interaction with AlEt$_3$ resulted into a substantial ID extraction for catalysts **C1** ($\approx$60%) and **C4** (30%). With AlEt$_3$/ED combinations the process went even further ($\approx$80% ID extraction for **C1**, $\approx$60% for **C4**), and was associated with an extensive ID/ED exchange.

[b] The IDs of catalysts **C2** and **C3**, on the other hand, were retained for over 85% upon exposure to AlEt$_3$ as well as AlEt$_3$/ED. In the latter case, only a modest amount of ED was adsorbed.

[c] For a given catalyst, the incorporation of **ED1** and **ED8** (in mol per mol of Mg) was practically the same.

[d] A massive chemisorption of Al species was observed for all systems, including those where the ID was retained.

[e] All catalysts underwent a significant (20-50%) loss of Ti.

Table 3.5. Evolution of catalyst composition upon reaction with AlEt$_3$(/ED).

Catalyst	Cocatalyst	Precatalyst Amount (mg)	mol% mol(Mg)$^{-1}$			
			Ti	ID	ED	Al
C1		Untreated	4.4	5.6	-	-
	AlEt$_3$	19.8	2.6	2.0	-	10.3
		20.0	2.8	2.3	-	11.4
	AlEt$_3$/**ED1**	15.8	2.5	1.2	5.5	8.0
		16.7	2.2	0.6	5.9	7.2
	AlEt$_3$/**ED8**	21.8	1.6	0.9	4.7	6.4
		20.7	2.4	1.3	5.3	7.4
C2		Untreated	6.9	8.2	-	-
	AlEt$_3$	19.5	5.7	6.7	-	11.1
		14.7	5.3	8.1	-	12.6
	AlEt$_3$/**ED1**	14.5	5.6	7.3	2.8	8.8
		14.6	5.5	7.3	3.1	8.6
	AlEt$_3$/**ED8**	14.5	4.9	6.4	2.4	7.9
		14.4	5.0	7.0	2.5	8.0
C3		Untreated	5.8	9.8	-	-
	AlEt$_3$	14.1	4.7	9.6	-	13.9
		13.6	4.4	8.7	-	9.0
	AlEt$_3$/**ED1**	13.0	4.6	8.9	1.5	11.7
		15.1	4.5	8.8	1.8	12.2
	AlEt$_3$/**ED8**	14.1	4.6	8.9	2.0	12.4
		16.9	4.2	8.3	2.8	10.6
C4		Untreated	6.3	4.8	-	-
	AlEt$_3$	19.1	4.5	2.9	-	13.9
		20.1	5.2	2.9	-	12.6
	AlEt$_3$/**ED1**	16.2	4.1	1.4	7.2	9.4
		15.0	4.3	1.7	6.6	8.6
	AlEt$_3$/**ED8**	17.7	4.2	2.0	6.2	9.9
		17.3	4.4	2.0	5.7	8.8

Facts [a] and [b] are the aggregate of several concurring processes, on which the previous literature shed light only in part.[3,4,11,14,26,27,31] ID extraction by the AlR_3 may follow from an irreversible chemical reaction, or the formation of a strong Lewis acid-base adduct. A thorough kinetic study, which will be presented in Section 3.3, allowed to shed light on the reactivity between TEA and ester-based IDs, revealing a fast(er) reaction for dibutylphthalate than for 2,3-diisopropyldiethyl-succinate. 1,3-Dimethoxypropanes, in turn, do not react with AlR_3 compounds, but rapidly form adducts with them in solution.[3,4]
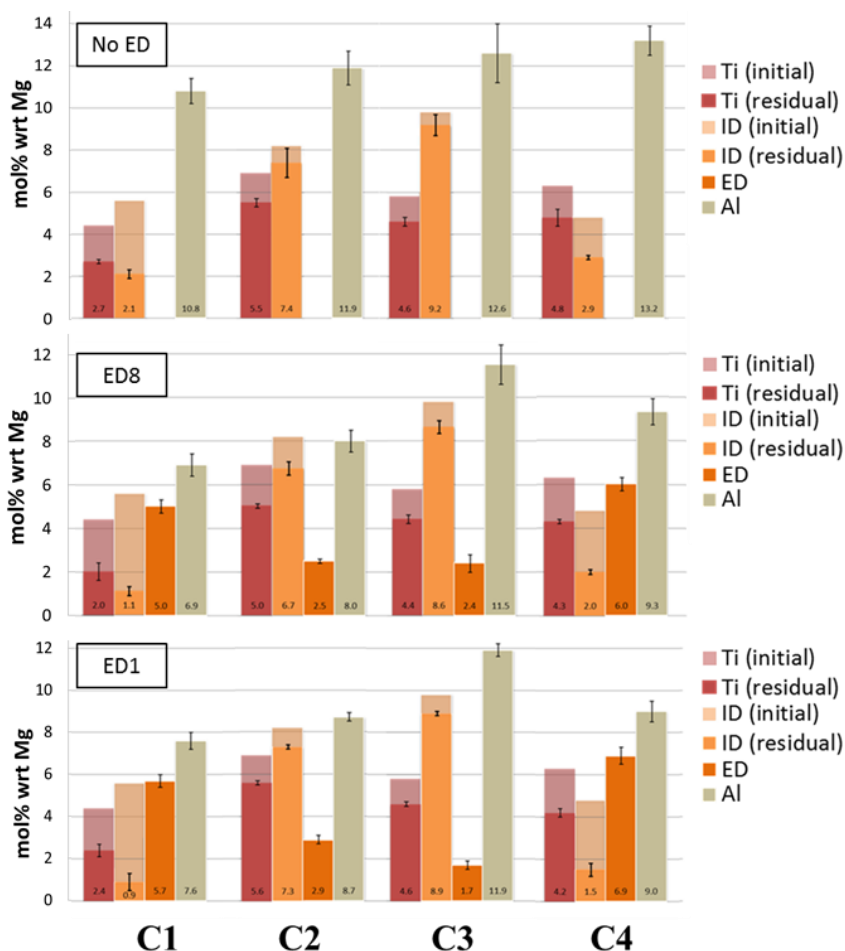
Figure 3.5. Evolution of catalyst composition upon reaction with $AlEt_3$(/ED).

According to the first seminal papers on fifth-generation ZN catalyst systems,[14,15] IDs with bulky substituents on C-2 (like e.g. 2,2-diisobutyl-1,3-dimethoxypropane in **C2**) are strongly bound to $MgCl_2(110)$ terminations, and their extraction by AlR_3 is marginal; on the other hand, less sterically demanding homologues (like 2,2-dimethyl-1,3-dimethoxypropane in **C3**) would adsorb much more weakly, because in a large fraction of low-energy conformers the two O atoms are too far apart to chelate tetracoordinated Mg (O∩O distance >3 Å).

The results presented here (Table 3.5 and Figure 3.5) do not endorse such a discrimination; as a matter of fact, the ID of catalyst **C3** turned out to be as extensively and firmly bound to the catalyst surface as that of catalyst **C2** (which is also in line with recent DFT calculations[32]).

We will come back to fact [c] at a later stage. Regarding fact [d], our ICP-OES determinations were not informative on the chemical nature of the Al adsorbates. $TiCl_4$ reduction by AlR_3 compounds is known to proceed with the formation of $AlR_{3-x}Cl_x$ species (in particular, $AlEt_2Cl$).[3-5] In the case of catalyst **C1**, $AlEt_2OBu$ was also formed, as a reduction product of the dibutylphthalate ID (see Section §3.3). Last but not least, fact [e] confirms the rather weak chemisorption of $TiCl_4$ onto $MgCl_2$;[19] we verified that the fraction of $TiCl_x$ lost to the liquid phase had negligible activity in propene polymerization under the conditions of this study, as was demonstrated by means of propene polymerization tests on the filtrates.

3.2.4. Catalyst QSAR

The impact of individual donor structures on catalyst performance can now be examined. As noted above, the screened EDs modulated very effectively the stereoselectivity of systems **C1**-$AlEt_3$/**EDx** and, to a lower extent, of **C4**-$AlEt_3$/**EDx** ones (Tables 3.4-A, 3.4-D, A3.1, A3.4 and Figures 3.3, 3.4). It is plausible to trace this finding to the observed ID/ED exchange (Table 3.5, Figure 3.5 and Section 3.3), that should result into a significant fraction of the catalytic species in **C1** and **C4** featuring neighboring ED molecules. We note at this point that the x numeral in the **EDx** (Table 3.3) identification codes of the screened alkoxysilanes was assigned ex-post, in such a way that a higher x corresponded to a higher stereoselectivity within the **C1**-$AlEt_3$/**EDx** series (Table 3.4-A). Notably, a very similar ordering turned out to hold for the **C4**-$AlEt_3$/**EDx** series too (Table 3.4-D

and Figure 3.3). In a first approximation, the steric crowding at the Si atom, that is to say next to the catalyst surface once the ED molecules get adsorbed, also grows with growing x (Table 3.3). This correlation is less obvious than it may appear; in fact, it suggests that for all alkoxysilanes in the set similar chemisorption modes ended up with comparable degrees of coverage at saturation (in mol per mol of Mg) for the available surfaces of each given catalyst;[23,33] the adsorption data of **ED1** and **ED8** (Figure 3.5) are compatible with such an assumption. If the hypothesis holds, then the lateral steric pressure experienced by the catalytic species, and hence their stereoselectivity according to the model of Ref[25] (see below), should grow with growing alkoxysilane steric demand, and attain a characteristic plateau value for each ED once surface saturation is reached; looking at Tables A3.1 and A3.4, this seems indeed to occur around [ED]/[Al] $\approx$ 0.05.

What does not seem to fit in the picture, on the other hand, is that systems **C1**-AlEt$_3$ and **C4**-AlEt$_3$ turned out to be slightly *more* stereoselective than **C1**-AlEt$_3$/**ED1** and **C4**-AlEt$_3$/**ED1** (Tables 3.4-A, 3.4-D and Figures 3.3, 3.4). Our explanation is that the chemisorbed Al species (Figure 3.5) surrogated the ED as ID replacements. AlEt$_3$ and AlEt$_2$Cl are strong Lewis acids, known for their self-dimerization equilibria;[34,35] in the monomeric state, they can form hetero-dinuclear adducts with Al-Cl-Mg and Al-Cl-Ti bridges.[3-5] Al-alkyl binding to TiCl$_3$ with formation of doubly-bridged Al-[(μ-Cl)(μ-Et)]-Ti moieties is strong,[36,37] and likely one of the reasons for the low concentration of active Ti measured in Quenched-Flow[38] or similar studies (see also Appendix of the Thesis). As far as binding to MgCl$_2$ is concerned, a recent DFT study concluded that AlEt$_{3-x}$Cl$_x$ chemisorption (x = 0, 1) on MgCl$_2$(104) facets is exergonic,[20] which is in line with the results in Figure 3.5. Based on our polymerization data (Figures 3.3, 3.4), the ability of adsorbed Al-alkyls to enhance catalyst stereoselectivity is similar or even slightly higher than that of small EDs (like e.g. **ED1**), but much poorer than for best-in-class EDs (e.g., **ED7** or **ED8**). It should be noted that the amount of chemisorbed Al on catalysts **C1** and **C4** was lower in the presence of an alkoxysilane (Figure 3.5), which we interpret as evidence for a competition; as a matter of fact, according to computational modeling data, alkoxysilanes prevail over AlEt$_{3-x}$Cl$_x$ species for adsorption on plain MgCl$_2$ crystal terminations.[20,23,39]

A completely different picture emerged for systems based on catalysts **C2** and **C3**, whose 1,3-dimethoxypropane IDs were the dominant donors in the adsorbate pool, leaving very limited room for ED action (Tables 3.4-B, 3.4-C, A3.2, A3.3, 3.5,

and Figures 3.3-3.5). Based on conventional wisdom, such ZN systems should be the easiest to interpret; as a matter of fact, the strong preference of their IDs for chemisorption on $MgCl_2$(110) terminations[14,15,33] is expected to determine the least differentiated surface environment (which indeed is consistent with the comparatively narrow molecular weight distribution of the produced polymers). Yet, computational modeling studies[39] indicated that 1,3-dimethoxypropanes on plain $MgCl_2$(110) facets, irrespective of the steric bulk of the alkyl substituents on C-2, cannot get close enough to adjacent $TiCl_2R$ catalytic species to make them highly stereoselective in propene insertion (see following section). The data in Table 3.5 and Figure 3.5, demonstrating unexpectedly that large amounts of Al species were chemisorbed on both catalysts **C2** and **C3**, despite the presence of the ID and with little (catalyst **C2**) or practically no (catalyst **C3**) evidence of competition with the ED when used, can provide a solution to this puzzling problem, as will be illustrated in the next section.

3.2.5. *Preliminary computational models of the catalytic species*

A tentative interpretation of the phenomenological picture of the previous sections can be made in terms of suitable models of ZN catalytic species. Different approaches have been reported to quantify the number of such species. Simulations of PP MWDs as summations of Schulz-Flory functions ended up with a minimum of four components;[40] however, this method cannot discriminate between chemical and physical effects on the MWD, and the possibility of overdetermined solutions is high because the poor resolution and limited precision of MWD data complicate the evaluation of model significance. A more robust approach, in our opinion, is based on the statistical analysis of high-resolution ^{13}C NMR stereosequence distributions.[13,25] This identified three basic types of stereosequences, namely highly isotactic, weakly isotactic ('isotactoid'), and syndiotactic;[13,25] the plausible assumption of a corresponding number of distinct *families* of catalytic species was translated into the three-site model of Ref[25]. Here it is possible to propose an updated version, assuming that all catalytic species are mononuclear Ti(III) surface adducts with the structure of Figure 3.6, in line with the indications of recent Raman[41] and high-resolution ESR[42] studies, and of the latest DFT calculations.[19,20]
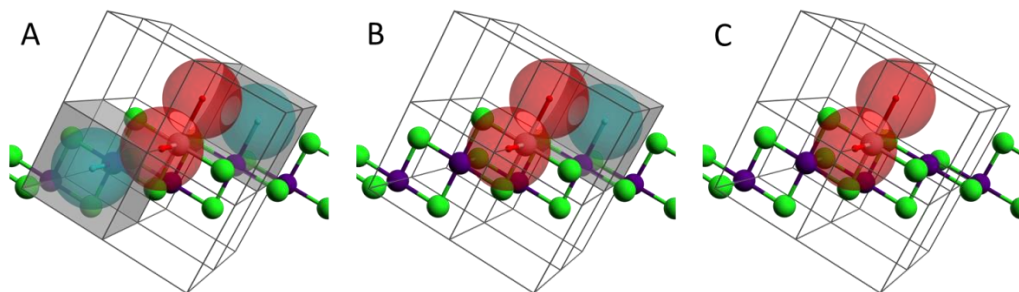
Figure 3.6. Updated three-site model for ZN catalysts (see text and Ref.[25]). Mg and Cl atoms are colored in violet and green, respectively. The large spheres in red highlight the two active Ti sites according to the Cossee insertion mechanism; those in light blue, the surface Mg sites where the presence of an adsorbate would hinder one of the two octants (in light grey) where the first chain C-C bond could be located. Chain propagation is predicted to be highly isotactic in case (A); weakly isotactic in case (B); chain-end-controlled syndiotactic in case (C).

The first coordination sphere of Ti is octahedral and C_2-symmetric (like in crystalline TiCl$_3$);[13] steric hindrance in the second coordination sphere, on the other hand, can vary. Assuming a Cossee-type chain migratory insertion mechanism,[6,13] highly isotactic chain propagation requires that the active sites are sterically constrained at two diagonal octants out of the four where the first C-C bond of the growing polymer chain can be located in the 1,2 propene insertion transition state, thus locking chain conformation in the desired chiral orientation and ensuring site (pseudo)homotopicity (Figure 3.6-A).[13] Such a condition can be met when adsorbates with adequate bulk occupy the adjacent surface just at the limit still allowing fast monomer access to the Ti center with the favored enantioface, and are under strong lateral pressure by the neighboring co-adsorbate pool, freezing diffusion phenomena[43,44] or even hindering conformational motions. Should said steric pressure fade, the enantioselectivity will decrease, because the conformational constraints on the growing chain weaken, and the chiral active pockets become too loose. Depending on the extent of said fading, and whether only one octant or both octants is/are involved, chain propagation will deteriorate to weakly isotactic (Figure 3.6-B), or even chain-end-controlled syndiotactic (Figure 3.6-C).[13,25] In case of a dynamic character of the interested surfaces, stereoblock chains may form.[13,25]

The distribution of the three basic cases of Figure 3.6 (i.e. close/close, close/open, open/open octants) is a function of the adsorbate pool. In the previous sections, we reported experimental evidence that said pool includes not only donors, but also Al-alkyls. Looking at the recent literature,[20,39] it appears that models of TiCl$_4$

adsorbates at defective locations of $MgCl_2(104)$-like edges exposing tetracoordinated Mg are not incompatible with the hypothesis of an effective steric modification by adjacent alkoxysilane EDs (even if explicit calculations are still pending). A case where the cooperation of Al-alkyls is required, on the other hand, seems that of fifth-generation catalysts. Figure 3.7-A shows a computational model[45] of a portion of plain $MgCl_2(110)$ edge accommodating a $TiCl_4$ unit and an adjacent 2,2-dimethyl-1,3-dimethoxypropane molecule in the minimum energy structure; it is evident on inspection, and was confirmed by calculation, that the two co-adsorbates are too far apart to give rise to a catalytic species falling under the case of Figure 3.6-A.
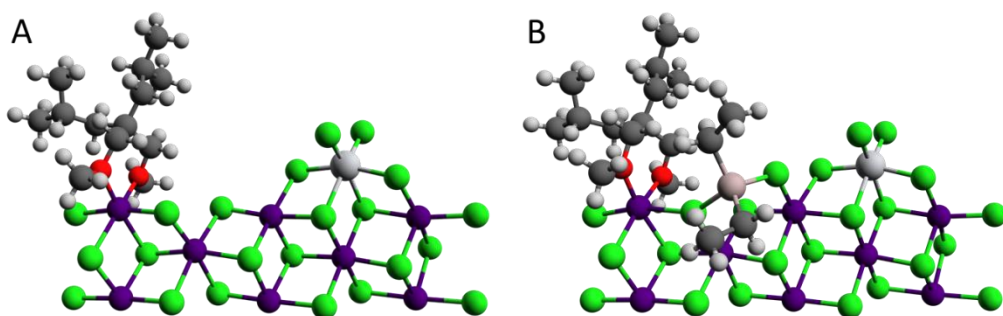
Figure 3.7. (A) DFT model of adjacent $TiCl_4$ and 2,2-diisobutyl-1,3-dimethoxypropane co-adsorption on a $MgCl_2(110)$ edge. (B) The same after the adsorption of an $AlEt_2Cl$ molecule (see text). Color key: Mg/Violet; Ti/Light grey; Al/Pink; Cl/Green; O/Red; C/Dark grey.

Figure 3.7-B shows the same fragment with an additional $AlEt_2Cl$ molecule chemisorbed in between the two aforementioned adsorbates; the calculated free energy of adsorption was ΔG_{ads} = -7.9 kcal mol^{-1}. Notably, even small alkoxysilane molecules like **ED1** were estimated to be too bulky to effectively compete with the $AlEt_2Cl$ moiety for chemisorption at that specific surface vacancy. For propene insertion at the catalytic species formed by alkylation and reduction of the $TiCl_4$ precursors in Figure 3.7-A and 3.7-B, we calculated $\Delta G_{re/si} \approx 0$ and 1.5 kcal mol^{-1}, respectively; the latter is in good agreement with experiment (Table 3.4-C). Conformational interlocking of ID and $AlEt_2Cl$ seems to enhance stereorigidity; with bulkier 1,3-dimethoxypropanes this can only be more severe (calculations are running). The presence of ED molecules at distal surface locations can also contribute to enforce the necessary lateral steric pressure (Figures 3.3-3.5).

3.3. A kinetic study of the reactivity of ester IDs with AlEt$_3$

3.3.1. Kinetic study in solution

As noted before[27,31,46], and confirmed in the previous section, typical ester IDs react irreversibly with AlR$_3$ compounds, and are extracted from the solid phase of ZN catalysts in the polymerization medium. According to the literature, the reaction of ethylbenzoate (EB) with excess AlEt$_3$ proceeds through three distinct stages (Scheme 3.1): (i) the rapid formation of Lewis acid-base adduct **I**, (ii) a somewhat slower bimolecular reaction between this adduct and 'free' AlEt$_3$ (nucleophilic acyl substitution), and (iii) loss of Et$_2$AlOEt from **II** to form **III**, which rapidly reacts with a third AlEt$_3$ molecule (nucleophilic addition), yielding several Al-alkoxy species.[47] Overall, two moles of AlEt$_3$ are consumed per mole of ester while a third mole of AlEt$_3$ is converted to the hemialkoxide.
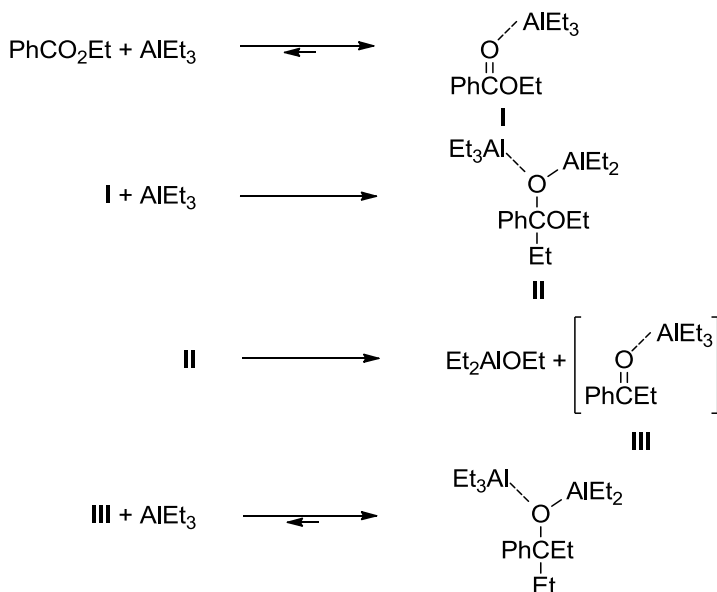
Scheme 3.1. Reaction of **EB** with AlEt$_3$.

A similar process is reported to occur with phthalates.[3–5] Our own results (§3.2.3) indicated that not only a phthalate ID, but also a succinate ID, can be lost to the solution phase and replaced by an alkoxysilane ED on the catalytic surfaces. It seems reasonable to speculate that the reactivity of succinates with AlR_3 is comparable with that of benzoates and phthalates, and trace the observed ID/ED exchange to that. On the other hand, no literature data is available to validate this guess. To address this problem, a variable temperature (VT) ^{1}H-NMR kinetic study on the reaction between $AlEt_3$ and three prototypical esters normally used as IDs (Figure 3.7) in toluene solution has been carried out.

**ethylbenzoate
(EB)**

**dibutylphthalate
(DBP)**

**diethyl-2,3-diisobutylsuccinate
(DiBS)**
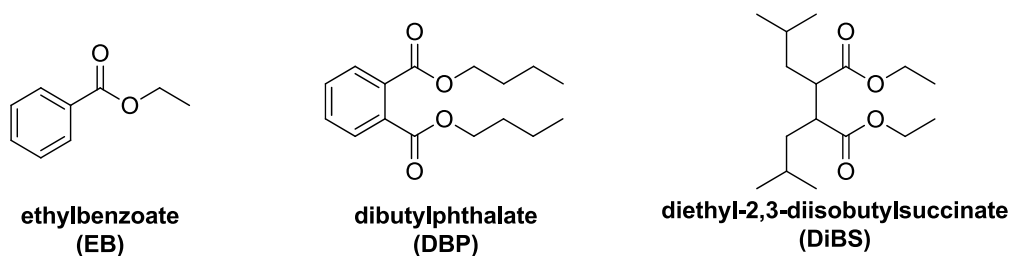
Figure 3.7. The three investigated ester IDs.

Figure 3.8 shows part of the ^{1}H NMR spectrum in toluene-d_8 of neat DBP (A) and of its reaction product(s) with excess $AlEt_3$ at 30°C after approximately 10, 20, 40 and 150 min. Upon addition of $AlEt_3$, the triplet of the methylene protons (4.18 ppm) of the OCH_2R group of DBP is shifted downfield by $\sim$0.1 ppm (Figure 3.8-B-E), indicating that the formation of an $AlEt_3$-DBP adduct is fast and complete. As the reaction proceeds (Scheme 1), the intensity of this signal decreases and a triplet at 3.57 ppm appears (Figure 3.8-B-E), owing to the formation of Et_2AlOBu (or Et_5Al_2OBu).
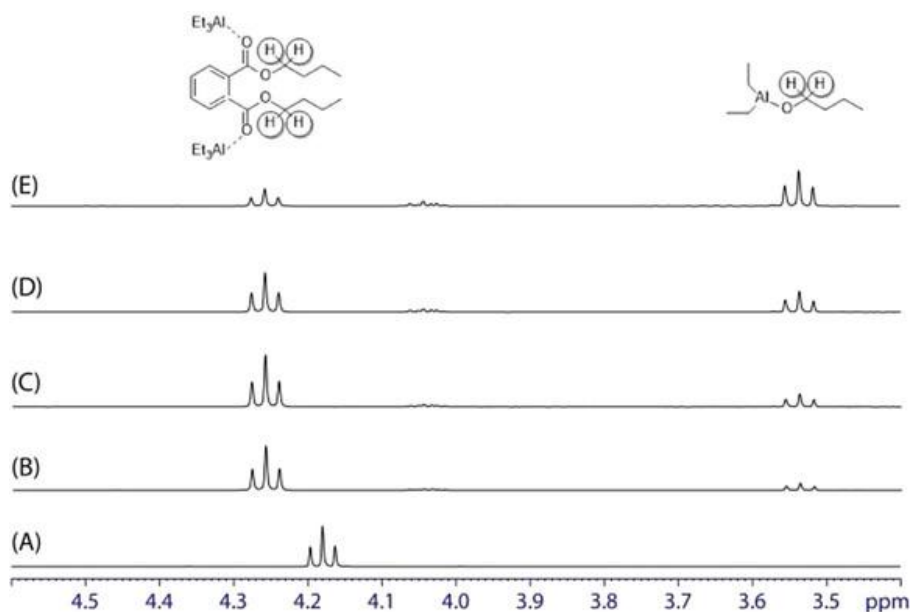
Figure 3.8. Excerpt of the ^{1}H NMR spectrum in toluene-d_8 of (A) neat DBP and its reaction with AlEt$_3$ at 30°C after (B) 10, (C) 20, (D) 40, and (E) 150 min.

For all three investigated molecules, residual donor concentrations as a function of time were calculated from the integrals of the OCH_2R protons (centered at approximately δ = 4.26 ppm (t) for DBP, δ = 4.05 ppm (m) for DiBS, and δ = 4.00 ppm (q) for EB). Mesitylene (δ = 2.13 ppm) was used as an internal standard. Identical results (within the error bar) were obtained from the integrals of the alkoxy protons of the formed Et$_2$AlOR.

Plots of ln([ID(t)]/[ID(0)]) versus t generated a straight line with R^2 always greater than 0.95 (Figure 3.9), which indicates that the reaction is pseudo-first-order with respect to [ID]. The slopes of the interpolating straight lines were used to determine the apparent kinetic constants for the reactions of the three donors with AlEt$_3$ at five different temperatures (Table 3.6).

Apparent activation parameters were determined from Eyring plots (Figure 3.10 and Table 3.7). We observed significantly negative activation entropy values for all three donors, likely traceable to the participation of a second AlEt$_3$ molecule in

the rate-limiting nucleophilic substitution step (Scheme 3.1). Most notable, however, is the large variation in activation enthalpy for the three donors, from ~8 kcal mol^{-1} for the relatively unhindered EB molecule to 18 kcal mol^{-1} for the highly hindered DiBS molecule. A relationship between alkylation rate and steric hindrance has been noted before for monoesters;[47] it seems likely that in the present case the lower reactivity of DBP and especially DiBS is also attributable to steric factors.
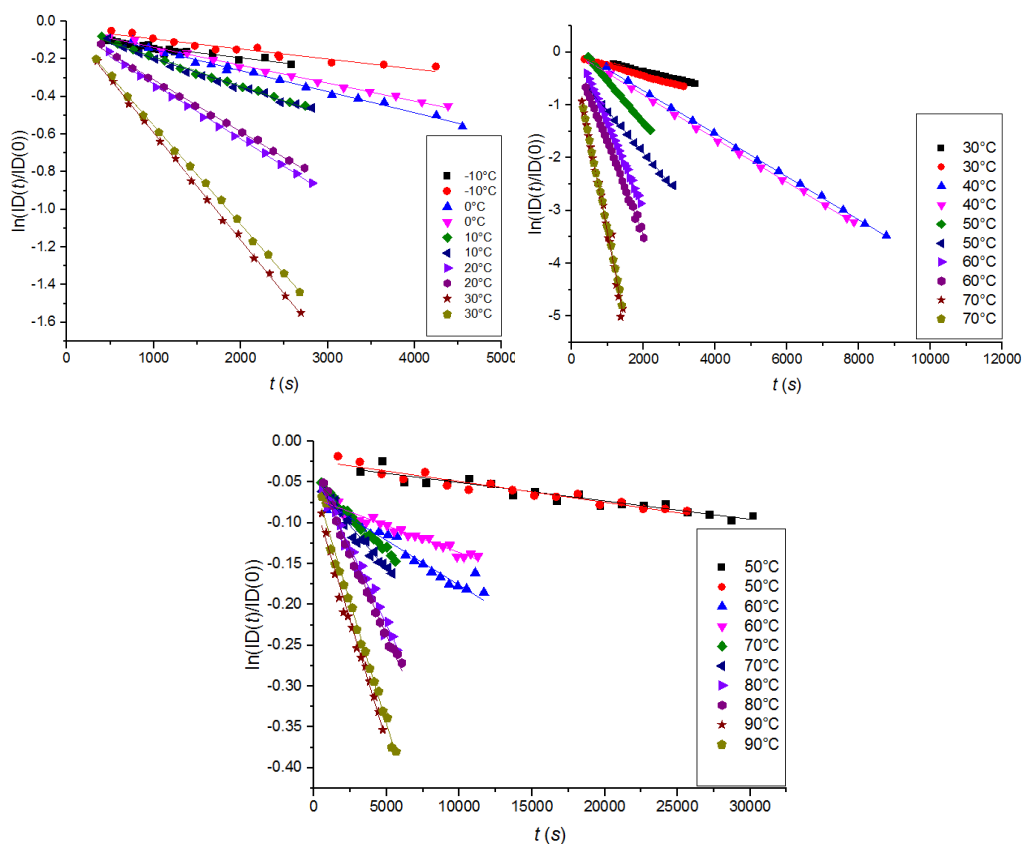
Figure 3.9. Plots of $\ln([ID(t)]/[ID(0)])$ *vs.* t for the reaction between the IDs and AlEt$_3$ at five different temperatures. Top-left: EB; top-right: DBP; bottom: DiBS.

Table 3.6. Apparent kinetic constants of the reactions of EB, DBP, and DiBS with AlEt$_3$ in toluene at five different temperatures.[a]

ID	T (°C)	k_{app} (10^4) (s^{-1}) [b]	
	-10	0.55 ± 0.04	0.53 ± 0.04
	0	1.11 ± 0.03	0.95 ± 0.02
EB	10	1.55 ± 0.03	1.54 ± 0.05
	20	2.91 ± 0.04	2.76 ± 0.04
	30	5.7 ± 0.04	5.26 ± 0.03
	30	1.62 ± 0.02	1.92 ± 0.02
	40	4.07 ± 0.02	4.13 ± 0.03
DBP	50	8.06 ± 0.05	7.90 ± 0.06
	60	16.30 ± 0.08	17.5 ± 0.1
	70	35.2 ± 0.9	33.9 ± 0.2
	50	0.022 ± 0.002	0.025 ± 0.002
	60	0.109 ± 0.005	0.066 ± 0.003
DiBS	70	0.179 0.006	0.21 ± 0.01
	80	0.37 ± 0.01	0.411 ± 0.008
	90	0.59 ± 0.02	0.59 ± 0.01

[a]In toluene-d_8 (550 uL), ID/AlEt$_3$ = 0.04 [b]Two independent determinations of k_{app} for each temperature.
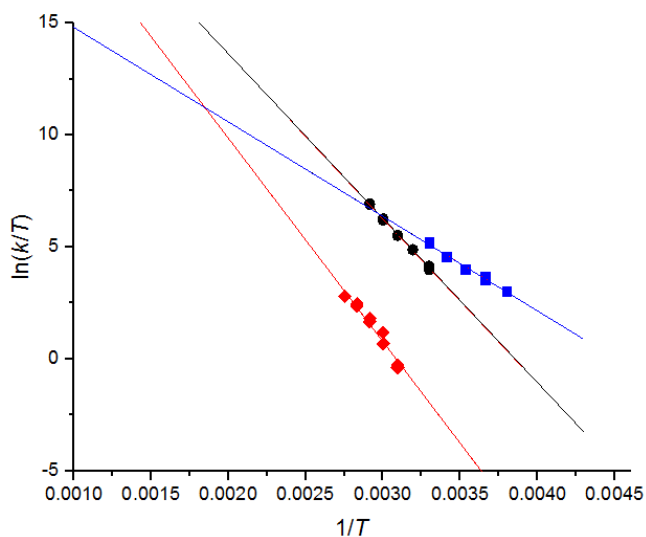
Figure 3.10. Eyring plots of the data in Table 3.6. (Blue) EB + AlEt$_3$ (R^2 = 0.984); (Black) DBP + AlEt$_3$ (R^2 = 0.997); (Red) DiBS + AlEt$_3$ (R^2 = 0.954).

Table 3.7. Activation parameters for the reaction between EB, DBP and DiBS with AlEt$_3$ in toluene (see also Scheme 3.1)

System	$\Delta S^{\#}_{exp}$ (cal mol^{-1} K^{-1})	$\Delta H^{\#}_{exp}$ (kcal mol^{-1})	$\Delta H^{\#}_{DFT}$ (kcal mol^{-1})
EB/AlEt$_3$	-46 ± 1	8.4±0.3	15.7
DBP/AlEt$_3$	-28 ± 1	14.6±0.4	19.9
DiBS/AlEt$_3$	-28 ± 4	18.0±1.0	24.6

From the mechanistic standpoint these reactions are complex, and involve more than one equivalent of AlEt$_3$ in the rate-limiting step. Also, there is some uncertainty in the literature about the nature of the nucleophilic substitution transition state (TS): both four-center and six-center TSs have been considered.[48] Recently, Vanka and co-workers published an extensive computational study in which only a six-center TS was considered.[49] A systematic exploration of these reactions by means of DFT calculations has been started. Initial results support a four-center TS assisted by the coordination of an additional AlEt$_3$ molecule to the carbonyl oxygen (Figure 3.11). These results, included in Table 3.7 (for details see Ref[30]), support the observed reactivity trends and are in good agreement with the experimental data.
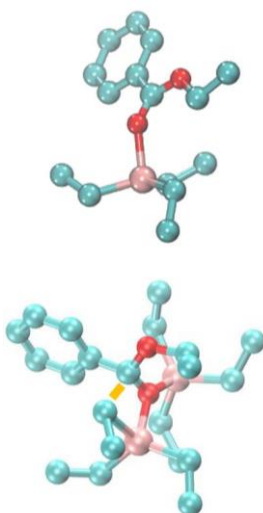
Figure 3.11. Optimized DFT geometries of adduct (top) and alkylation TS (bottom) for reaction of EB with AlEt$_3$.

3.3.2. Kinetic study in heterogeneous phase

Based on the results in Table 3.7 and Figure 3.10, one can conclude that at temperatures of relevance for industrial propene polymerization (70-80°C) EB and DBP react with $AlEt_3$ at similar rates, whereas the reaction of DiBS and $AlEt_3$ is slow to the point that it may be ignored. Yet, as shown in Sections 3.2.2 and 3.2.3 (Figures 3.3 and 3.5), ID/ED exchange does occur in the succinate-containing catalyst **C4**. This may be interpreted either by assuming that the results of the kinetic studies in solution are not representative of the reactivity on catalytic surfaces, or that an irreversible reaction between the ID and $AlEt_3$ is *not* a necessary requirement for ID surface clean-up.

In order to address this question, a series of activation experiments in heptane slurry at 40°C and 70°C for three different $MgCl_2$/ID/$TiCl_4$ precatalysts with $AlEt_3$ were designed and performed. Precatalysts **C1** (ID = DBP) and **C4** (ID = DiBS) of Section 3.2.1, and a homologue with ID = EB, were reacted with $AlEt_3$ for 30 min according to the protocol already described in Sections 2.4.2 and 3.2.3. The results are reported in Table 3.8, as averages of duplicate experiments.

Table 3.8. Evolution of catalyst composition upon reaction with $AlEt_3$.

Catalyst	T (°C)	ID (mol/mol Mg × 100)		Retained ID, %
		Without $AlEt_3$	With $AlEt_3$	
$MgCl_2$/**EB**/$TiCl_4$		14.7	4.7±0.2	32
$MgCl_2$/**DBP**/$TiCl_4$	70	5.6	2.1±0.2	38
$MgCl_2$/**DiBS**/$TiCl_4$		4.8	2.9±0.1	60
$MgCl_2$/**EB**/$TiCl_4$		14.7	7.1±0.5	48
$MgCl_2$/**DBP**/$TiCl_4$	40	5.5	4.2±0.4	76
$MgCl_2$/**DiBS**/$TiCl_4$		4.8	3.4±0.1	71

At 40°C, 76% DBP and less than 50% EB was retained in the activated solid phase. At 70°C, close to the crossover temperature of Figure 3.10, the amount of retained ID was about 35% in both cases. This is nicely in line with the reactivity measured in solution (Table 3.7). On the other hand, 30% (40%) DiBS was extracted at 40°C

(70°C), whereas nearly quantitative retention should have been expected based on the reactivity in solution.

A more thorough study was carried out for precatalyst **C1** (ID = DBP).The HTE workflow and protocol described in §2.4.2 were used to react it with $AlEt_3$ ([Al]/[Ti] = 25) at 40, 60, 80 and 100°C in the time range of 5 to 120 min. The experimental results are summarized in Figures 3.12-3.14 and Tables A3.5-A3.8 (for the latter see the Appendix at the end of this Chapter).
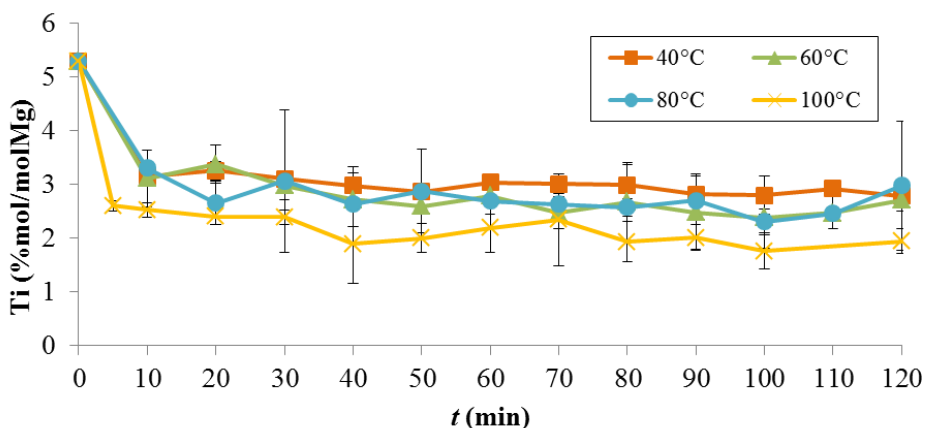
Figure 3.12. Residual Ti content in the solid phases recovered after reacting precatalyst **C1** ($MgCl_2/TiCl_4/DBP$) with $AlEt_3$ in heptane at 40°C, 60°C, 80°C and 100°C (data from Tables A3.5-A3.8). Error bars are based on the average absolute deviation.
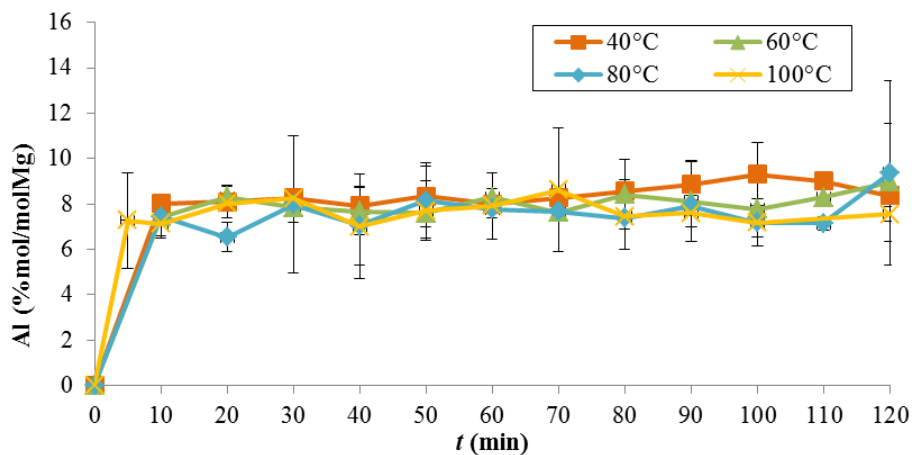
Figure 3.13. Al content in the solid phases recovered after reacting precatalyst **C1** ($MgCl_2/TiCl_4/DBP$) with $AlEt_3$ in heptane at 40°C, 60°C, 80°C and 100°C (data from Tables A3.5-A3.8). Error bars are based on the average absolute deviation.
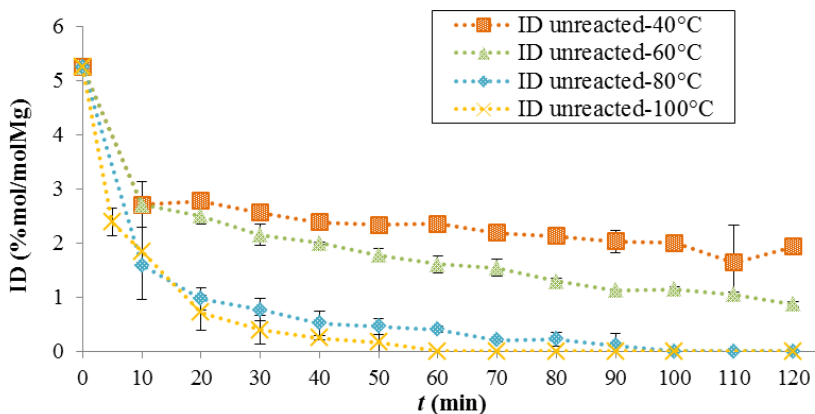
Figure 3.14. Residual unreacted DBP content in the solid phases recovered after reacting precatalyst **C1** (MgCl$_2$/TiCl$_4$/DBP) with AlEt$_3$ in heptane at 40°C, 60°C, 80°C and 100°C (data from Tables A3.5-A3.8). Error bars are based on the average absolute deviation.

Contacting the precatalyst with TEA in heptane slurry resulted into profound changes of solid composition. ICP-OES analyses pointed out that about 50% of the Ti species were extracted, already within the first minutes of reaction and almost independently of the reaction temperature; past that time, no further Ti leaching was observed over two hours. As was noted before, this fraction of Ti lost to the liquid phase is inactive in propene polymerization. At the same time, a major uptake of Al took place, up to [Al]/[Ti] ≈ 3 to 4; unfortunately, ICP-OES is not informative on the nature of the Al species, although it is plausible that they include chemisorbed AlEt$_{3-x}$Cl$_x$ species, adducts with chemisorbed donors, and hetero-dinuclear adducts with alkylated Ti(III) species.

Regarding the ID, that it would be largely removed was expected. In particular, under this set of experimental conditions an extensive surface clean-up, ranging from ≈35% at 40°C to >95% at 100°C, was achieved. Plots of ln([ID(t)]/[ID(0)]) versus t could be well interpolated by straight lines (R^2 always >0.89), which indicates that the reaction is pseudo-first-order with respect to the ID (Figure 3.15). The slopes of said interpolating straight lines were used to determine the apparent kinetic constants for the reaction at four different temperatures (Table 3.9). The apparent activation parameters were calculated from the Arrhenius plot (Figure 3.16).
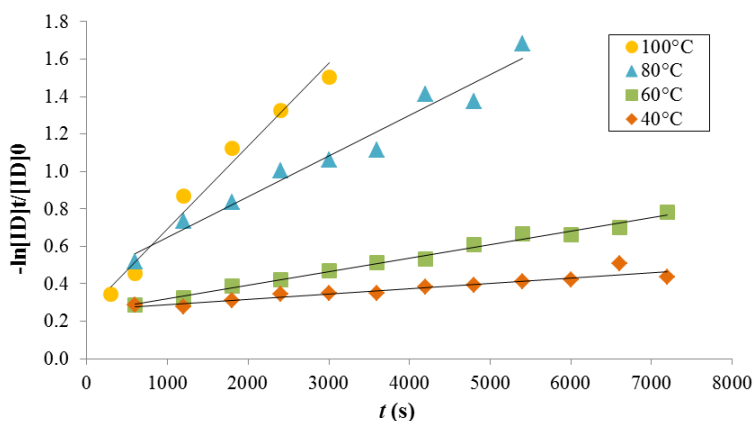
Figure 3.15. VT plots of -ln([ID(t)]/[ID(0)]) vs t. Correlation coefficients were R^2 = 0.89 at 40°C, 0.99 at 60°C, 0.97 at 80°C, and 0.98 at 100°C.

Table 3.9. Apparent kinetic constants and activation parameters for the reaction of AlEt$_3$ with DBP in catalyst **C1** in heptane slurry.

T (°C)	k_{app} (s^{-1})	$\Delta H^{\#}$ (kcal mol^{-1})	$\Delta S^{\#}$ (cal mol^{-1} K^{-1})
40	$2.9 \cdot 10^{-5} \pm 3 \cdot 10^{-6}$		
60	$7.2 \cdot 10^{-5} \pm 2 \cdot 10^{-6}$	10.1 ± 0.5	-47 ± 1
80	$2.2 \cdot 10^{-4} \pm 1 \cdot 10^{-5}$		
100	$4.4 \cdot 10^{-4} \pm 4 \cdot 10^{-5}$		
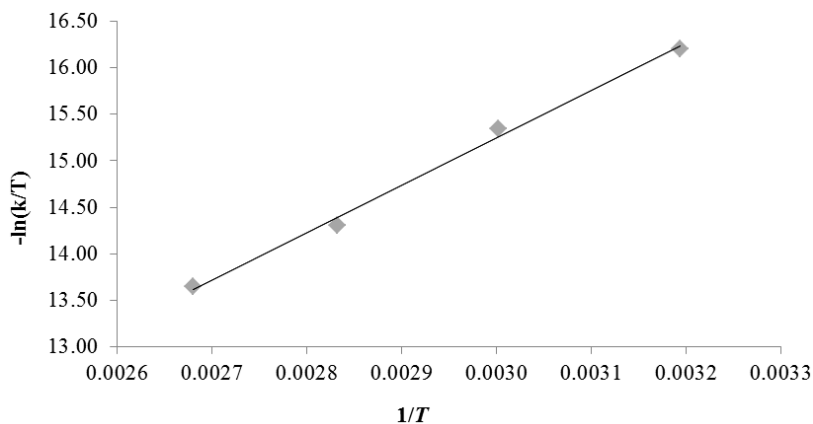
Figure 3.16. Arrhenius plot for the k_p values in Table 3.9 (R^2 = 0.996).

The values of $\Delta H^{\#}$ and $\Delta S^{\#}$ in Table 3.9 are in remarkably good agreement with those obtained for the reaction between DBP and AlEt$_3$ in solution (Table 3.7).

The possible impact of an alkoxysilane ED in solution on the reaction kinetics was also investigated. To this end, dicyclopentyldimethoxysilane (**ED8** of Table 3.3) and diethylaminotriethoxysilane (**ED6** of Table 3.3) were added to AlEt$_3$ ([Al]/[Si] = 0.10), and the measurements at 80°C with AlEt$_3$ alone were repeated under the very same conditions. The amount of chemisorbed ED was measured by ^{1}H NMR similarly to what was reported for DBP, by integrating the signals of the protons α to Si or of the methoxy ones. The results are shown graphically in Figures 3.17 and 3.18.
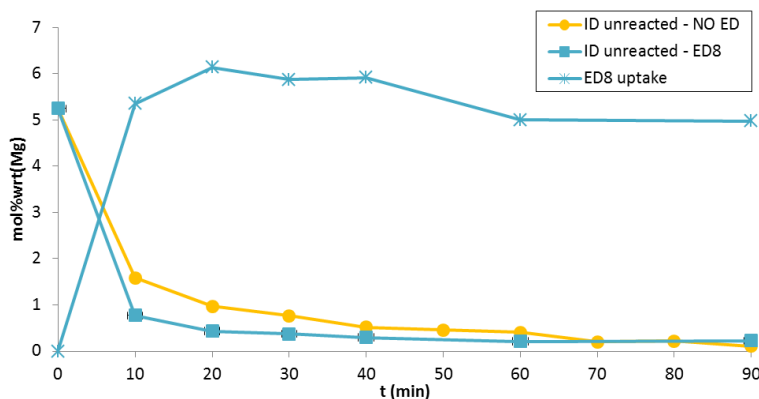
Figure 3.17. Contents of unreacted DBP [ID] and **ED8** in the solid phases recovered after reacting precatalyst **C1** (MgCl$_2$/TiCl$_4$/DBP) with AlEt$_3$/**ED8** in heptane slurry at 80°C. Comparative data for the reaction with AlEt$_3$ alone are also shown for comparison.
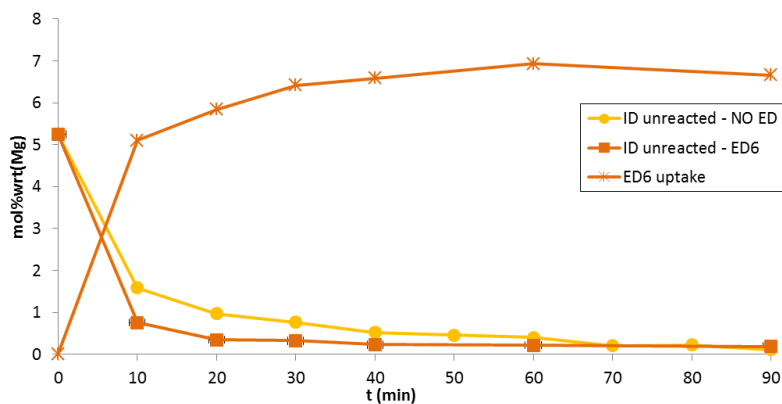
Figure 3.18. Contents of unreacted DBP [ID] and **ED6** in the solid phases recovered after reacting precatalyst **C1** (MgCl$_2$/TiCl$_4$/DBP) with AlEt$_3$/**ED6** in heptane slurry at 80°C. Comparative data for the reaction with AlEt$_3$ alone are also shown for comparison.

DBP desorption was only slightly faster in the presence of an ED; at the same time, the latter adsorbed at an amount suggesting an extensive replacement of the former on the surface.

Overall, we conclude that the reaction kinetics between $AlEt_3$ and the three investigated IDs is similar in solution and on catalytic surfaces. Therefore, an irreversible reaction of the ID with $AlEt_3$ unquestionably favors ID removal and ID/ED exchange, but at the same time it is not a mandatory requirement.

At this point it is worthy to recall that all IDs investigated in this project (i.e. EB, DBP, DiBS as well as 1,3-dimethoxypropanes) form reversibly Lewis acid-base adducts with $AlEt_3$. Interestingly, DFT modeling results[30] indicate that the formation free energy for the adduct of DiBS with $AlEt_3$ is higher by ca. 4 kcal mol^{-1} than those of representative 1,3-dimethoxypropanes.[29] Tentatively, we suggest that the competition between $AlEt_3$ and the surface for binding to an ID is in favor of the surface for ID = 1,3-dimethoxypropane, and more balanced for ID = DiBS.

In concluding this Section, we note that the chemistry presiding over the ID/ED exchange in a ZN catalyst formulation is extremely relevant with respect to application. An ID which gives way to the ED represents a great opportunity to tailor the catalytic surfaces for a desired behavior of the catalytic species. Phthalate IDs belong in this category, but – as we have seen before – their industrial future is uncertain.[1] Identifying convenient alternatives is important and urgent; in this respect too, a HTE approach is highly desirable.

References

(1)   Ali, S. . *Catal. Rev.* **2014**, *27*, 7–14.

(2)   Boor, J. J. *Ziegler-Natta Catalysts and Polymerizations*; Academic Press: New York, 1979.

(3)   Cecchin, G.; Morini, G.; Piemontesi, F. Ziegler-Natta Catalysts. In *Kirk-Othmer Encyclopedia of Chemical Technology*; Seidel, A., Ed.; John Wiley & Sons, Inc.: Hoboken, NJ, 2007; pp 502–554.

(4)   Pasquini, N. *Polypropylene Handbook, 2nd Ed.*; Hanser Publisher: Munich, 2005.

(5)   Busico, V. Giulio Natta and the Development of Stereoselective Propene Polymerization. In *Polyolefins: 50 years after Ziegler and Natta I.*; Kaminsky, W., Ed.; Springer: Heidelberg, 2013; pp 37–58.

(6)   Arlman, E. J.; Cossee, P. Ziegler-Natta Catalysis III. Stereospecific Polymerization of Propene with the Catalyst System $TiCl_3/AlEt_3$. *J. Catal.* **1964**, *3* (1), 99–104.

(7)   Zambelli, A.; Sacchi, M. C.; Locatelli, P.; Zannoni, G. Isotactic Polymerization of α-Olefins: Stereoregulation for Different Reactive Chain Ends. *Macromolecules* **1982**, *15* (1), 211–212.

(8)   Corradini, P.; Barone, V.; Fusco, R.; Guerra, G. Analysis of Models for the Ziegler-Natta Stereospecific Polymerization on the Basis of Non-Bonded Interactions at the Catalytic Site—I. The Cossee Model. *Eur. Polym. J.* **1979**, *15* (12), 1133–1141.

(9)   Corradini, P.; Guerra, G.; Fusco, R.; Barone, V. Analysis of Models for the Ziegler-Natta Stereospecific Polymerization on the Basis of Non-Bonded Interactions at the Catalytic Site—I. The Cossee Model. *Eur. Polym. J.* **1980**, *16*, 835–842.

(10)   Busico, V.; Cipullo, R. Microstructure of Polypropylene. *Prog. Polym. Sci.* **2001**, *26* (3), 443–533.

(11)   Corradini, P.; Barone, V.; Fusco, R.; Guerra, G. A Possible Model of Catalytic Sites for the Stereospecific Polymerization of Alpha-Olefins on 1st-Generation and Supported Ziegler-Natta Catalysts. *Gazz. Chim. Ital.* **1983**, *113*, 601–607.

(12)   Cecchin, G.; Morini, G.; Piemontesi, F.; Seidel, A. . *Kirk-Othmer Encyclopedia of Chemical Technology*; Wiley Interscience: New York, 2007; p Vol. 26.

(13)   Busico, V.; Cipullo, R. Microstructure of Polypropylene. *Prog. Polym. Sci.* **2001**, *26* (3), 443–533.

(14)   Albizzati, E.; Giannini, U.; Morini, G.; Galimberti, M.; Barino, L.; Scordamaglia, R. . *Macromol. Symp.* **1995**, *89*, 73–89.

(15)   Scordamaglia, R.; Barino, L. . *Macromol. Theory Simul.* **1998**, *7* (4), 399–405.

(16)   Morini, G.; Albizzati, E.; Balbontin, G.; Mingozzi, I.; Sacchi, M. C.; Forlini, F.; Tritto, I. . *Macromolecules* **1995**, *89*, 73–89.

(17)   Seth, M.; Margl, P. M.; Ziegler, T. A Density Functional Embedded Cluster Study of Proposed Active Sites in Heterogeneous Ziegler-Natta Catalysts. *Macromolecules* **2002**, *35* (20), 7815–7829.

(18)   Boero, M.; Parrinello, M.; Weiss, H.; Hüffer, S. A First Principles Exploration of a Variety of Active Surfaces and Catalytic Sites in Ziegler-Natta Heterogeneous Catalysis. *J. Phys. Chem. A* **2001**, *105* (21), 5096–5105.

(19)   D'Amore, M.; Credendino, R.; Budzelaar, P. H. M.; Causá, M.; Busico, V. A Periodic Hybrid DFT Approach (Including Dispersion) to $MgCl_2$-Supported Ziegler–Natta Catalysts – 1: $TiCl_4$ Adsorption on MgCl2 Crystal Surfaces. *J. Catal.* **2012**, *286*, 103–110.

(20)   Credendino, R.; Liguori, D.; Fan, Z.; Morini, G.; Cavallo, L. Toward a Unified Model Explaining Heterogeneous Ziegler–Natta Catalysis. *ACS Catal.* **2015**, *5* (9), 5431–5435.

(21)   Busico, V.; Causà, M.; Cipullo, R.; Credendino, R.; Cutillo, F.; Friederichs, N.; Lamanna, R.; Segre, A.; Van Axel Castelli, V. Periodic DFT and High-Resolution Magic-Angle-Spinning (HR-MAS)^{1}H NMR Investigation of the Active Surfaces of $MgCl_2$-Supported Ziegler-Natta Catalysts. the $MgCl_2$ Matrix. *J. Phys. Chem. C* **2008**, *112* (4), 1081–1089.

(22)   Credendino, R.; Pater, J. T. M.; Correa, A.; Morini, G.; Cavallo, L. Thermodynamics of Formation of Uncovered and Dimethyl Ether-Covered MgCl2 Crystallites. Consequences in the Structure of Ziegler-Natta Heterogeneous Catalysts. *J. Phys. Chem. C* **2011**, *115* (27), 13322–13328.

(23)   Capone, F.; Rongo, L.; D'Amore, M.; Budzelaar, P. H. M.; Busico, V. Periodic Hybrid DFT Approach (Including Dispersion) to $MgCl_2$-Supported Ziegler–Natta Catalysts. 2. Model Electron Donor Adsorption on $MgCl_2$ Crystal Surfaces. *J. Phys. Chem. C* **2013**, *117* (46), 24345–24353.

(24)   D'Amore, M.; Thushara, K. S.; Piovano, A.; Causà, M.; Bordiga, S.; Groppo, E. Surface Investigation and Morphological Analysis of Structurally Disordered $MgCl_2$ and $MgCl_2$/$TiCl_4$ Ziegler–Natta Catalysts. *ACS Catal.* **2016**, *6* (9), 5786–5796.

(25)   Busico, V.; Cipullo, R.; Monaco, G.; Talarico, G.; Vacatello, M.; Chadwick, J. C.; Segre, A. L.; Sudmeijer, O. High-Resolution 13 C NMR Configurational Analysis of Polypropylene Made with $MgCl_2$-Supported Ziegler–Natta Catalysts. 1. The "Model" System $MgCl_2$/$TiCl_4$–2,6-Dimethylpyridine/$Al(C_2H_5)_3$. *Macromolecules* **1999**, *32* (13), 4173–4182.

(26)   Busico, V.; Corradini, P.; Martino, L. De; Proto, A.; Mezzocannone, V.; Albiuati, E.; Donegani, I. G.; Novara, C. R. Effects of the Co-Catalyst Composition. **1986**, *1124*, 1115–1124.

(27)   Noristi, L.; Barbè, P. C.; Baruzzi, G. Effect of the Internal/External Donor Pair in High-Yeld Catalysts for Propylene Polymerization, 1. Catalysts-Cocatalyst Interactions. *Makromol. Chem.* **1991**, *192*, 1115–1127.

(28)   Busico, V.; Cipullo, R.; Mingione, A.; Rongo, L. Accelerating the Research Approach to Ziegler–Natta Catalysts. *Ind. Eng. Chem. Res.* **2016**, *55* (10), 2686–2695.

(29)   Vittoria, A.; Meppelder, A.; Friederichs, N.; Busico, V.; Cipullo, R. Demystifying Ziegler–Natta Catalysts: The Origin of Stereoselectivity. *ACS Catal.* **2017**, *7* (7), 4509–4518.

(30)   Zaccaria, F.; Vittoria, A.; Correa, A.; Ehm, C.; Budzelaar, P. H. M.; Busico, V.; Cipullo, R. Internal Donors in Ziegler-Natta Systems: Is Reduction by AlR_3 a

Requirement for Donor Clean-Up? *ChemCatChem* **2018**, *10* (5), 984–988.

(31)   Busico, V.; Corradini, P.; De Luigi, M.; Proto, A.; Savino, V.; Albizzati, E. Polymerization of Propene in the Presence of Magnesium Chloride-Supported Ziegler-Natta Catalysts, 1. The Role of Ethyl Benzoate as "Internal" and "External" Base. *Makromol. Chemie* **1985**, *186* (6), 1279–1288.

(32)   Kuklin, M. S.; Bazhenov, A. S.; Denifl, P.; Leinonen, T.; Linnolahti, M.; Pakkanen, T. A. Stabilization of Magnesium Dichloride Surface Defects by Mono- and Bidentate Donors. *Surf. Sci.* **2015**, *635*, 5–10.

(33)   Correa, A.; Piemontesi, F.; Morini, G.; Cavallo, L. Key Elements in the Structure and Function Relationship of the MgCl$_2$/TiCl$_4$/Lewis Base Ziegler–Natta Catalytic System. *Macromolecules* **2007**, *40* (25), 9181–9189.

(34)   Shreve, A. P.; Mulhauot, R.; Fultz, W.; Calabrese, J.; Robbins, W.; Ittel, S. D. Sterically Hindered Aryloxide-Substituted Alkylaluminum Compounds. *Organometallics* **1988**, *7* (2), 409–416.

(35)   Ehm, C.; Antinucci, G.; Budzelaar, P. H. M.; Busico, V. Catalyst Activation and the Dimerization Energy of Alkylaluminium Compounds. *J. Organomet. Chem.* **2014**, *772–773*, 161–171.

(36)   Bahri-Laleh, N.; Correa, A.; Mehdipour-Ataei, S.; Arabi, H.; Haghighi, M. N.; Zohuri, G.; Cavallo, L. Moving up and down the Titanium Oxidation State in Ziegler–Natta Catalysis. *Macromolecules* **2011**, *44* (4), 778–783.

(37)   Kumawat, J.; Kumar Gupta, V.; Vanka, K. The Nature of the Active Site in Ziegler-Natta Olefin Polymerization Catalysis Systems - A Computational Investigation. *Eur. J. Inorg. Chem.* **2014**, *2014* (29), 5063–5076.

(38)   Yu, Y.; Busico, V.; Budzelaar, P. H. M.; Vittoria, A.; Cipullo, R. Of Poisons and Antidotes in Polypropylene Catalysis. *Angew. Chemie Int. Ed.* **2016**, *55* (30), 8590–8594.

(39)   Correa, A.; Credendino, R.; Pater, J. T. M.; Morini, G.; Cavallo, L. Theoretical Investigation of Active Sites at the Corners of MgCl$_2$ Crystallites in Supported Ziegler–Natta Catalysts. *Macromolecules* **2012**, *45* (9), 3695–3701.

(40)   Kissin, Y. V.; Chadwick, J. C.; Mingozzi, I.; Morini, G. Isoselectivity Distribution of Isospecific Centers in Supported Titanium-Based Ziegler-Natta Catalysts. *Macromol. Chem. Phys.* **2006**, *207* (15), 1344–1350.

(41)   Brambilla, L.; Zerbi, G.; Piemontesi, F.; Nascetti, S.; Morini, G. Structure of Donor Molecule 9,9-Bis(Methoxymethyl)-Fluorene in Ziegler-Natta Catalyst by Infrared Spectroscopy and Quantum Chemical Calculation. *J. Phys. Chem. C* **2010**, *114* (26), 11475–11484.

(42)   Morra, E.; Giamello, E.; Van Doorslaer, S.; Antinucci, G.; D'Amore, M.; Busico, V.; Chiesa, M. Probing the Coordinative Unsaturation and Local Environment of Ti^{3+} Sites in an Activated High-Yield Ziegler–Natta Catalyst. *Angew. Chemie Int. Ed.* **2015**, *54* (16), 4857–4860.

(43)   Credendino, R.; Pater, J. T. M.; Liguori, D.; Morini, G.; Cavallo, L. Investigating Alkoxysilane Coverage and Dynamics on the (104) and (110) Surfaces of MgCl$_2$-Supported Ziegler–Natta Catalysts. *J. Phys. Chem. C* **2012**, *116* (43), 22980–22986.

(44)   Credendino, R.; Liguori, D.; Morini, G.; Cavallo, L. Investigating Phthalate

and 1,3-Diether Coverage and Dynamics on the (104) and (110) Surfaces of MgCl$_2$-Supported Ziegler–Natta Catalysts. **2014**, *118* (15), 8050–8058.

(45)   Breuza, E. To Be Published. Federico II University of Naples.

(46)   Chien, J.; Wu, J. Magnesium-Chloride-Supported High-Mileage Catalysts for Olefin Polymerization. II. Reactions between Aluminum Alkyl and Promoters. *J. Polym. Sci. Part A Polym. Chem.* **1982**, *20*, 2445–2460.

(47)   Langer, A. W. B.; Burkhardt, T. J.; Steger, J. J. *Polymer Science and Technology, Vol. 19*; Price, C. C., Vandenberg, E. J., Eds.; Plenum Press: New York, 1983.

(48)   Ashby, E. C.; Laemmle, J. T. Mechanisms of Organometallic Alkylation Reactions. III. The Mechanism of Trimethylaluminum Addition to Benzophenone in Diethyl Ether. *J. Org. Chem.* **1968**, *33* (9), 3398–3401.

(49)   Csir, J. K.; Gupta, V. K.; Vanka, K. Donor Decomposition by Lewis Acids in Ziegler–Natta Catalyst Systems: A Computational Investigation. **2014**, *33*, 4357–4367.

Appendix to Chapter 3

Table A3.1. Full results of propene polymerization with system **C1+**AlEt$_3$/**EDx**.

EDx	[Ti]:[Si]:[Al]	Catalyst (mg)	Yield (mg)	R_p (Kg g^{-1} h^{-1})	M_n (KDa)	M_w (KDa)	M_w/M_n	AF (%)	$T_{el,max}$ (°C)	[*mmmrrmmm*] (%)
None	1:0:160	0.05	179	7.2	17	103	6.1	15.2	113.2	0.90
		0.05	197	7.9	18	103	5.7	11.9	113.0	0.92
ED1	1:4:160	0.05	132	5.3	22	143	6.5	10.4	112.8	1.15
		0.05	163	6.5	28	158	5.6	10.8	112.7	1.12
	1:8:160	0.05	176	7.0	24	174	7.3	8.4	112.9	1.12
		0.05	153	6.1	29	177	6.1	9.1	112.9	1.17
	1:16:160	0.05	158	6.3	29	175	6.0	6.3	112.9	1.12
		0.05	125	5.0	29	175	6.0	7.3	113.1	1.06
	1:32:160	0.05	119	4.8	25	137	5.4	7.8	112.8	1.10
		0.05	126	5.0	25	153	6.1	6.7	112.6	1.10
ED2	1:4:160	0.05	147	5.9	33	254	7.7	4.2	114.9	0.57
		0.05	161	6.4	31	247	8.0	4.0	114.7	0.62
	1:8:160	0.05	151	6.0	28	221	7.9	4.6	115.2	0.54
		0.05	151	6.0	33	250	7.6	5.4	115.4	0.56
	1:16:160	0.05	126	5.0	42	222	5.3	3.3	115.8	0.48
		0.05	137	5.5	29	229	7.8	3.5	115.9	0.49
	1:32:160	0.05	95	3.8	35	218	6.3	3.1	115.7	0.45
		0.05	85	3.4	42	257	6.1	3.3	116.0	0.44
ED3	1:4:160	0.05	152	6.1	27	171	6.3	5.0	115.0	0.66
		0.05	148	5.9	23	170	7.4	6.1	114.9	0.60
	1:8:160	0.05	132	5.3	25	173	6.9	5.2	115.3	0.53
		0.05	172	6.9	24	150	6.3	5.1	115.2	0.43
	1:16:160	0.05	130	5.2	30	180	6.0	4.8	115.5	0.49
		0.05	157	6.3	26	145	5.5	4.4	115.6	0.48
	1:32:160	0.05	117	4.7	27	176	6.6	4.3	115.7	0.45
		0.05	131	5.2	28	153	5.4	4.0	115.6	0.37
ED4	1:4:160	0.05	155	6.2	33	259	7.8	4.9	115.4	0.52
		0.05	178	7.1	30	245	8.2	4.8	115.5	0.56
	1:8:160	0.05	206	8.2	32	256	8.0	4.9	115.9	0.48
		0.05	174	7.0	31	251	8.1	4.9	115.9	0.52
	1:16:160	0.05	208	8.3	42	257	6.1	4.3	116.2	0.41
		0.05	160	6.4	32	284	8.8	3.8	116.2	0.47
	1:32:160	0.05	148	5.9	24	264	7.7	3.1	116.4	0.40
		0.05	164	6.6	39	255	6.5	3.1	116.3	0.40

EDx	[Ti]:[Si]:[Al]	Catalyst (mg)	Yield (mg)	R_p (Kg g^{-1} h^{-1})	M_n (KDa)	M_w (KDa)	M_w/M_n	AF (%)	$T_{el,max}$ (°C)	[*mmmrrmmm*] (%)
ED5	1:4:160	0.05	138	5.5	29	263	9.1	5.2	115.6	0.52
		0.05	148	5.9	25	233	9.3	4.3	115.6	0.52
	1:8:160	0.05	207	8.3	27	264	9.8	3.9	115.9	0.43
		0.05	209	8.4	29	250	8.6	3.5	116.1	0.46
	1:16:160	0.05	180	7.2	38	251	6.6	4.7	116.3	0.46
		0.05	207	8.3	41	242	5.9	3.6	116.3	0.40
	1:32:160	0.05	186	7.4	31	246	7.9	3.5	116.4	0.37
		0.05	153	6.1	30	256	8.5	3.8	116.3	0.40
ED6	1:4:160	0.05	157	6.3	26	176	6.8	4.5	115.9	0.42
		0.05	143	5.7	25	179	7.2	5.3	116.4	0.37
	1:8:160	0.05	132	5.3	34	282	8.3	5.0	116.0	0.38
		0.05	144	5.8	25	202	8.1	5.0	116.3	0.43
	1:16:160	0.05	119	4.8	25	198	7.9	5.2	116.4	0.43
		0.05	128	5.1	25	177	7.2	5.5	116.4	0.43
	1:32:160	0.05	113	4.5	22	168	7.5	4.1	116.5	0.32
		0.05	135	5.4	25	154	6.1	3.7	116.5	0.32
ED7	1:4:160	0.05	193	7.7	38	316	8.3	3.5	116.6	0.36
		0.05	170	6.8	43	361	8.4	3.0	117.0	0.38
	1:8:160	0.05	187	7.5	35	317	9.1	2.7	116.0	0.29
		0.05	185	7.4	37	314	8.5	3.8	116.3	0.32
	1:16:160	0.05	168	6.7	40	319	8.0	3.2	117.4	0.30
		0.05	178	7.1	39	313	8.0	3.6	117.5	0.29
	1:32:160	0.05	165	6.6	39	319	8.1	2.6	117.3	0.25
		0.05	145	5.8	41	340	8.3	2.7	117.7	0.24
ED8	1:4:160	0.05	194	7.8	35	383	10.9	3.9	117.2	0.36
		0.05	188	7.5	36	369	10.3	3.8	117.1	0.31
	1:8:160	0.05	220	8.8	43	400	9.3	5.3	117.6	0.31
		0.05	211	8.4	39	414	10.6	4.4	117.8	0.26
	1:16:160	0.05	218	8.7	45	393	8.8	3.0	117.9	0.26
		0.05	189	7.6	46	399	8.7	3.0	117.8	0.29
	1:32:160	0.05	208	8.3	38	365	9.5	2.4	118.0	0.20
		0.05	201	8.0	43	378	8.7	2.7	118.0	0.21

Table A3.2. Full results of propene polymerization with system **C2+**AlEt$_3$/**EDx**.

EDx	[Ti]:[Si]:[Al]	Catalyst (mg)	Yield (mg)	R_p (Kg g^{-1} h^{-1})	M_n (KDa)	M_w (KDa)	M_w/M_n	AF (%)	$T_{el,max}$ (°C)	[*mmmrrmmm*] (%)
None	1:0:160	0.04	222	11.1	27	124	4.6	3.9	114.0	0.75
		0.04	214	10.7	33	162	4.9	4.4	113.7	0.67
ED1	1:4:160	0.04	283	14.2	26	126	4.9	3.8	113.6	0.59
		0.04	240	12.0	35	151	4.3	3.9	113.6	0.65
	1:8:160	0.04	242	12.1	30	155	5.1	3.4	114.0	0.61
		0.04	194	9.7	38	164	4.3	4.0	114.0	0.68
	1:16:160	0.04	224	11.2	32	157	4.9	3.5	113.5	0.66
		0.04	176	8.8	33	173	5.3	4.1	113.6	0.65
	1:32:160	0.04	188	9.4	30	158	5.3	3.7	113.7	0.65
		0.04	199	10.0	32	167	5.2	3.8	113.6	0.57
ED2	1:4:160	0.04	201	10.1	32	151	4.7	4.0	113.9	0.67
		0.04	205	10.3	32	162	5.1	3.1	114.0	0.60
	1:8:160	0.04	170	8.5	19	139	7.2	3.7	113.9	0.59
		0.04	196	9.8	31	153	5.0	3.5	113.8	0.54
	1:16:160	0.04	156	7.8	32	169	5.3	2.8	114.3	0.56
		0.04	130	6.5	32	164	5.2	2.4	114.2	0.55
	1:32:160	0.04	133	6.7	33	173	5.2	3.9	113.8	0.58
		0.04	132	6.6	38	198	5.2	4.9	113.9	0.53
ED3	1:4:160	0.04	228	11.4	33	150	4.5	4.7	114.0	0.58
		0.04	270	13.5	34	149	4.4	3.9	114.1	0.60
	1:8:160	0.04	220	11.0	26	150	5.8	3.1	114.0	0.67
		0.04	231	11.6	32	146	4.5	3.8	113.8	0.58
	1:16:160	0.04	207	10.4	34	185	5.5	3.6	114.4	0.65
		0.04	178	8.9	32	169	5.3	3.6	114.1	0.57
	1:32:160	0.04	175	8.8	35	191	5.4	4.0	113.8	0.62
		0.04	164	8.2	35	177	5.1	4.0	113.8	0.54
ED4	1:4:160	0.04	266	13.3	33	144	4.4	4.0	113.9	0.65
		0.04	232	11.6	32	158	5.0	4.4	113.9	0.59
	1:8:160	0.04	212	10.6	35	163	4.6	3.9	113.7	0.64
		0.04	246	12.3	31	160	5.2	3.6	113.9	0.64
	1:16:160	0.075	251	10.1	35	157	4.5	3.7	114.1	0.52
		0.04	201	10.1	35	161	4.6	2.9	114.2	0.53
	1:32:160	0.04	209	10.5	33	178	5.4	3.3	113.9	0.56
		0.04	188	9.4	31	181	5.9	4.6	113.9	0.56

EDx	[Ti]:[Si]:[Al]	Catalyst (mg)	Yield (mg)	R_p (Kg g^{-1} h^{-1})	M_n (KDa)	M_w (KDa)	M_w/M_n	AF (%)	$T_{el,max}$ (°C)	[*mmmrrmmm*] (%)
ED5	1:4:160	0.04	247	12.4	39	169	4.3	3.6	114.1	0.68
		0.04	258	12.9	36	153	4.2	3.2	114.0	0.66
	1:8:160	0.04	226	11.3	35	164	4.7	3.8	114.0	0.63
		0.04	267	13.4	24	153	6.3	3.7	113.9	0.61
	1:16:160	0.04	184	9.2	35	194	5.6	3.1	114.1	0.58
		0.04	142	7.1	26	144	5.6	3.4	113.9	0.55
	1:32:160	0.04	227	11.4	35	191	5.4	4.4	113.9	0.58
		0.04	179	9.0	43	204	4.8	4.6	113.7	0.60
ED6	1:4:160	0.04	221	11.1	25	148	5.9	3.7	119.9	0.59
		0.04	198	9.9	36	143	4.0	3.5	113.8	0.59
	1:8:160	0.04	210	10.5	35	159	4.5	4.6	114.2	0.62
		0.04	213	10.7	24	151	6.3	3.9	114.1	0.57
	1:16:160	0.04	190	9.5	34	179	5.2	3.7	113.5	0.56
		0.04	192	9.6	34	205	6.0	4.1	112.8	0.47
	1:32:160	0.04	175	8.8	37	179	4.8	3.2	114.0	0.56
		0.04	146	7.3	36	185	5.2	3.1	113.8	0.57
ED7	1:4:160	0.04	202	10.1	34	155	4.5	3.7	114.1	0.64
		0.04	246	12.3	36	165	4.6	3.0	113.9	0.61
	1:8:160	0.04	185	9.3	28	149	5.4	3.3	114.1	0.62
		0.04	203	10.2	34	154	4.5	3.6	114.0	0.62
	1:16:160	0.04	211	10.6	29	166	5.8	3.6	114.0	0.55
		0.04	117	5.9	33	168	5.1	4.9	113.8	0.58
	1:32:160	0.04	196	9.8	35	185	5.3	3.0	114.0	0.56
		0.04	176	8.8	34	192	5.6	3.2	113.8	0.59
ED8	1:4:160	0.04	264	13.2	36	143	4.0	2.9	113.9	0.62
		0.04	225	11.3	36	155	4.3	3.6	114.0	0.64
	1:8:160	0.04	217	10.9	36	153	4.2	3.5	114.3	0.56
		0.04	185	9.3	37	155	4.2	4.8	114.1	0.58
	1:16:160	0.04	216	10.8	38	189	5.0	3.6	114.6	0.60
		0.04	200	10.0	33	180	5.5	3.8	114.3	0.53
	1:32:160	0.04	169	8.5	34	162	4.8	3.3	114.1	0.51
		0.04	167	8.4	39	195	5.0	4.4	114.0	0.55

Table A3.3. Full results of propene polymerization with system **C3+**AlEt$_3$/**EDx**.

EDx	[Ti]:[Si]:[Al]	Catalyst (mg)	Yield (mg)	R_p (Kg g^{-1} h^{-1})	M_n (KDa)	M_w (KDa)	M_w/M_n	AF (%)	$T_{el,max}$ (°C)	[*mmmrrmmm*] (%)
None	1:0:160	0.08	240	6.0	19	87	4.7	19.4	109.7	1.63
		0.08	234	5.9	28	105	3.7	18.2	110.0	1.53
ED1	1:4:160	0.08	269	6.7	20	85	4.2	16.6	109.7	1.39
		0.08	280	7.0	26	102	3.9	14.4	109.3	1.29
	1:8:160	0.10	355	7.2	26	111	4.5	13.5	110.2	1.25
		0.08	204	5.1	25	98	4.8	12.8	110.2	1.49
	1:16:160	0.08	189	4.7	21	104	4.9	14.8	110.5	1.33
		0.08	159	4.0	22	108	5.0	15.0	110.4	1.35
	1:32:160	0.08	190	4.8	18	83	4.7	15.3	110.4	1.38
		0.08	161	4.0	23	113	4.9	14.3	110.1	1.44
ED2	1:4:160	0.08	194	4.9	23	113	4.9	11.5	110.6	1.43
		0.08	230	5.8	26	114	4.5	11.1	110.5	1.28
	1:8:160	0.08	256	6.4	23	98	4.2	9.5	110.8	1.21
		0.08	228	5.7	24	138	5.8	9.8	112.5	1.06
	1:16:160	0.08	140	3.5	23	101	4.3	12.7	111.1	1.33
		0.08	152	3.8	21	109	5.1	10.1	111.2	1.17
	1:32:160	0.08	116	2.9	23	110	4.7	11.6	111.6	1.18
		0.08	131	3.3	29	120	4.2	11.2	111.7	1.26
ED3	1:4:160	0.08	226	5.7	22	109	4.9	11.3	110.3	1.32
		0.08	272	6.8	24	101	4.3	11.1	110.4	1.34
	1:8:160	0.08	241	6.0	23	104	4.5	11.5	110.5	1.34
		0.10	386	7.9	24	100	4.2	11.3	110.3	1.25
	1:16:160	0.08	180	4.5	22	122	5.6	12.3	110.9	1.24
		0.08	189	4.7	18	96	5.4	13.2	110.9	1.24
	1:32:160	0.08	139	3.5	24	116	4.8	10.9	111.1	1.32
		0.08	160	4.0	22	106	4.9	11.9	111.5	1.26
ED4	1:4:160	0.08	244	6.1	24	103	4.3	11.2	110.7	1.33
		0.08	238	6.0	21	104	4.9	10.4	110.3	1.33
	1:8:160	0.10	384	7.7	25	104	4.1	11.5	111.0	1.21
		0.08	255	6.4	23	98	4.3	11.0	110.8	1.38
	1:16:160	0.08	201	5.0	22	110	5.0	13.6	111.2	1.18
		0.08	199	5.0	20	99	4.9	12.9	111.0	1.22
	1:32:160	0.08	200	5.0	18	105	6.0	11.9	111.5	1.26
		0.08	167	4.2	25	126	5.0	11.9	111.7	1.31

EDx	[Ti]:[Si]:[Al]	Catalyst (mg)	Yield (mg)	R_p (Kg g^{-1} h^{-1})	M_n (KDa)	M_w (KDa)	M_w/M_n	AF (%)	$T_{el,max}$ (°C)	[*mmmrrmmm*] (%)
ED5	1:4:160	0.08	304	7.9	25	94	3.8	13.0	109.8	1.26
		0.08	248	6.2	23	109	4.8	12.1	110.2	1.39
	1:8:160	0.10	347	8.2	22	100	4.5	11.4	110.7	1.22
		0.08	228	5.7	19	84	4.4	12.9	110.1	1.36
	1:16:160	0.08	179	4.5	24	114	4.7	12.5	110.9	1.28
		0.08	197	4.9	22	105	4.7	12.4	110.9	1.39
	1:32:160	0.08	170	4.3	24	117	4.8	11.9	111.2	1.22
		0.08	167	4.2	25	117	4.7	10.7	111.3	1.35
ED6	1:4:160	0.08	176	4.4	20	89	4.4	12.8	110.9	1.19
		0.08	241	6.0	22	96	4.5	13.6	110.5	1.27
	1:8:160	0.08	216	5.4	23	106	4.7	10.2	110.9	1.32
		0.10	362	7.2	28	108	3.9	11.6	110.8	1.35
	1:16:160	0.08	163	4.1	23	110	4.7	12.7	111.1	1.29
		0.08	178	4.5	28	114	4.1	12.3	111.4	1.16
	1:32:160	0.08	147	3.7	23	109	4.7	11.9	111.3	1.32
		0.08	140	3.5	21	102	4.8	13.0	111.0	1.22
ED7	1:4:160	0.08	230	5.8	23	118	5.2	10.8	110.0	1.26
		0.08	210	5.3	22	107	4.9	10.5	111.2	1.32
	1:8:160	0.08	249	6.2	22	101	4.7	11.3	111.3	1.25
		0.08	241	6.0	25	104	4.2	11.0	111.4	1.22
	1:16:160	0.08	165	4.1	21	103	4.9	14.5	111.4	1.28
		0.08	191	4.8	25	108	4.3	13.3	111.7	1.19
	1:32:160	0.08	192	4.8	21	103	4.9	9.7	111.8	1.13
		0.08	170	4.3	26	128	4.9	10.7	112.2	1.20
ED8	1:4:160	0.08	277	6.9	26	108	4.3	11.0	111.2	1.25
		0.08	254	6.4	24	108	4.6	10.1	111.1	1.31
	1:8:160	0.10	380	7.6	25	107	4.2	12.0	111.3	1.18
		0.08	235	5.9	24	108	4.6	11.3	111.5	1.29
	1:16:160	0.08	193	4.8	23	113	5.0	12.5	110.9	1.14
		0.08	171	4.3	23	112	4.9	13.2	110.8	1.15
	1:32:160	0.08	148	3.7	19	101	5.3	11.1	112.3	1.21
		0.08	145	3.6	27	121	4.5	11.1	112.4	1.25

Table A3.4. Full results of propene polymerization with system **C4+**AlEt$_3$/**EDx**.

EDx	[Ti]:[Si]:[Al]	Catalyst (mg)	Yield (mg)	R_p (Kg g^{-1} h^{-1})	M_n (KDa)	M_w (KDa)	M_w/M_n	AF (%)	$T_{el,max}$ (°C)	[*mmmrrmmm*] (%)
None	1:0:160	0.08	158	4.0	16	103	6.5	9.9	115.0	0.70
		0.08	191	4.8	15	124	8.1	9.6	115.2	0.78
ED1	1:4:160	0.08	176	4.4	14	113	8.2	10.0	114.7	0.88
		0.08	206	5.2	15	118	8.0	9.5	114.6	0.83
	1:8:160	0.10	270	5.4	16	135	8.6	8.5	115.2	0.79
		0.10	270	5.4	17	141	8.4	7.4	115.0	0.89
	1:16:160	0.08	202	5.1	16	134	8.3	8.5	115.2	0.78
		0.08	197	4.9	17	135	7.8	9.0	115.1	0.81
	1:32:160	0.08	178	4.5	16	114	7.1	9.6	115.1	0.79
		0.08	178	4.5	17	120	7.2	8.4	115.3	0.77
ED2	1:4:160	0.08	205	5.1	17	137	8.1	7.3	115.2	0.67
		0.08	191	4.8	19	155	8.3	6.2	115.1	0.60
	1:8:160	0.10	231	4.7	18	167	9.5	5.6	115.6	0.52
		0.075	173	4.6	19	176	9.4	5.1	115.5	0.58
	1:16:160	0.08	192	4.8	18	139	7.7	5.0	115.3	0.53
		0.08	205	5.1	20	152	7.6	5.1	115.8	0.50
	1:32:160	0.08	144	3.6	20	165	8.3	5.8	115.9	0.53
		0.08	159	4.0	20	166	8.2	4.8	116.0	0.47
ED3	1:4:160	0.08	170	4.3	17	128	7.7	7.4	115.1	0.61
		0.08	217	5.4	15	131	8.7	6.9	115.1	0.64
	1:8:160	0.075	177	4.7	17	156	9.3	6.2	115.7	0.52
		0.10	289	5.8	16	138	8.4	6.2	115.4	0.51
	1:16:160	0.08	206	5.2	18	167	9.1	5.9	115.9	0.57
		0.08	226	5.7	19	143	7.7	5.6	115.8	0.53
	1:32:160	0.08	174	4.4	19	153	8.0	5.5	116.1	0.47
		0.08	190	4.8	19	140	7.4	5.3	116.1	0.45
ED4	1:4:160	0.08	239	6.0	17	142	8.5	6.5	115.5	0.60
		0.08	207	5.2	16	158	9.8	6.7	115.5	0.59
	1:8:160	0.10	315	6.7	19	178	9.2	5.1	115.7	0.54
		0.075	211	5.6	19	171	9.0	5.8	115.7	0.59
	1:16:160	0.08	252	6.3	20	182	9.3	5.6	116.1	0.54
		0.08	252	6.3	19	180	9.5	6.0	116.2	0.51
	1:32:160	0.08	245	6.1	20	171	8.4	5.3	116.4	0.40
		0.08	214	5.4	21	178	8.6	4.6	116.4	0.45

EDx	[Ti]:[Si]:[Al]	Catalyst (mg)	Yield (mg)	R_p (Kg g^{-1} h^{-1})	M_n (KDa)	M_w (KDa)	M_w/M_n	AF (%)	$T_{el,max}$ (°C)	[*mmmrrmmm*] (%)
ED5	1:4:160	0.08	238	6.0	18	157	8.7	6.9	115.6	0.59
		0.075	242	6.5	17	168	9.8	6.9	115.3	0.64
	1:8:160	0.10	325	6.5	16	187	11.4	6.1	115.6	0.61
		0.10	123	3.0	19	175	9.1	6.8	115.7	0.49
	1:16:160	0.08	234	5.9	20	175	9.0	6.0	115.9	0.52
		0.08	276	6.9	20	168	8.6	5.7	116.3	0.51
	1:32:160	0.08	245	6.1	21	187	8.9	5.5	116.1	0.47
		0.08	243	6.1	24	183	8.7	5.2	116.2	0.49
ED6	1:4:160	0.08	205	5.1	16	122	7.6	6.3	115.9	0.49
		0.08	198	5.0	14	118	8.4	6.2	115.5	0.43
	1:8:160	0.075	181	4.8	16	151	9.4	6.3	116.0	0.49
		0.10	276	5.5	18	155	8.8	5.9	115.8	0.45
	1:16:160	0.08	204	5.1	18	155	8.7	7.1	116.3	0.45
		0.08	203	5.1	18	153	8.6	6.3	116.4	0.48
	1:32:160	0.08	192	4.8	18	148	8.1	5.1	116.6	0.38
		0.08	186	4.7	17	141	8.1	4.9	116.5	0.42
ED7	1:4:160	0.08	268	6.7	18	146	8.2	5.6	116.2	0.50
		0.08	235	5.9	20	178	8.9	4.9	116.3	0.45
	1:8:160	0.10	306	6.1	18	184	10.5	4.9	116.7	0.39
		0.075	207	5.5	20	180	8.8	4.5	116.4	0.44
	1:16:160	0.08	238	6.0	22	174	8.0	5.9	116.7	0.40
		0.08	246	6.2	20	171	8.6	5.1	116.7	0.42
	1:32:160	0.08	273	6.8	21	188	9.0	4.2	116.9	0.31
		0.08	239	6.0	22	202	9.2	4.1	117.1	0.31
ED8	1:4:160	0.08	278	7.0	18	173	9.8	4.8	116.8	0.39
		0.08	273	6.8	21	186	8.7	5.3	116.4	0.49
	1:8:160	0.10	310	7.0	19	239	12.6	5.2	116.9	0.40
		0.075	232	6.2	20	233	11.6	5.4	116.7	0.39
	1:16:160	0.08	286	7.2	23	274	12.1	5.5	117.2	0.37
		0.08	245	6.1	19	250	13.2	5.1	117.2	0.39
	1:32:160	0.08	276	6.9	24	221	9.2	4.3	117.6	0.30
		0.08	246	6.2	24	239	10.0	3.9	117.4	0.34

Table A3.5. Metal and ID contents of the solid phases recovered after reacting precatalyst **C1** with AlEt$_3$ in heptane at 40°C.

| t_r (min)	$n(Mg)$[a]	$n(Al)$[a]	$n(Ti)$[a]	$n(ID)^a_{unreacted}$	$n(ID)^a_{total}$
0		0	5.29	5.25	5.25
10		8.0	3.2	2.7	4.0
20		8.1	3.3	2.8	3.9
30		8.3	3.1	2.6	4.1
40		7.9	3.0	2.4	3.8
50		8.3	2.9	2.3	4.0
60	100	8.0	3.0	2.4	3.8
70		8.3	3.0	2.2	3.7
80		8.6	3.0	2.1	3.9
90		8.9	2.8	2.0	3.5
100		9.3	2.8	2.0	3.5
110		9.0	2.9	1.6	3.2
120		8.4	2.8	1.9	3.4

[a] % mol mol(Mg)$^{-1}$

Table A3.6. Metal and ID contents of the solid phases recovered after reacting precatalyst **C1** with AlEt$_3$ in heptane at 60°C.

t_r (min)	$n(Mg)$[a]	$n(Al)$[a]	$n(Ti)$[a]	$n(ID)^a_{unreacted}$	$n(ID)^a_{total}$
0		0.0	5.3	5.25	5.25
10		7.4	3.1	2.7	4.5
20		8.3	3.4	2.5	4.0
30		7.8	3.0	2.1	3.7
40		7.7	2.7	2.0	3.7
50		7.6	2.6	1.8	3.4
60	100	8.3	2.8	1.6	3.4
70		7.6	2.5	1.5	3.3
80		8.4	2.7	1.3	3.0
90		8.1	2.5	1.1	3.0
100		7.8	2.4	1.1	2.8
110		8.3	2.5	1.0	2.8
120		9.0	2.7	0.9	2.4

[a] % mol mol(Mg)$^{-1}$

Table A3.7. Metal and ID contents of the solid phases recovered after reacting precatalyst **C1** with AlEt$_3$ in heptane at 80°C.

t_r (min)	$n(Mg)^a$	$n(Al)^a$	$n(Ti)^a$	$n(ID)^a_{unreacted}$	$n(ID)^a_{total}$
0		0	5.29	5.25	5.25
10		7.5	3.3	1.6	2.6
20		6.5	2.6	1.0	2.1
30		8.0	3.1	0.8	1.6
40		7.0	2.6	0.5	1.6
50		8.1	2.9	0.5	1.3
60	100	7.8	2.7	0.4	1.4
70		7.7	2.6	0.2	1.4
80		7.4	2.6	0.2	1.1
90		7.9	2.7	0.1	1.2
100		7.2	2.3	V. L.	0.7
110		7.1	2.5	V. L.	0.4
120		9.4	3.0	V. L.	0.3

[a] % mol mol(Mg)$^{-1}$; V.L.= very low

Table A3.8. Metal and ID contents of the solid phases recovered after reacting precatalyst **C1** with AlEt$_3$ in heptane at 100°C.

t_r (min)	$n(Mg)^a$	$n(Al)^a$	$n(Ti)^a$	$n(ID)^a_{unreacted}$	$n(ID)^a_{total}$
0		0	5.29	5.25	5.25
5		7.3	2.6	2.4	4.0
10		7.1	2.5	1.8	3.9
20		8.0	2.4	0.7	2.6
30		8.2	2.4	0.4	2.0
40		7.0	1.9	0.2	2.2
50	100	7.7	2.0	0.2	2.0
60		7.9	2.2	V.L.	1.7
70		8.6	2.3	V.L.	1.5
80		7.4	1.9	V.L.	1.4
90		7.6	2.0	V.L.	1.5
100		7.2	1.8	V.L.	1.4
120		7.5	1.9	V.L.	1.4

[a] % mol mol(Mg)$^{-1}$; V.L.= very low

4.   Regioselectivity of ZN catalysts for PP

4.1. Introduction

## 4.2. ^{13}C NMR assignment of regioirregular units in ZN PP
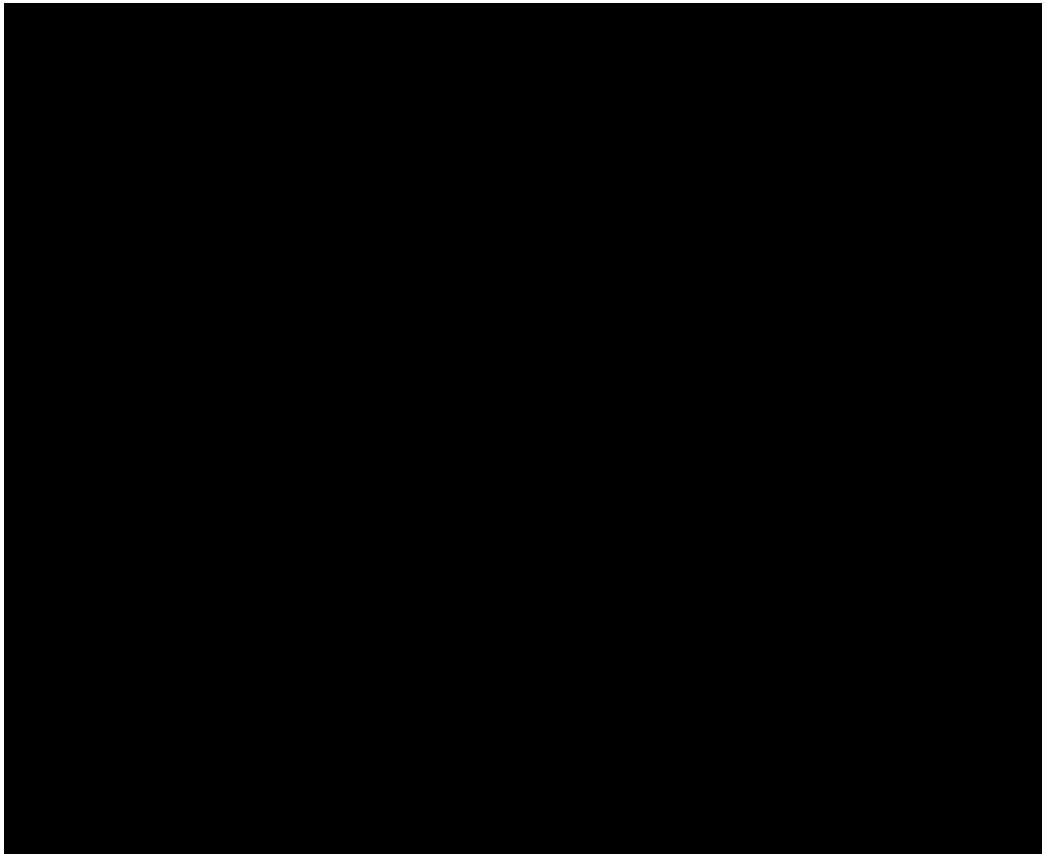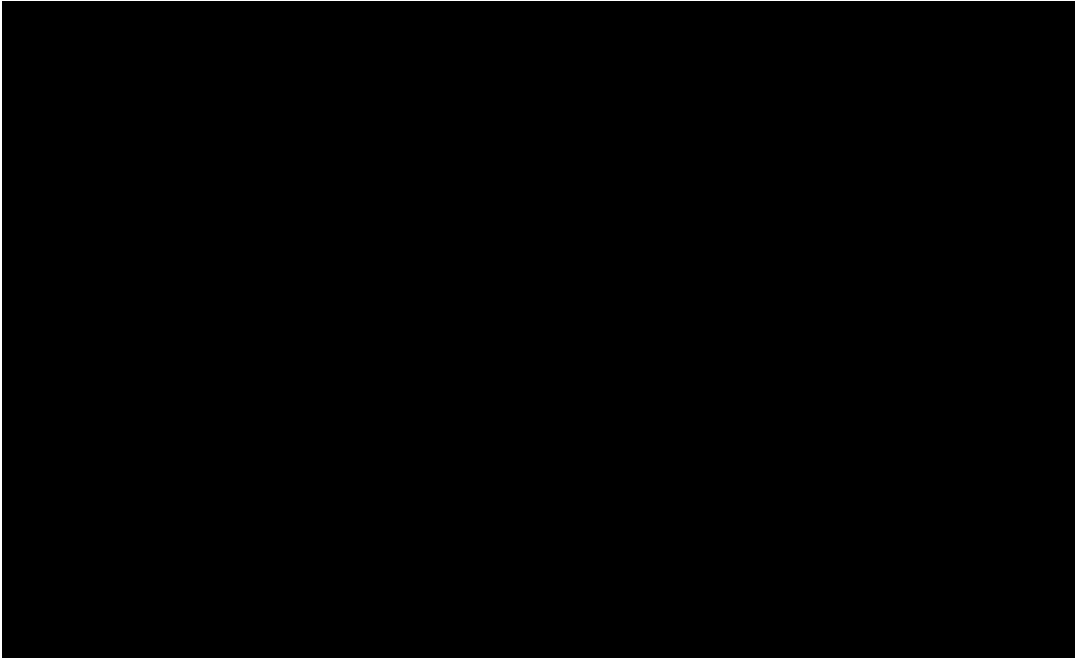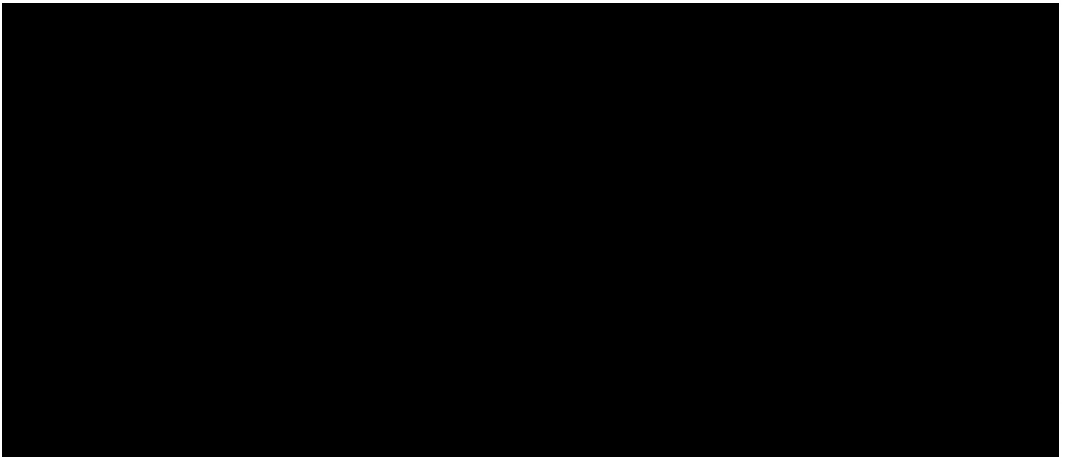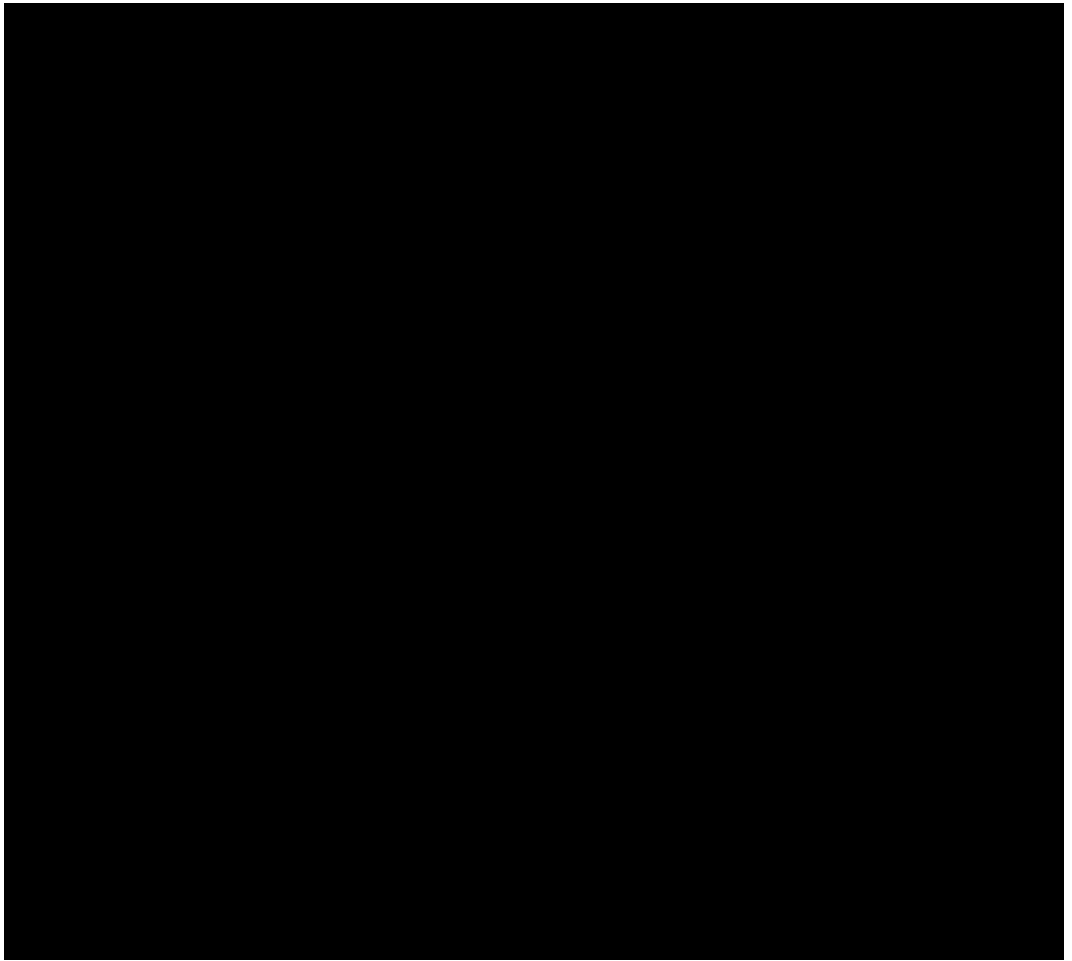
4.3. A HTE protocol for measuring the regioselectivity of ZN PP catalyst systems

██
██████████

████████████████	████████	████████	████████	████████	████
████████████████	████████	████████	████████	████████	████
████████████████████	████████	████████	████████	████████	████
██			████████████		
██					
██					
█████████████████████████████					
██					
██					
█████████████████████████████					
██					

██

████████████████████████

███████████████████	████████	████████████	██████████
███████████	██████████████	██████████	
██████████████	██████████	██████████	
█████████████	██████████	██████████	

██
██
██
██
██
██
██
██
██
██

█████████████

4.4. A HTE screening of the regioselectivity of ZN PP catalyst systems

██
██
██
██
██
██
███████████████████████████████████████

██
████████████

███ ██	██	██
████████████████████████████████		
███		
███		
███		
███		
███		
███		
███		
███		
███		

References

(1)   Vittoria, A.; Meppelder, A.; Friederichs, N.; Busico, V.; Cipullo, R. Demystifying Ziegler-Natta Catalysts: The Origin of Stereoselectivity. *ACS Catal.* **2017**, *7* (7), 4509–4518.

(2)   Cecchin, G.; Morini, G.; Piemontesi, F. Ziegler-Natta Catalysts. In *Kirk-Othmer Encyclopedia of Chemical Technology*; Seidel, A., Ed.; John Wiley & Sons, Inc.: Hoboken, NJ, 2007; pp 502–554.

(3)   Pasquini, N. *Polypropylene Handbook, 2nd Ed.*; Hanser Publisher: Munich, 2005.

(4)   Pellecchia, C.; Zambelli, A.; Oliva, L.; Pappalardo, D. Syndiotactic-Specific Polymerization of Propene with Nickel-Based Catalysts. 2. Regiochemistry and Stereochemistry of the Initiation Steps. *Macromolecules* **1996**, *29* (22), 6990–6993.

(5)   Zambelli, A.; Ammendola, P. Stereospecific Polymerization of α-Olefins: End Groups, Polymer Structure and Reaction Mechanism. *Polym. Sci.* **1991**, *16*, 203–218.

(6)   Zambelli, A.; Sacchi, M. C.; Locatelli, P.; Zannoni, G. Isotactic Polymerization of α-Olefins: Stereoregulation for Different Reactive Chain Ends. *Macromolecules* **1982**, *15* (1), 211–212.

(7)   Zambelli, A.; Locatelli, P.; Sacchi, M. C.; Tritto, I. Isotactic Polymerization of Propene: Stereoregularity of the Insertion of the First Monomer Unit as a Fingerprint of the Catalytic Active Site. *Macromolecules* **1982**, *15* (3), 831–834.

(8)   Busico, V.; Cipullo, R.; Corradini, P. Ziegler-Natta Oligomerization of 1-Alkenes: A Catalyst's "Fingerprint", 2 Preliminary Results of Propene Hydrooligomerization in the Presence of the Homogeneous Isospecific Catalyst System *rac*-(EBI) ZrCI$_2$/MAO. *Makromol. Chem., Rapid Commun.* **1993**, *103*, 97–103.

(9)   Busico, V.; Cipullo, R.; Corradini, P. Ziegler-Natta Oligomerization of 1-Alkenes: A Catalyst's "Fingerprint", 1 Hydrooligomerization of Propene in the Presence of a Highly Isospecific MgCl$_2$-Supported Catalyst. *Makromol. Chem.* **1993**, *194*, 1079–1093.

(10)   Busico, V.; Cipullo, R.; Polzone, C.; Talarico, G.; Chadwick, J. C. Propene/Ethene-[1-^{13}C] Copolymerization as a Tool for Investigating Catalyst Regioselectivity. 2. The MgCl$_2$/TiCl$_4$–AlR$_3$ System. *Macromolecules* **2003**, *36* (8), 2616–2622.

(11)   Busico, V.; Cipullo, R.; Ronca, S. Propene/Ethene-[1-^{13}C] Copolymerization as a Tool for Investigating Catalyst Regioselectivity. 1. Theory and Calibration. *Macromolecules* **2002**, *35* (5), 1537–1542.

(12)   Busico, V.; Cipullo, R. Microstructure of Polypropylene. *Prog. Polym. Sci.* **2001**, *26* (3), 443–533.

(13)   Corradini, P.; Barone, V.; Fusco, R.; Guerra, G. Analysis of Models for the Ziegler-Natta Stereospecific Polymerization on the Basis of Non-Bonded Interactions at the Catalytic Site—I. The Cossee Model. *Eur. Polym. J.* **1979**, *15* (12), 1133–1141.

(14)   Corradini, P.; Barone, V.; Fusco, R.; Guerra, G. A Possible Model of Catalytic Sites for the Stereospecific Polymerization of Alpha-Olefins on 1st-Generation and Supported Ziegler-Natta Catalysts. *Gazz. Chim. Ital.* **1983**, *113*, 601–607.

(15)   Corradini, P.; Busico, V.; Cavallo, L.; Guerra, G.; Vacatello, M.; Venditto, V. Structural Analogies between Homogeneous and Heterogeneous Catalysts for the Stereospecific Polymerization of 1-Alkenes. *J. Mol. Catal.* **1992**, *74* (1), 433–442.

(16)   Zhou, Z.; Kümmerle, R.; Stevens, J. C.; Redwine, D.; He, Y.; Qiu, X.; Cong, R.; Klosin, J.; Montañez, N.; Roof, G. 13C NMR of Polyolefins with a New High Temperature 10mm Cryoprobe. *J. Magn. Reson.* **2009**, *200* (2), 328–333.

(17)   Zhou, Z.; Stevens, J. C.; Klosin, J.; KUmmerle, R.; Qiu, X.; Redwine, D.; Cong, R.; Taha, A.; Mason, J.; Winniford, B.; et al. NMR Study of Isolated 2,1-Inverse Insertion in Isotactic Polypropylene. *Macromolecules* **2009**, *42* (6), 2291–2294.

(18)   Busico, V.; Cipullo, R. Microstructure of Polypropylene. *Prog. Polym. Sci.* **2001**, *26* (3), 443–533.

(19)   Busico, V.; Cipullo, R.; Chadwick, J. C.; Modder, J. F.; Sudmeijer, O. Effects of Regiochemical and Stereochemical Errors on the Course of Isotactic Propene Polyinsertion Promoted by Homogeneous Ziegler-Natta Catalysts. *Macromolecules* **1994**, *27* (26), 7538–7543.

(20)   Brintzinger, H. H.; Fischer, D.; Mülhaupt, R.; Rieger, B.; Waymouth, R. M. Stereospecific Olefin Polymerization with Chiral Metallocene Catalysts. *Angew. Chemie Int. Ed. English* **1995**, *34* (11), 1143–1170.

(21)   Resconi, L.; Cavallo, L.; Fait, A.; Piemontesi, F. Selectivity in Propene Polymerization with Metallocene Catalysts. *Chem. Rev.* **2000**, *100* (4), 1253–1346.

(22)   Boussie, T. R.; Diamond, G. M.; Goh, C.; Hall, K. A.; LaPointe, A. M.; Leclerc, M. K.; Murphy, V.; Shoemaker, J. A. W.; Turner, H.; Rosen, R. K.; et al. Nonconventional Catalysts for Isotactic Propene Polymerization in Solution Developed by Using High-Throughput-Screening Technologies. *Angew. Chemie Int. Ed.* **2006**, *45* (20), 3278–3283.

(23)   Fujita, M.; Coates, G. W. Synthesis and Characterization of Alternating and Multiblock Copolymers from Ethylene and Cyclopentene. *Macromolecules* **2002**, *35* (26), 9640–9647.

(24)   Cipullo, R.; Vittoria, A.; Busico, V. Assignment of Regioirregular Sequences in the 13C NMR Spectrum of Syndiotactic Polypropylene. *Polymers (Basel).* **2018**, *10* (8), 863.

(25)   Ewen, J. A.; Jones, R. L.; Razavi, A.; Ferrara, J. D. Syndiospecific Propylene Polymerizations with Group 4 Metallocenes. *J. Am. Chem. Soc.* **1988**, *110* (18), 6255–6256.

5. QSAR of Metallocene PP catalysts

5.1.   Introduction

In the previous two chapters we have presented applications of our HTE workflow to heterogeneous ZN PP catalysts. Here and in the next one we broaden the scope of the HTE approach to molecular catalysts, starting with the screening and optimization of C_2-symmetric bis(indenyl) *ansa*-zirconocenes for isotactic-selective propene homo-polymerization.

The ability of Group 4 metallocene compounds (e.g. Cp_2TiCl_2; Cp = h^5-cyclo-pentadienyl) to mediate olefin polymerization was known since the late 1950s.[1,2] Initially used in combination with AlR_xCl_{3-x} activators, in analogy with classical ZN systems, they featured poor activity towards ethene and propene, and no stereoselectivity for the latter monomer. As matter of fact, for over two decades they were only used as molecular mimics of ZN catalysts in mechanistic studies.[1,2] The scenario changed dramatically in 1976, when in the group of Prof. Kaminsky at the University of Hamburg the strongly activating effect of traces of water on $Cp_2MX_2/AlMe_3$ (X = halogen, alkyl or aryl) catalyst systems in ethene polymerization was serendipitously discovered.[3–5] The reason turned out to be that the stoichiometric hydrolysis of $AlMe_3$ (TMA) under mild conditions forms methylalumoxane (MAO), a complex mixture of oligomers mostly with cage structures in which the $–(Al(Me)O)_n–$ fragment can be proposed as the 'monomer'. The key point for olefin polymerization catalysis is that the activation of Cp_2MX_2

precursors by MAO ends up with $[Cp_2MMe][(MAO)X_2]$ ion pairs, in which the poorly coordinating $[(MAO)X_2]^-$ anion with delocalized charge does not hamper monomer π-coordination to the M center in the $[Cp_2MMe]^+$ cation, at odds with $[Cp_2XMe][AlMe_2X_2]$ ion pairs where the anion in nonpolar media acts as an effective monomer stopper.[6]

Whereas several simple metallocene catalysts with non-chirotopic active sites turned out to be of practical interest for ethene homopolymerization and ethene/1-alkene copolymerizations, application to propene polymerization required an extensive elaboration of the ancillary ligand framework, primarily aimed to introduce the active site chirotopicity which is a pre-requisite for a high enantioselectivity in the insertion of the prochiral monomer. A tremendous research effort in industry and academia over some 15 years led to the discovery of a myriad of metallocene structures with different symmetries and stereoselectivities. The popular 'PP metallocene catalyst tree' (Figure 5.1) published by Resconi in a leading *Chem. Rev.* article[6] includes many competent C_2-symmetric and C_1-symmetric catalysts yielding isotactic (i-) PP,[7] and several C_s-symmetric catalysts producing syndiotactic (s-) PP.[8] Unfortunately, this beautiful scientific adventure had very limited industrial success, because highly stereoregular s-PP can only be obtained under impractical process conditions, whereas i-PP made with ZN catalysts has higher margins and, with only few exceptions, better application performance than metallocene i-PP.[9]

The two leads among metallocene catalysts for i-PP were *rac*-Me$_2$Si(2-Me-4-Ph-Ind)$_2$ZrCl$_2$[10], developed by Spaleck et al. at Hoechst, and *rac*-Me$_2$Si((2-Me-(4,5-benz-[e]-indenyl))$_2$ZrCl$_2$[11], designed by Brintzinger in collaboration with BASF. The key structural element in common is a stereorigid C_2-symmetric Me$_2$Si-bridged *ansa*-bis(1-indenyl) ligand framework, which can be suitably substituted so as to enforce the chiral recognition of propene enantiofaces at the two homotopic coordination sites of the Zr centers. Both catalysts can be immobilized on a support (like e.g. silica/MAO), and produce i-PP with relatively high stereoregularity and decent average MW at practical polymerization temperatures (e.g. 70°C). A number of subsequent elaborations of Spaleck's complex (from now on, **M1**), by Spaleck himself and also by others, led to significant improvements in performance. Rieger recently disclosed an 'ultrarigid' Hf-based homologue of **M1** able to produce 'perfect' i-PP at 0°C[12,13]: the polymer would feature no detectable stereo- and regiodefects when analyzed by ^{13}C NMR,

and M_w > 5 MDa. At practical temperatures, though, in all cases the performance greatly deteriorates.
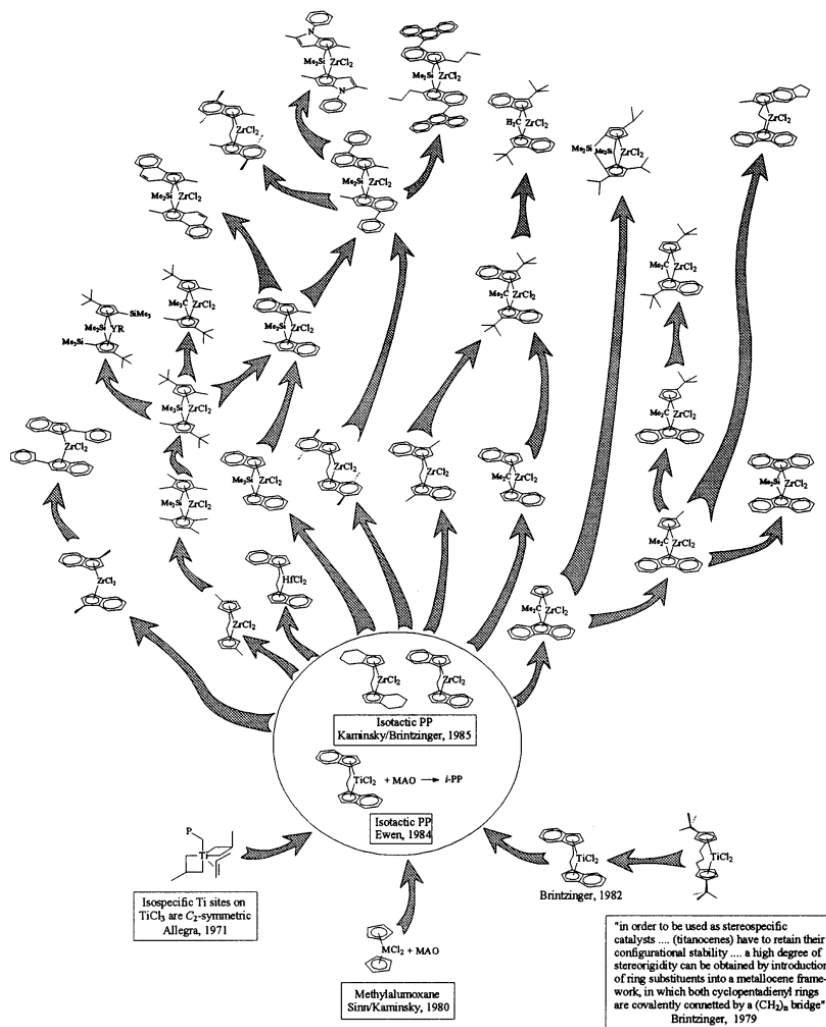

Figure 5.1 The evolution of metallocene catalysts for propene polymerization.[6]

In the last decade, a sentiment that 'all has been said' concerning C_2-symmetric *ansa*-metallocene catalysts for i-PP has spread in the scientific community.[14] On the other hand, the potential of HTE in this story had no time to be exploited, for a number of good reasons. In the first place, parallel methods for metallocene synthesis have been lacking until very recently, which represented a heavy

limitation in primary and secondary screening campaigns. High-throughput polymer characterization methods able to analyze and rank samples with tiny amounts of regio- and stereodefects have also become available only recently (see Chapters 2-4). Last but not least, QM computational modeling still lacks the accuracy that would be necessary to anticipate catalyst performance thus aiding rational ligand design.

Moving from these considerations, the Dutch Polymer Institute (DPI) has recently started a collaborative research project involving three world-leading research groups, namely that of Prof. Alexander Voskoboynikov at Moscow State University (MSU) for (parallel) metallocene synthesis; LSP (Profs. Vincenzo Busico and Roberta Cipullo) at the Federico II University for HTE studies of propene polymerization and PP microstructural characterization; and the group of Prof. Alceo Macchioni at the University of Perugia for solution NMR studies of catalyst ion pairs. The main aim of the project, which is currently ongoing, is the HTE determination of the QSAR for metallocene olefin polymerization catalysts. The present PhD project has contributed to the part of the endeavor dealing with a refinement of Spaleck-type *ansa*-metallocenes. The results obtained thus far, which have already been published[15], will be presented and discussed in the following sections.

5.2. Results and discussion

5.2.1. Catalysts selection

The catalysts screened in this study, reported in Figure 5.2, correspond to a first set with a wide variety of substituents in the 4-position of the indenyl groups, bearing promise for important electronic and steric effects.
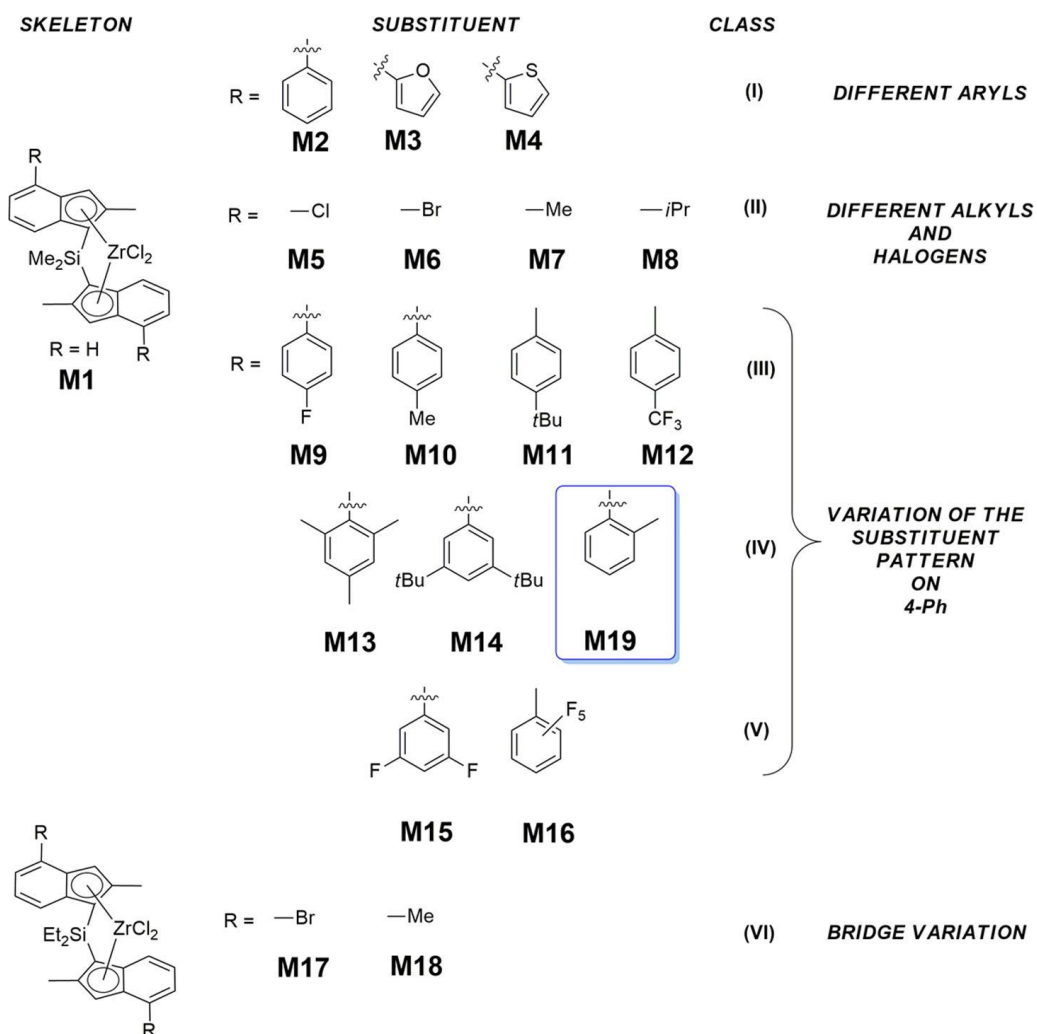
Figure 5.2. Pre-catalysts screened in propene homopolymerization. Catalyst **M19** was synthesized and tested *a posteriori* as a proof of concept.

All catalyst, including the parent **M1**, are 2-Me substituted to increase PP MW.[16] The substituents include:

(I)   Different aryl and hetaryl groups, i.e. phenyl (**M2**), 2-furyl (**M3**) and 2-thienyl (**M4**): here, electron-rich aryl fragments could manifest electronic influences.

(II)   Different halogens, i.e. Cl (**M5**) vs. Br (**M6**), or alkyl, i.e. Me (**M7**) vs. *i*Pr (**M8**), allowing modulation of steric and electronic influence.

(III)   4-Ph systems substituted in *para*-position by electron donating [Me (**M10**) and *t*Bu (**M11**)] or electron withdrawing groups [F (**M9**) or CF_3 (**M12**)] allow for clear identification of electronic trends. Direct steric influences can be excluded due to the remoteness of this position.

(IV)   Systems with additional steric crowding close to active pocket, i.e. mesityl (**M13**) or 3,5-di-*t*Bu-Ph (**M14**).

(V)   4-Ph systems with fluorine atoms close to the active pocket, i.e. substitution in *meta*-position (**M15**) or *ortho*-position (**M16**, C_6F_5) allowing insight into steric, electronic and potentially H-F contact effects.

(VI)   To test the influence of substituents on the silicon bridge, **M17** and **M18** feature a $SiEt_2$ bridge, while all other systems possess a $SiMe_2$ bridge.

Some of the catalysts are known and were previously tested in propene homopolymerization, albeit in varying detail. The performance of **M1**, **M2** and **M8** in propene homopolymerization has been reported in the literature.[10,17] **M11** and **M14** have been described by the groups of Linnolathi and Resconi, but in heterogenous systems.[18] **M6**, **M7**, **M9**, **M10**, **M13**, **M15**, **M17**, **M18**, and **M19** have been claimed in the patent literature only and in little detail.[19–21] The synthesis of **M4** has been described but no polymerization performance data is available.[22] To our knowledge, **M3**, **M5**, **M12** and **M16** precursors had not been synthesized so far.

5.2.2. Propene homopolymerization results

All polymerizations were conducted under a standard set of conditions. A polymerization temperature of 60°C was chosen in order to avoid an observable contribution coming from growing chain epimerization. As demonstrated for the parent catalyst **M1**, this temperature is a 'safe spot' provided that the monomer

concentration is high enough (≥ 2.2 mol/L).[23,24] Preliminary studies in our laboratory indicated that Spaleck's catalyst **M2** also shows no chain epimerization, even at lower propene concentrations. Anyhow, two propene partial pressures, i.e. 65 psi (4.5 bar) and 95 psi (6.5 bar) were tested to verify that this is the case for all catalysts of this work. Stereoregularity of the polymers produced at said two pressures were found identical within the experimental error, implying that chain epimerization does not affect stereoselectivity appreciably.

Triisobutylaluminum/HNMe$_2$Ph$^+$[B(C$_6$F$_5$)$_4$]$^-$ (TIBA/AB) was chosen as the scavenger/alkylator/activator system, as the one guaranteeing the best control of polymerization kinetics. All catalysts, except **M18**, were also tested using triisobutylaluminum/trityl tetrakis(pentafluorophenyl)borate ([Ph$_3$C][B(C$_6$F$_5$)$_4$], TIBA/TTB) at 95 psi propene partial pressure.

The main results of the screening are summarized in Table 5.1 and Figure 5.2. All data are averages of at least duplicate experiments. Catalyst **M19** is included in Figure 5.2 and Table 5.1, but since it was synthesized *a posteriori* (after complete analysis of the 18 validation catalysts), its polymer characteristics will be discussed in a further section, after rationalizing what drives catalyst performance in these systems.

Figure 5.3 shows a bar graph representation of stereoselectivity, regioselectivity, and MW capability for each catalyst, along with the DSC melting points of all polymers (dots). To compare all 'error' sources (stereoerrors, regioerrors and chain ends) on the same scale, these are plotted as Gibbs free energy differences ($\Delta\Delta G^{\#}$) between the relevant events (*re vs si* insertion, 1,2 *vs* 2,1 insertion, propagation *vs* termination (T/P), respectively). This is licit whenever Curtin-Hammet principle[25] applies: in this case, propene coordination is reversible and the olefin complex lies energetically below the transition states (TSs) of interest. In such a regime, the relative ratios of kinetic constants are solely determined by TS energy differences.[26]

In the following, we discuss separately the observed trends in stereoselectivity, regioselectivity, and molecular weight capability.

Stereoselectivity. All activated precatalysts substituted in 4-position show high isotactic selectivity, regardless of the substituent, with enantioselectivity (σ) values between 0.9917 and 0.9997 at 60°C, which translate into a $\Delta\Delta G^{\#}_{enantio}$ difference of 3.2 to 5.4 kcal/mol. The unsubstituted catalyst **M1** shows a lower

stereoselectivity (σ = 0.9865; $\Delta\Delta G^{\#}_{enantio}$ =2.8 kcal/mol).[17] ^{13}C-NMR spectra expanded in the methyl region of the PP samples obtained with catalysts **M1**, **M2**, **M13** and **M14** are shown in Figure 5.4.

Table 5.1. Summary of propene polymerization results with catalysts **M1-M19** activated with TIBA/AB ([AB]/[Zr] = 2.0) in toluene at 60°C and 95 psi propene partial pressure. Experimental uncertainty on last significant digit is ±1, unless otherwise indicated in parentheses.

Catalyst	[*mmrrmm*][A]	σ	$\Delta\Delta G^{\#}_{enantio}$[B]	[2,1][C]	[3,1][D]	$\Delta\Delta G^{\#}_{regio}$[B]	M_n[E]	M_w[E]	PDI	$\Delta\Delta G^{\#}_{T/P}$[D]	T_m[F]
M1	1.25(3)	0.9865(3)	2.8	0.25	0.03	3.9	98	189	1.9	5.2	145.7
M2	0.12	0.9988	4.5	0.32	n.d.	3.8	319	621	2.0	5.9	160.1
M3	0.79	0.9917	3.2	0.90	n.d	3.1	126	265	2.1	5.3	143.2
M4	0.29(2)	0.9971(3)	3.9	0.50(2)	n.d.	3.5	232	474	2.0	5.7	153.2
M5	0.39(3)	0.9960(3)	3.7	0.54(3)	n.d.	3.5	145	288	2.0	5.4	151.7
M6	0.39	0.9960	3.7	0.82	n.d.	3.2	136	269	1.9	5.4	148.9
M7	0.39(2)	0.9960(2)	3.6	0.62(2)	0.04	3.3	78	162	2.1	5.0	148.9
M8	0.37(2)	0.9962(2)	3.7	0.69	0.05	3.3	100	208	2.1	5.2	149.7
M9	0.11	0.9989	4.5	0.29	n.d.	3.9	316	651	2.1	5.9	157.3
M10	0.14	0.9986	4.4	0.38	0.04(4)	3.7	232	551	2.4	5.7	157.6
M11	0.14	0.9986	4.4	0.29	0.02(2)	3.9	254	550	2.2	5.8	159.3
M12	0.11	0.9989	4.5	0.32	n.d.	3.8	293	701	2.4	5.9	156.9
M13	0.03	0.9997	5.4	0.21(2)	0.18(3)	3.7	76	169	2.2	5.0	155.3
M14	0.06	0.9994	4.8	0.17	n.d.	4.2	533	1139	2.2	6.3	162.4
M15	0.16	0.9984	4.2	0.42	n.d	3.6	290	678	2.3	5.9	157.2
M16	0.06	0.9994	4.9	0.18	n.d.	4.2	408	885	2.2	6.1	160.8
M17	0.36	0.9963	3.7	0.78(3)	n.d.	3.2	143	281	2.0	5.4	149.0
M18	0.39(3)	0.9959(2)	3.7	0.61(2)	0.05(5)	3.3	91	186	2.1	5.1	149.3
M19	0.01	0.9999	6.1	0.32	0.09	3.6	470	1049	2.2	6.2	158.2

[A] % of total ^{13}C NMR methyl integral. [B] In kcal/mol. [C] Fraction of 2,1 units, in mol%. [D] Fraction of 3,1 units, in mol%. [E] In kDa. [F] In °C.
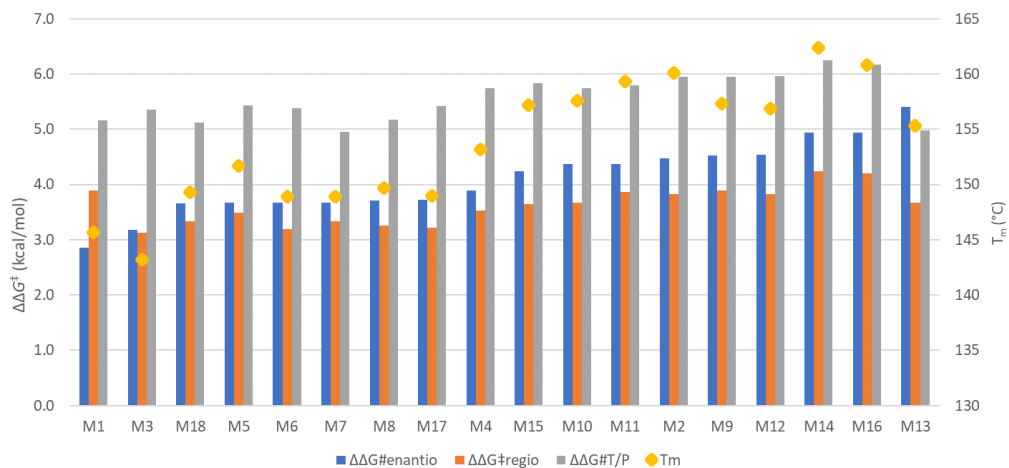
Figure 5.3. Bar graphs for stereoselectivity (as $\Delta\Delta G^{\#}_{enantio}$), regioselectivity (as $\Delta\Delta G^{\#}_{regio}$), and molecular weight capability (as $\Delta\Delta G^{\#}_{T/P}$) for the screened catalysts (Figure 5.2). Polymer melting points (T_m) provided as single yellow dots. Data taken from Table 5.1.
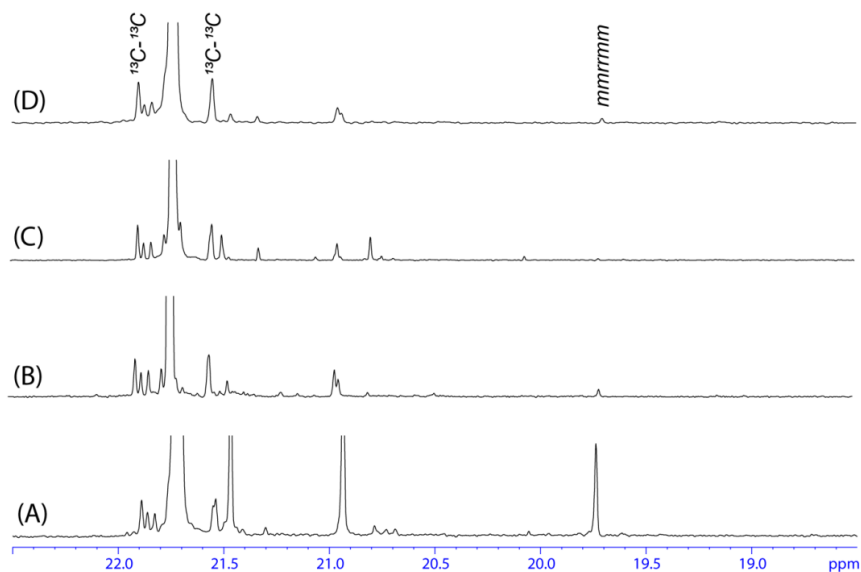

Figure 5.4. ^{13}C NMR spectra (expanded in the methyl region) of the PP samples obtained with catalysts **M1** (A), **M2** (B), **M13** (C) and **M14** (D).

The simple substitution of the hydrogen in 4-position of **M1** with alkyl or halogen substituents increases σ substantially. The σ value remains essentially constant ($\sigma \approx 0.996$) even though the substituent size increases in the order Cl (**M5**) < Br (**M6**) < Me (**M7**) < iPr (**M8**).[27] Aromatic substituents show a wide diversity. The furyl substituted catalyst **M3** shows the "poorest" stereoselectivity in the whole catalysts set ($\sigma = 0.9917$) excluding **M1**. **M4** (thienyl) shows a slightly increased stereoselectivity ($\sigma = 0.9971$) over alkyl and halogen substituents, while σ reaches 0.9988 ($\Delta\Delta G^{\#}_{enantio}$ = 4.5 kal/mol) in the phenyl substituted system **M2**. The increase in stereoselectivity for aryl substituted systems follows the size of the aromatic system, i.e. furyl < thienyl < phenyl. Change of the bridge from Me_2Si to Et_2Si has no influence on the stereoselectivity, as confirmed by the pairs **M6** *vs* **M17** and **M7** *vs* **M18**.

Variation of the substituents on Ph (**M2**) has different effects. *Para*-substitution on Ph has negligible effects on the stereoselectivity ($\Delta\Delta G^{\#}_{enantio}$ = ±0.1 kcal/mol, compared to **M2**). Steric bulk, i.e. H (**M2**) < F (**M9**) < Me (**M10**) < CF_3 (**M12**) < tBu (**M11**) as well as electronic effects are therefore irrelevant.

Conversely, variation of the *meta* substituents on Ph (**M2**) does affect the stereoselectivity: for **M15** (*meta*-F) $\sigma = 0.9984$, i.e. $\Delta\Delta G^{\#}_{enantio}$ = 4.2 kcal/mol, while for **M14** (*meta*-tBu) σ =0.9994, i.e. $\Delta\Delta G^{\#}_{enantio}$ = 4.8 kcal/mol. It appears that this trend does not follow the substituent size (H < F << tBu). Introduction of a substituent in *ortho*-position on Ph (**M2**), which points directly into the active pocket, also increases stereoselectivity. **M16** (C_6F_5) reaches $\sigma = 0.9994$ while stereoselectivity for **M13** (2,4,6-Me_3) is $\sigma = 0.9997$ ($\Delta\Delta G^{\#}_{enantio}$ = 5.4 kcal/mol). This trend appears to follow the size of the substituent (H < F < Me).

M13, **M14** and **M16** reach the performance of the best known zirconocenes. For instance, the group of Linnolahti has recently reported that *rac*-Me_2Si(2-Me-4-Ph-5-OMe-6-tBu-Ind)$_2ZrCl_2$ yields i-PP with [*mmmm*] = 0.9975 (70°C), corresponding to $\sigma = 0.9995$, albeit with a low regioregularity ([2,1] = 1.6%).[28] The high performance of Rieger's ultra-rigid metallocenes has been in part explained by a repulsive interaction of the methoxy substituent in 7-position of the indenyl with the $SiMe_2$ bridge, which lowers the bite angle of the metallocene.[13] The ligand framework of **M14** is identical to Rieger's framework but omits the methoxy group. Although some caution should be used when comparing the performance of catalysts under non-identical conditions, as mentioned in the introduction, **M14** shows increased stereoselectivity compared to Rieger's catalyst ($\sigma = 0.9995$ *vs* $\sigma \approx 0.9983$ at 60°C, both for the Zr and Hf derivative[13]), implying that the

additional   7-MeO substitution might, in fact, be counterproductive with respect to stereoselectivity.

Regioselectivity. The i-PP samples produced with **M1**-**M18** show from 0.17 to 0.90 mol% regioerrors. This translates to a span of $\Delta\Delta G^{\ddagger}_{regio}$ of $\approx$0.9 kcal/mol for the set of 18 catalysts, i.e. much narrower than that observed for stereoselectivity ($\approx$2.6 kcal/mol). Trends follow qualitatively those observed for stereoselectivity. Substituents that only lead to a modest increase of stereoselectivity like alkyl (**M8**, **M7** and **M18**), halogen (**M5**, **M6** and **M17**) and furyl/thienyl result into the highest amounts of regiodefects (0.5 – 0.9%), while all phenyl-substituted systems produce i-PP with lower amounts of regiodefects (0.17 – 0.42%). The unsubstituted **M1** yields a polymer with only 0.29% regiodefects. Only catalysts with very high stereoselectivity (**M14** and **M16**) exceed this performance. **M13** is an exception here, its polymer containing 0.40% regiodefects despite having a high stereoselectivity.

No correlation with electronic properties of the substituent in 4-position can be observed, as electron-withdrawing substituents like Br (**M6**, 0.82%) and Cl (**M5**, 0.53%) result into i-PP samples with less or more regioerrors than electron donating substituents like Me (**M7**, 0.67%) and iPr (**M8,** 0.74%). Moreover, the electron-rich arene-substituted systems **M3** (0.90%) and **M4** (0.50%) can be found towards the low as well as the high end of this series. Substitution on Ph does not yield clear electronic trends either.

Regioselectivity appears to decrease if steric bulk of the substituents decreases, looking at the pairs **M5/M6** (Br > Cl) and **M7/M8** (iPr > Me), but the trend for **M3**, **M4**, **M2, M16** (furyl < thienyl < Ph < C_6F_5) indicates the opposite. Change of the bridge from Me_2Si to Et_2Si does not affect regioselectivity (**M6** vs. **M17** and **M7** vs. **M18**).

MW capability. Also here we observe that trends in MW (M_n *and* M_w, as PDI is in all cases $\approx$2.0) follow qualitatively those in stereoselectivity, i.e. the higher the stereoselectivity, the higher the molecular weight. **M13** (mesityl substituent) behaves as an outlier and produces a short polymer (M_w = 169 kDa), despite having a very high stereoselectivity. The Me (**M7**, **M18**), iPr (**M8**) substituted systems and the unsubstituted **M1** produce i-PP with the lowest M_w values (160 to 210 kDa). The Cl (**M5**) and Br (**M6**, **M17**) substituted systems yields polymers with somewhat increased M_w (270 – 290 kDa). **M3** (furyl), the smallest aryl

substituted system, shows a similar performance (265 kDa). All other aryl systems show decent to very good (474 – 1139 kDa) M_w capabilities at 60°C. Electron donating substituents (Me, *t*Bu) in *para*-Ph position (**M10**, **M11**) appear to decrease M_w somewhat ($\approx$ 550 kDa *vs* 621 for **M2**), while electron withdrawing substituents on Ph (F, CF$_3$ but also C$_6$F$_5$) increase M_w (**M2 < M9 < M15 < M12 << M16**, 621 – 885 kDa). **M14**, which brings bulky *t*Bu groups from the outside near the active pocket, yields i-PP with the highest M_w value (= 1139 kDa).

Activity. Although the project focused primarily on polymer microstructure, we cannot ignore the substituent effects on the catalytic activity of zirconocenes **M1-M19**. As already noted TIBA/AB was mainly used as the scavenger/alkylator/ activator system for a good control of the polymerization kinetics; observed activities indeed are relatively low, likely due to the formation of N,N-dimethylaniline which can compete with the monomer for coordination to Zr. On the other hand, activators like MAO or TIBA/TTB ended up with (much) higher catalyst activities (Table 5.2), in some cases very difficult to control; as a matter of fact, the values in the table should be regarded with some caution and likely only correspond to a lower limit, as we did not attempt to optimize performance yet. On the other hand, the polymers produced by a given catalyst in combination with different activators turned out to be practically identical.

Table 5.2. Average productivities in propene polymerization in toluene solution at 60°C (R_p, in kg mmol^{-1} h^{-1}) for the screened catalysts for the two used activator systems.

Catalyst	R_p (TIBA/AB)	R_p (TIBA/TTB)	Catalyst	R_p (TIBA/AB)	R_p (TIBA/TTB)
M1	26	512	**M10**	12	804
M2	14	1286	**M11**	17	851
M3	14	41	**M12**	0.3	97
M4	22	219	**M13**	2	32
M5	4	120	**M14**	3	276
M6	2	721	**M15**	2	552
M7	18	103	**M16**	1	136
M8	40	312	**M17**	1	394
M9	8	360	**M19**	5	170

Although catalysts **M3** (furyl) and **M4** (thienyl) possess substituents with heteroatoms (O or S) which may in principle interact with the alkyl aluminum compound, no obvious impact of that on activity was noted. As a matter of fact, preliminary computational data suggest that alkyl aluminum binding to said donor atoms is endergonic at 60°C.

Using a single molecular descriptor to predict stereoselectivity. Stereoselectivity of olefin polymerization catalysts usually correlates with steric bulk at the transition metal center. The so-called 'percentage of buried volume', $\%V_{Bur}$, is a simple molecular descriptor measuring the fraction of sterically hindered volume in the first coordination sphere of a transition metal species.[29] Cavallo recommended a sphere radius of 3.5 Å to 4.0 Å for a QSAR model correlating $\%V_{Bur}$ and Bond Dissociation Energy for a benchmark set of Pd-NHC complexes (NHC = *N*-Heterocyclic Carbene). However, he noted that such a radius may be too small for QSAR models of metallocene catalysts.[30]

A related descriptor, $\Delta\%V_{Bur}$, can be introduced to quantify the difference in buried volume between 'crowded' and 'open' quadrants for C_2-symmetric *ansa*-metallocenes. DFT models suggested that $\Delta\%V_{Bur}$ should correlate rather well with the enantioselectivity of 1,2 propene insertion[31], provided that the sphere radius is properly set. With specific reference to the catalysts screened here, a comparatively large sphere is definitely needed to cover the effects of substituents in 4-position, and in particular their *ipso* and *ortho* atoms and substituents thereon, found to crucially affect the stereoselectivity (Figure 5.5). Making use of the high-quality data set produced in this work, we found that a good correlation between $\Delta\%V_{Bur}$ and σ can indeed be obtained with optimal sphere radius = 5.0 Å (spheres with radii in the 4.5–5.5 Å range all give similar correlations, whereas smaller or larger ones lead to a steep decrease of R^2).[15]

A remarkably simple QSAR expression (Eq5.1) ended up with a good ($R^2 = 0.88$) linear fit of ($\Delta\%V_{Bur}$, $\Delta\Delta G^{\ddagger}_{enantio, 60°C}$) data points ($\Delta\Delta G^{\ddagger}_{enantio, 60°C} = RT(\ln \sigma/(1-\sigma))$), as shown in Figure 5.6:

$$\Delta\Delta G\#_{enantio,60°C} = 0.4281 \times \Delta\%V_{Bur} - 2.5168 \qquad (Eq5.1)$$
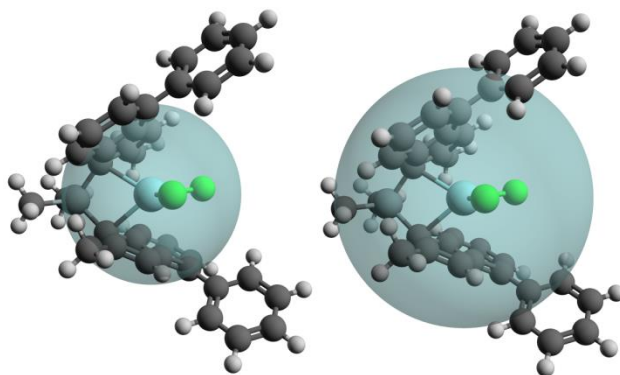
Figure 5.5. Different sphere sizes used to calculate $\Delta\%V_{Bur}$ of C_2-symmetric *ansa*-bis(1-Indenyl)Zirconocenes: (Left) 3.5 Å, (Right) 5.0 Å. Only in the latter case the substituent in 4-position is adequately covered.
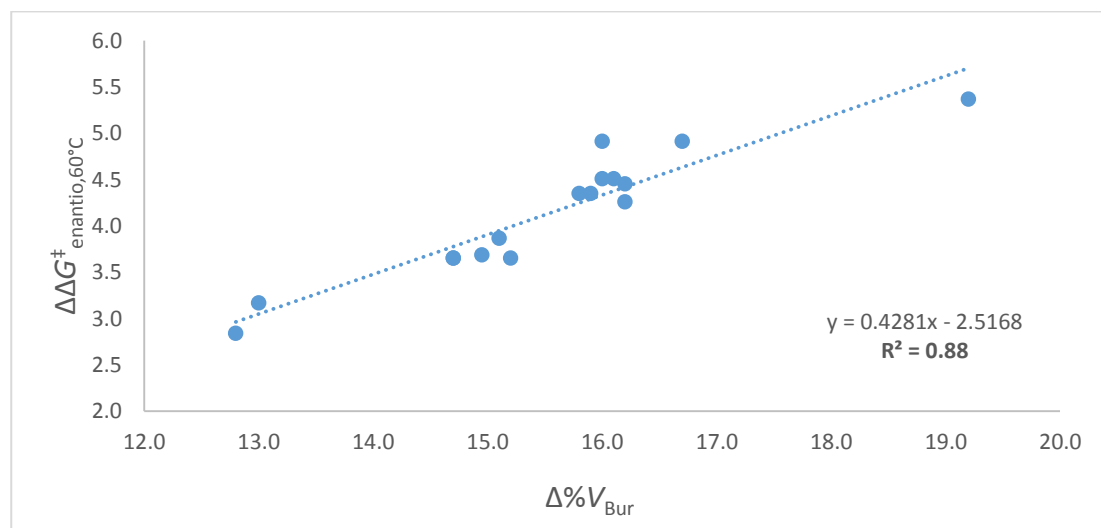
Figure 5.6. Correlation plot of $\Delta\Delta G^{\ddagger}_{enantio,\ 60°C}$ (in kcal/mol) *vs* $\Delta\%V_{Bur}$ (see text).

A leave-one-out cross-validation (LOOCV,[32,33] see ref[15] for more details) confirmed the validity of the proposed model (cross-validated R^2 (Q^2) = 0.84). A plot of predicted *vs* experimentally observed stereoselectivity for each iteration of the LOOCV showed a slope close to 1, and went nearly through the origin (y = 0.9011x + 0.3958, R^2 =0.82; y = 0.9935 and R^2 = 0.81 when constrained).

A detailed analysis of the **M3**, **M4**, **M2**, **M16, M13** sub-set can help understand why this correlation works so well. Maps of the steric bulk, as measured by %V_{Bur} and %ΔV_{Bur}, for the dichloride precatalysts are shown in Figure 5.7, along with the values of the (1-Indenyl-to-Aryl) torsion angle and those of observed catalyst enantioselectivity σ.
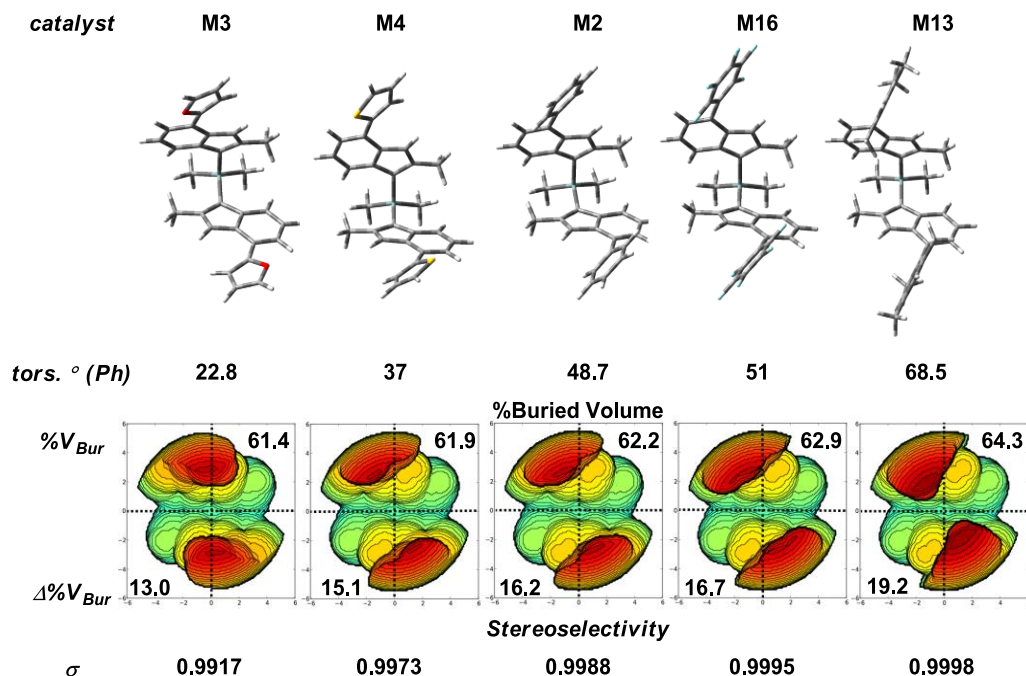
Figure 5.7 Buried volume maps for the **M3**, **M4**, **M2**, **M16**, **M13** sub-set (see text). Spheres with 5.0 radius were generated defining Zr as the center, Si-Zr as the z-axis and Si-Zr-C_{Si} as the xz plane. H-atoms were included in the analysis.

It can be seen that an increase in dihedral angle between the 4-Aryl substituent and the 1-Indenyl fragment (from 23° to 69°) is associated with an increase in %ΔV_{Bur}, which should be favorable for catalyst enantioselectivity (as long as the propene insertion TSs feature a similar trend). Experimentally, this is indeed the case. Similar to **M3** and **M4**, spherical substituents like Cl, Br and Me (**M6**, **M5**, **M7**) also bring considerable steric bulk into the 'open' quadrants and the resulting stereoselectivity is at the lower end of the range for the catalysts discussed here. DFT modeling results (Table 5.3) also lend support to the above

interpretation.[34] Notably, the calculated enantioselectivity is practically the same for propene insertion into a Zr-Me and Zr-*i*Pr bond, which indicates that direct interactions between the incoming monomer and the chiral ligand frame (rather than the chirally oriented growing polymer chain) are mainly responsible for the chiral recognition.[34]

Table 5.3. Calculated stereoselectivity ($\Delta\Delta G^{\ddagger}_{\text{enantio, DFT}}$, in kcal/mol) of propene insertion into Zr-Me and Zr-*i*Pr bonds of model catalytic species. Level of theory M06-2X(PCM)/TZ//TPSSTPSS/DZ. T = 333 K.

Catalyst	$\Delta\Delta G^{\ddagger}_{\text{enantio, DFT}}$	
	Me	**iPr**
M13*	2.4	2.5
M16	1.3	1.5
M2	0.4	0.7
M4	0.3	0.5
M3	-0.1	-0.8

*Modeled without the *para*-Me groups

Connection of Stereoselectivity, Regioselectivity and MW Capability. With the data of Table 5.1 it is possible to seek correlations between stereoselectivity, regioselectivity and MW. Some results are shown in Figures 5.8-5.9; all screened systems are included.

Stereoselectivity and regioselectivity correlate surprisingly well (R^2 = 0.71), considering that for many other metallocene catalysts they do *not*. The correlation becomes even better when the overly hindered and rigid catalyst **M13** is excluded from the set (R^2 = 0.93). Stereoselectivity and M_n do not correlate well if all catalysts are included in the plot (R^2 = 0.23), but surprisingly well instead if again **M13** is excluded (R^2 = 0.80). Since stereoselectivity correlates well with both regioselectivity and MW capability, the correlation between the latter two properties is also good (R^2 = 0.80 with **M13** excluded).
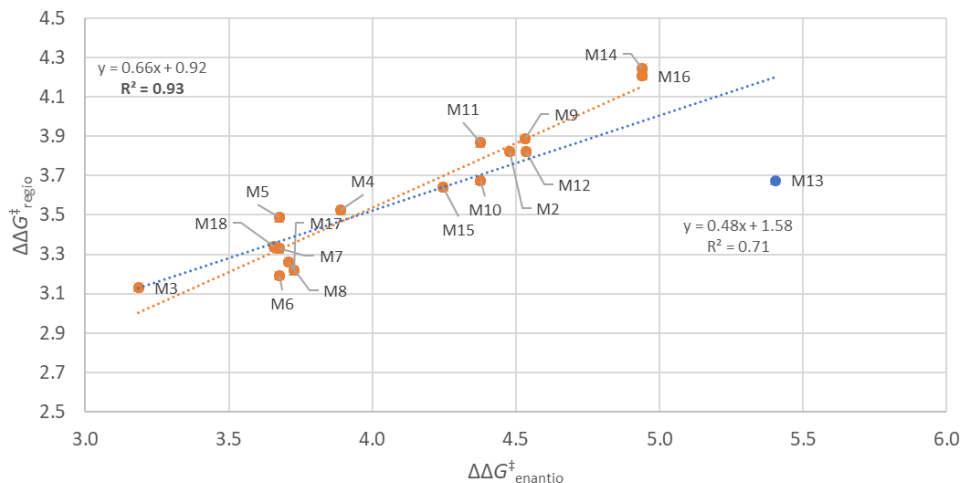
Figure 5.8. Regioselectivity ($\Delta\Delta G^{\ddagger}_{regio, 60°C}$) *vs* stereoselectivity ($\Delta\Delta G^{\ddagger}_{enantio, 60°C}$) in kcal/mol. For catalysts **M1**-**M18**, blue line, R^2 = 0.71; excluding 'over-tuned' catalyst **M13**, orange line, R^2 = 0.93.
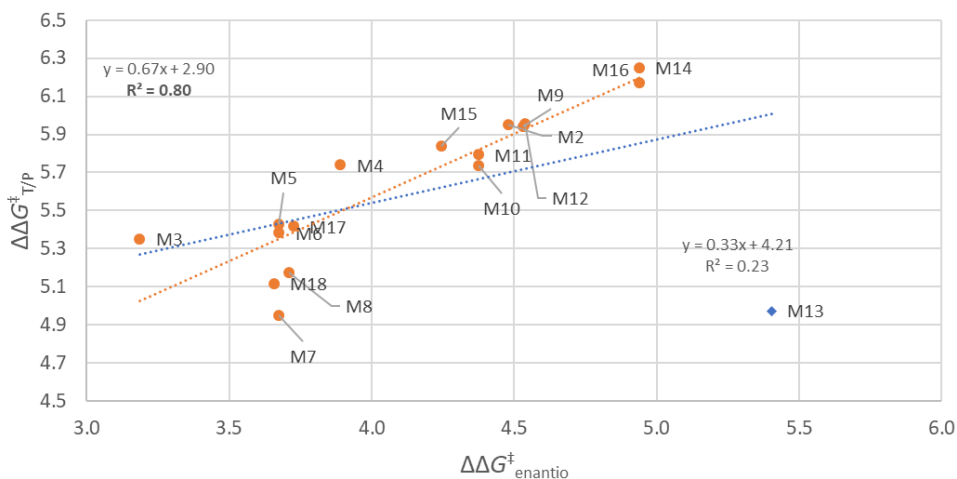
Figure 5.9. MW capability ($\Delta\Delta G^{\ddagger}_{T/P, 60°C}$) vs. stereoselectivity ($\Delta\Delta G^{\ddagger}_{enantio, 60°C}$) in kcal/mol. For catalysts **M1**-**M18**, blue line, R^2 = 0.24; excluding 'over-tuned' catalyst **M13**, orange line, R^2 = 0.80.

The catalyst with the highest stereoselectivity, namely **M13**, is clearly an exception here, and represents a case of 'over-tuning'. As a matter of fact, it does not fit well in the correlations of Figures 5.8-5.9, which can be traced to two main reasons. The buried volume maps in Figure 5.7 show that, while the substituent pattern for **M13** enhances the dissimilarity between 'open' and 'crowded' quadrants, it also amasses steric bulk near the equatorial plane and the center of the catalyst, which is not the case for the other catalysts. Furthermore, the 2,6-dimethyl substitution pattern locks the aromatic ring in place, and makes the ligand framework much more rigid. Amassing steric bulk near the equatorial plane of the catalyst is expected to increase all insertion barriers (which is in line with the very low productivity experimentally observed for this catalyst), making correlations for very different processes less likely.

Testing the prediction ability of the model. The observed correlation between stereoselectivity/regioselectivity/MW capability means that an increase in one catalyst performance indicator does not necessarily come with tradeoffs in the other performance indicators. **M14** and **M16** deliver the best overall performance of the whole catalyst set; they both give similar stereo- and regioselectivity, but the former gives higher PP MW. On the other end of the spectrum, **M3** and **M7** produce one of the shortest and 'most flawed' polymers in the test set.

The connection of dihedral angle of 4-aryl substituents, predictability of quadrant steric bulk and detrimental effect of additional steric bulk in the equatorial plane of the catalyst prompted us to test several other catalysts computationally. In particular **M19**, with a 4-*o*-tolyl substituent, was tested computationally because it avoids over-tuning by occupation of the equatorial catalyst plane and possesses an even larger dihedral angle than **M13**. While the predicted stereoselectivity remained high (σ >0.9994), we expected polymer MW to significantly increase. *Ad hoc* synthesis and testing of **M19** to verify the model confirmed the predictions. The catalyst shows the highest stereoselectivity (σ = 0.9999) reported so far for metallocene catalysts at 60°C, while maintaining a high MW capability (M_w > 1 MDa) and high regioselectivity. Although comparison is hampered by the difference in polymerization conditions, it appears that **M19** outperforms, in terms of stereoselectivity, Rieger's metallocenes (Zr/Hf: $\sigma \approx$ 0.9984/0.9984 at 60°C and $M_w \approx$ 440/900 kDa),[12,13] Spaleck's *rac*-Me$_2$Si(2-Me-4-naphthyl-indenyl)$_2$ZrCl$_2$ (σ = 0.9982 at 70°C and M_w = 920 kDa),[17] and *rac*-*n*Pr$_2$Si(2-Me-4-

phenanthryl-indenyl)$_2$ZrCl$_2$ ($\sigma \approx 0.9991$ at 0°C and M_w = 140 kDa), showing an order of magnitude less stereoerrors.[35]

5.3. Concluding remarks

In this chapter, we illustrated how the HTE polyolefin workflow introduced in Chapter 2 was successfully applied to highlight the QSAR for a set of 19 C_2-symmetric *ansa*-zirconocene propene polymerization catalysts belonging in the *rac*-R'$_2$Si(2-Me-4-R-1-Indenyl)$_2$ZrX$_2$ family, featuring substituents with variable steric demand in position 4 of the 1-Indenyl rings.

A simple QSAR model was used predictively to optimize catalyst performance. Remarkably, the overall performance of the leading catalyst thus identified turned out to surpass that of previously known metallocene catalysts that benefit from substitution in multiple positions of the indenyl fragment. We are therefore hopeful that similar studies on different substituent positions (2, 3, 5, 6 and 7-position and bridge), and a subsequent combination of the most beneficial substitution patterns, will ultimately unlock even better high-temperature/high-performance catalysts.

5.4. Experimental part

5.4.1. Catalyst synthesis

The precursor compounds 4-bromo-1-methoxy-2-methylindane,[22] bis(4-bromo-2-methyl-1*H*-inden-1-yl)dimethylsilane, bis(4-chloro-2-methyl-1*H*-inden-1-yl) dimethylsilane,[36] and Zr[PhN(CH$_2$)$_3$NPh]Cl$_2$(THF)$_2$,[37] metallocenes **M6** and **M17**,[19] **M4**,[22] **M8**,[10] **M7**, **M9**, **M10** and **M13**,[20] **M11**, **M14** and **M15**[21] were synthesized at MSU according to the literature.[38] The synthesis of **M3**, **M5**, **M12**, **M16**, **M18**, and **M19** is detailed in the supporting information of ref[15]. **M1** and **M2** were kindly donated by SABIC and used as received.

5.4.2. Polymer synthesis and characterization

Synthesis and characterization of all polypropylene samples have been performing using the HTE workflow described in Chapter 2. The polymerizations were carried out in toluene at 60°C and $p_{propene}$ of 65 or 95 psi until a desired gaseous monomer consumption was reached (reaction time 2-120 minutes), using TIBA/AB as the scavenger/activator system. 10 μmol of TIBA, 5.0 mL of solvent and 2 equivalents of AB with respect to the precatalyst were used in each reaction cell. The catalyst amount was varied in the 10-150 nmol range, depending on the catalyst. For runs using TIBA/TTB as the scavenger/activator, catalyst amounts had to be lowered down to 1-5 nmol, and the activator was used in 5 to 10-fold excess relative to the precatalyst.

The polymers were characterized by Rapid-GPC, A-CEF and ^{13}C NMR as reported in Chapter 2. We are grateful to Dr. Rocco De Girolamo for the DSC measurements.

5.4.3. Computational Details

All geometries were fully optimized using the Gaussian 09 software package[39] in combination with the OPTIMIZE routine of Baker[40,41] and the BOpt software package.[42] Following the protocol proposed in Ref.[43], all relevant minima and transition states were fully optimized at the TPSSTPSS level[44] of theory employing

correlation-consistent polarized valence double-ζ Dunning (DZ) basis sets of cc-pVDZ quality[45,46] from the EMSL basis set exchange library.[47] The protocol has been successfully used, in combination with M06-2X single point energy corrections to address several polymerization related problems: absolute barrier heights for propagation,[48] comonomer reactivity ratios,[26,49] metal-carbon bond strengths[50,51] and electronic and steric tuning effects on MW capability.[51] The density fitting approximation (Resolution of Identity, RI) was used throughout.[52-55] All calculations were performed at the standard Gaussian 09 quality settings [Scf=Tight and Int(Grid=Fine)]. All structures represent either true minima (as indicated by the absence of imaginary frequencies) or transition states (with exactly one imaginary frequency corresponding to the reaction coordinate). The SambVca 2.0 program was used to calculate $\Delta\%V_{\mathrm{Bur}}$ and generate maps of the steric bulk.[56]

References

(1)   Natta, G.; Pino, P.; Mazzanti, G.; Giannini, U. A Crystallizable Organometallic Complex Containing Titanium and Aluminum. *J. Am. Chem. Soc.* **1957**, *79* (11), 2975–2976.

(2)   Breslow, D. S.; Newburg, N. R. Bis-(Cyclopentadienyl)-Titanium Dichloride —Alkylaluminum Complexls As Catalysts for the Polymerization of Ethylene. *J. Am. Chem. Soc.* **1957**, *79* (18), 5072–5073.

(3)   Andresen, A.; Cordes, H.-G.; Herwig, J.; Kaminsky, W.; Merck, A.; Mottweiler, R.; Pein, J.; Sinn, H.; Vollmer, H.-J. Halogen-Free Soluble Ziegler Catalysts for the Polym- Erization of Ethylene. Control of Molecular Weight by Choice of Temperature[**]. *Angew. Chemie Int. Ed. English* **1976**, *15* (10), 630–632.

(4)   Sinn, H.; Kaminsky, W.; Vollmer, H.-J.; Woldt, R. "Living Polymers" on Polymerization with Extremely Productive Ziegler Catalysts. *Angew. Chemie Int. Ed. English* **1980**, *19* (5), 390–392.

(5)   Kaminsky, W. Discovery of Methylaluminoxane as Cocatalyst for Olefin Polymerization. *Macromolecules* **2012**, *45* (8), 3289–3297.

(6)   Resconi, L.; Cavallo, L.; Fait, A.; Piemontesi, F. Selectivity in Propene Polymerization with Metallocene Catalysts. *Chem. Rev.* **2000**, *100* (4), 1253–1346.

(7)   Ewen, J. A. Mechanisms of Stereochemical Control in Propylene Polymerizations with Soluble Group 4B Metallocene/Methylalumoxane Catalysts. *J Am Chem Soc* **1984**, *106* (21), 6355–6364.

(8)   Ewen, J. A.; Jones, R. L.; Razavi, A.; Ferrara, J. D. Syndiospecific Propylene Polymerizations with Group 4 Metallocenes. *J. Am. Chem. Soc.* **1988**, *110* (18), 6255–6256.

(9)   Ali, S. . *Catal. Rev.* **2014**, *27*, 7–14.

(10)   Spaleck, W.; Antberg, M.; Rohrmann, J.; Winter, A.; Bachmann, B.; Kiprof, P.; Behm, J.; Herrmann, W. A. High Molecular Weight Polypropylene through Specifically DesigneZirconocene Catalysts. *Angew. Chemie Int. Ed. English* **1992**, *31* (10), 1347–1350.

(11)   Kaminsky, W.; Külper, K.; Brintzinger, H. H.; Wild, F. R. W. P. Polymerization of Propene and Butene with a Chiral Zirconocene and Methylalumoxane as Cocatalyst. *Angew. Chemie Int. Ed. English* **1985**, *24* (6), 507–508.

(12)   Machat, M. R.; Lanzinger, D.; Pöthig, A.; Rieger, B. Ultrarigid Indenyl-Based Hafnocene Complexes for the Highly Isoselective Polymerization of Propene: Tunable Polymerization Performance Adopting Various Sterically Demanding 4-Aryl Substituents. *Organometallics* **2017**, *36* (2), 399–408.

(13)   Schöbel, A.; Herdtweck, E.; Parkinson, M.; Rieger, B. Ultra-Rigid Metallocenes for Highly Iso- and Regiospecific Polymerization of Propene: The Search for the Perfect Polypropylene Helix. *Chem. – A Eur. J.* **2012**, *18* (14), 4174–4178.

(14)   Falivene, L.; Cavallo, L.; Talarico, G. Buried Volume Analysis for Propene Polymerization Catalysis Promoted by Group 4 Metals: A Tool for Molecular Mass

Prediction. *ACS Catal.* **2015**, *5* (11), 6815–6822.

(15)   Ehm, C.; Vittoria, A.; Goryunov, G. P.; Kulyabin, P. S.; Budzelaar, P. H. M.; Voskoboynikov, A. Z.; Busico, V.; Uborsky, D. V; Cipullo, R. Connection of Stereoselectivity, Regioselectivity, and Molecular Weight Capability in *rac*-R′$_2$Si(2-Me-4-R-Indenyl)$_2$ZrCl$_2$ Type Catalysts. *Macromolecules* **2018**.

(16)   Jüngling, S.; Mülhaupt, R.; Stehling, U.; Brintzinger, H.-H.; Fischer, D.; Langhauser, F. Propene Polymerization Using Homogeneous MAO-Activated Metallocene Catalysts: Me$_2$Si(Benz[e]Indenyl)$_2$ZrCl$_2$/MAO vs. Me$_2$Si(2-Me-Benz[e]Indenyl)$_2$ZrCl$_2$/MAO. *J. Polym. Sci. Part A Polym. Chem.* **1995**, *33* (8), 1305–1317.

(17)   Spaleck, W.; Kueber, F.; Winter, A.; Rohrmann, J.; Bachmann, B.; Antberg, M.; Dolle, V.; Paulus, E. F. The Influence of Aromatic Substituents on the Polymerization Behavior of Bridged Zirconocene Catalysts. *Organometallics* **1994**, *13* (3), 954–963.

(18)   Kuklin, M. S.; Virkkunen, V.; Castro, P. M.; Resconi, L.; Linnolahti, M. Controlling the Microstructure of Isotactic Polypropene by C2-Symmetric Zirconocene Polymerization Catalysts: Influence of Alkyl Substituents on Regio- and Stereocontrol. *Eur. J. Inorg. Chem.* **2015**, *2015* (26), 4420–4428.

(19)   Voskoboynikov, A. Z.; Ryabov, A. N.; Nikulin, M. V; Lygin, A. V; Izmer, V. V; Asachenko, A. F.; Coker, C. L.; Canich, J. A. M. Halogen Substituted Metallocene Compounds for Olefin Polymerization. US7446216, 2004.

(20)   Voskoboynikov, A. Z.; Ryabov, A. N.; Coker, C. L.; Canich, J. A. M. Process for Producing Substituted Metallocene Compounds for Olefin Polymerization. US7709670, 2004.

(21)   Voskoboynikov, A. Z.; Nikulin, M. V; Ryabov, A. N.; Lygin, A. V; Coker, C. L.; Canich, J. A. M. Preparation of Substituted Bridged Indenyl and Related Ligands. US7910783, 2005.

(22)   Izmer, V. V; Lebedev, A. Y.; Nikulin, M. V.; Ryabov, A. N.; Asachenko, A. F.; Lygin, A. V.; Sorokin, D. A.; Voskoboynikov, A. Z. Palladium-Catalyzed Pathways to Aryl-Substituted Indenes: Efficient Synthesis of Ligands and the Respective Ansa-Zirconocenes. *Organometallics* **2006**, *25* (5), 1217–1229.

(23)   Busico, V.; Brita, D.; Caporaso, L.; Cipullo, R.; Vacatello, M. Interfering Effects of Growing Chain Epimerization on Metallocene-Catalyzed Isotactic Propene Polymerization. *Macromolecules* **1997**, *30* (14), 3971–3977.

(24)   Busico, V.; Cipullo, R.; Kretschmer, W. P.; Talarico, G.; Vacatello, M.; Van Axel Castelli, V. "Oscillating" Metallocene Catalysts: How Do They Oscillate? *Angew. Chemie Int. Ed.* **2002**, *41* (3), 505–508.

(25)   Curtin, D. Y. Stereochemical Control of Organic Reactions. Differences in Behavior of Diastereoisomers. I. Ethane Derivatives. The Cis Effect. *Rec. Chem. Progr.* **1954**, *15*, 111–128.

(26)   Zaccaria, F.; Ehm, C.; Budzelaar, P. H. M.; Busico, V. Accurate Prediction of Copolymerization Statistics in Molecular Olefin Polymerization Catalysis: The Role of Entropic, Electronic, and Steric Effects in Catalyst Comonomer Affinity. *ACS Catal.* **2017**, *7*, 1512–1519.

(27)   Förster, H.; Vögtle, F. Steric Interactions in Organic Chemistry: Spatial

Requirements of Substituents. *Angew. Chemie Int. Ed. English* **1977**, *16* (7), 429–441.

(28)   Kuklin, M. S.; Virkkunen, V.; Castro, P. M.; Izmer, V. V; Kononovich, D. S.; Voskoboynikov, A. Z.; Linnolahti, M. Quantitative Structure–property Relationships in Propene Polymerization by Zirconocenes with a *rac*-SiMe$_2$[Ind]$_2$ Based Ligand Framework. *J. Mol. Catal. A Chem.* **2016**, *412*, 39–46.

(29)   Viciu, M. S.; Navarro, O.; Germaneau, R. F.; Kelly, R. A.; Sommer, W.; Marion, N.; Stevens, E. D.; Cavallo, L.; Nolan, S. P. Synthetic and Structural Studies of (NHC)Pd(Allyl)Cl Complexes (NHC = *N* -Heterocyclic Carbene). *Organometallics* **2004**, *23* (7), 1629–1635.

(30)   Poater, A.; Cavallo, L. Comparing Families of Olefin Polymerization Precatalysts Using the Percentage of Buried Volume. *Dalt. Trans.* **2009**, No. 41, 8885–8890.

(31)   bahri-Laleh, N.; Falivene, L.; Cavallo, L. Testing DFT Ability to Predict the Stereoselectivity of Group 4 Metallocenes in Propylene Polymerization. *Polyolefins J.* **2014**, *1* (2), 139–146.

(32)   Cramer, R. D.; Patterson, D. E.; Bunce, J. D. Comparative Molecular Field Analysis (CoMFA). 1. Effect of Shape on Binding of Steroids to Carrier Proteins. *J. Am. Chem. Soc.* **1988**, *110* (18), 5959–5967.

(33)   Alexander, D. L. J.; Tropsha, A.; Winkler, D. A. Beware of R^2: Simple, Unambiguous Assessment of the Prediction Accuracy of QSAR and QSPR Models. *J. Chem. Inf. Model.* **2015**, *55* (7), 1316–1322.

(34)   Talarico, G.; Budzelaar, P. H. M. Analysis of Stereochemistry Control in Homogeneous Olefin Polymerization Catalysis. *Organometallics* **2014**, *33* (21), 5974–5982.

(35)   Kashiwa, N.; Kojoh, S.; Imuta, J.; Tsutsui, T. Characterization of PP Prepared with the Latest Metallocene and MgCl2-Supported TiCl4 Catalyst Systems. In *Metalorganic Catalysts for Synthesis and Polymerization*; Kaminsky, W., Ed.; Springer Berlin Heidelberg: Berlin, Heidelberg, 1999; pp 30–37.

(36)   Nikulin, M. V; Tsarev, A. A.; Lygin, A. V; Ryabov, A. N.; Beletskaya, I. P.; Voskoboinikov, A. Z. Palladium Catalyzed Arylation of Bis (4-Bromo-2-Methylinden-1-Yl) Dimethylsilane and Related Compounds. **2008**, *57* (11), 2298–2306.

(37)   Zhang, X.; Zhu, Q.; Guzei, I. A.; Jordan, R. F. General Synthesis of Racemic Me$_2$Si-Bridged Bis(Indenyl) Zirconocene Complexes [12]. *J. Am. Chem. Soc.* **2000**, *122* (33), 8093–8094.

(38)   Bingel, C.; Goeres, M.; Fraaije, V.; Winter, A. Preparation of Preparing Substituted Indanones. US6492539, 2002.

(39)   Frisch, M. J.; Trucks, G. W.; Schlegel, H. B.; Scuseria, G. E.; Robb, M. A.; Cheeseman, J. R.; Scalmani, G.; Barone, V.; Mennucci, B.; Petersson, G. A.; et al. Gaussian 09, Revision B.01. *Gaussian 09, Revision B.01, Gaussian, Inc., Wallingford CT*. 2009.

(40)   Baker, J. 2.4 Ed. In *J. Parallel Quantum Solutions*; Fayetteville, AR, 2001.

(41)   Baker, J. An Algorithm for the Location of Transition States. *J Comput Chem* **1986**, *7* (4), 385–395.

(42)   Budzelaar, P. H. M. Geometry Optimization Using Generalized, Chemically Meaningful Constraints. *J Comput Chem* **2007**, *28* (13), 2226–2236.

(43)   Ehm, C.; Budzelaar, P. H. M.; Busico, V. Calculating Accurate Barriers for Olefin Insertion and Related Reactions. *J. Organomet. Chem.* **2015**, *775*, 39–49.

(44)   Tao, J.; Perdew, J. P.; Staroverov, V. N.; Scuseria, G. E. Climbing the Density Functional Ladder: Nonempirical Meta\char21{}Generalized Gradient Approximation Designed for Molecules and Solids. *Phys. Rev. Lett.* **2003**, *91* (14), 146401.

(45)   Balabanov, N. B.; Peterson, K. A. Systematically Convergent Basis Sets for Transition Metals. I. All-Electron Correlation Consistent Basis Sets for the 3d Elements Sc–Zn. *J. Chem. Phys.* **2005**, *123* (6), 64107.

(46)   Balabanov, N. B.; Peterson, K. A. Basis Set Limit Electronic Excitation Energies, Ionization Potentials, and Electron Affinities for the 3d Transition Metal Atoms: Coupled Cluster and Multireference Methods. *J. Chem. Phys.* **2006**, *125* (7), 74110.

(47)   Schuchardt, K. L.; Didier, B. T.; Elsethagen, T.; Sun, L.; Gurumoorthi, V.; Chase, J.; Li, J.; Windus, T. L. Basis Set Exchange: A Community Database for Computational Sciences. *J. Chem. Inf. Model.* **2007**, *47* (3), 1045–1052.

(48)   Ehm, C.; Cipullo, R.; Budzelaar, P. H. M.; Busico, V. Role(s) of TMA in Polymerization. *Dalt. Trans.* **2016**, *45* (16), 6847–6855.

(49)   Zaccaria, F.; Cipullo, R.; Budzelaar, P. H. M.; Busico, V.; Ehm, C. Backbone Rearrangement during Olefin Capture as the Rate Limiting Step in Molecular Olefin Polymerization Catalysis and Its Effect on Comonomer Affinity. *J. Polym. Sci. Part A Polym. Chem.* **2017**, *55* (17), 2807–2814.

(50)   Ehm, C.; Cipullo, R.; Passaro, M.; Zaccaria, F.; Budzelaar, P. H. M.; Busico, V. Chain Transfer to Solvent in Propene Polymerization with Ti Cp-Phosphinimide Catalysts: Evidence for Chain Termination via Ti–C Bond Homolysis. *ACS Catal.* **2016**, *6* (11), 7989–7993.

(51)   Ehm, C.; Budzelaar, P. H. M.; Busico, V. Tuning the Relative Energies of Propagation and Chain Termination Barriers in Polyolefin Catalysis through Electronic and Steric Effects. *Eur. J. Inorg. Chem.* **2017**, 3343–3349.

(52)   Whitten, J. L. Coulombic Potential Energy Integrals and Approximations. *J. Chem. Phys.* **1973**, *58*, 4496.

(53)   Baerends, E. J.; Ellis, D. E.; Ros, P. Self-Consistent Molecular Hartree—Fock—Slater Calculations I. The Computational Procedure. *Chem. Phys.* **1973**, *2* (1), 41–51.

(54)   Feyereisen, M.; Fitzgerald, G.; Komornicki, A. Use of Approximate Integrals in Ab Initio Theory. An Application in MP2 Energy Calculations. *Chem. Phys. Lett.* **1993**, *208* (5), 359–363.

(55)   Vahtras, O.; Almlöf, J.; Feyereisen, M. W. Integral Approximations for LCAO-SCF Calculations. *Chem. Phys. Lett.* **1993**, *213* (5), 514–518.

(56)   Falivene, L.; Credendino, R.; Poater, A.; Petta, A.; Serra, L.; Oliva, R.; Scarano, V.; Cavallo, L. SambVca 2. A Web Tool for Analyzing Catalytic Pockets with Topographic Steric Maps. *Organometallics* **2016**, *35* (13), 2286–2293.

6. HTE for molecular kinetic investigations: The case of Polyolefin Chain Shuttling

6.1. Introduction

Over the last decades, the production of polymers with novel architectures and end-use properties using commercially abundant and cheap monomers has attracted significant attention. Ethene is the simplest and least expensive olefin monomer; therefore, it is by no means surprising that polyethylene based materials have become the largest volume polymers and one of the most important chemical products in the market. These materials include the homopolymer (High-Density Polyethylene, HDPE), which is a typical thermoplastic material, as well as random copolymers of ethene with a higher olefin (e.g. 1-hexene, 1-octene), comprehensively known as Linear Low-Density Polyethylene (LLDPE) and featuring elastomeric or elastoplastic behaviors.

The wealth of molecular (metallocene and post-metallocene) olefin polymerization catalysts opened the door to polyolefins with tailored microstructures and architectures.[1] In the case of polyethylene, this meant fine control over the average number and distribution of short and long chain branches.[2,3] However, a necessary correlation between density and melting temperature (Figure 6.1) has long represented a paradigm.[4] Ethene copolymers made with multi-sited catalysts (e.g., Ziegler-Natta systems) seem not to follow

the master curve only because they are physical blends, but each of the constituting fractions in reality obeys the relationship in the figure.
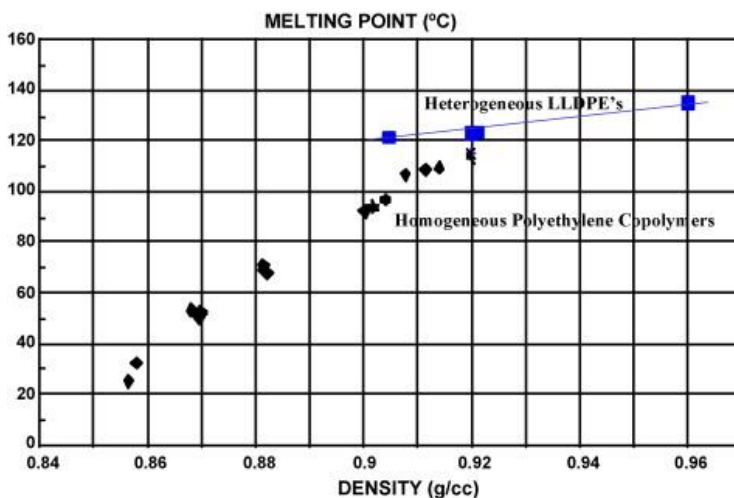
Figure 6.1. Correlation between melting temperature and density for ethene/1-octene copolymers produced with homogeneous and heterogeneous catalysts.[4]

Breaking the paradigm is only possible with Olefin Block Copolymers (OBCs). The synthesis of well-defined OBCs has become possible in the last decade of the 1990s, after the discovery of 'living' molecular catalysts. These enable the sequential polymerization of different monomers or mixtures of comonomers without chain transfer or termination events, ending up with block chain architectures.[5–7] In particular, OBC with HDPE and LLDPE blocks do not follow the curve of Figure 6.1, because their density and melting temperature can be controlled independently by tuning the relative amounts of HDPE and LLDPE blocks, the composition of the latter, and the length of the former (Figure 6.2). Such materials are valuable for applications as thermoplastic elastomers (TPEs) or phase compatibilizers. Unfortunately, the living polymerization route has the drawback that each catalyst molecule can yield at most one single OBC chain, which is not sustainable in view of the high catalyst cost.
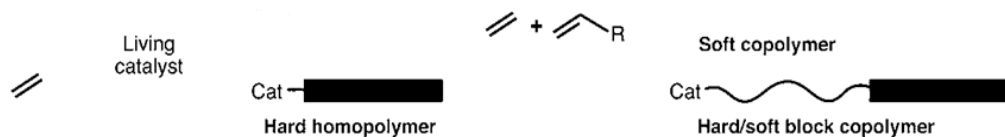
Figure 6.2. Schematic representation of the living polymerization approach to hard/soft ethene OBCs.[8]

In the mid-2000s, Dow Chemical researchers disclosed an innovative catalytic strategy for the production of OBCs, which they denominated 'Chain Shuttling Polymerization'.[8–10]

The idea of polyolefin 'chain shuttling' is almost as old as catalytic olefin polymerization itself. As a matter of fact, Natta noted the trans-alkylating ability of triethyl-Al and diethyl-Zn with early $TiCl_3$-based polypropylene catalysts, and traced the stereoblock fraction found in the polymer to the repeated exchange of polymeryls growing at different surface sites with the mediation of the main group metal cocatalyst.[11,12] Whereas this interpretation turned out to be incorrect at a later stage,[12-14] it had the merit to introduce the concept of reversible trans-alkylation between two or more diverse catalysts by means of a suitable 'Chain Shuttling Agent' (CSA) as a way to produce olefin stereoblock polymers[13] and, by extension, olefin block copolymers (OBCs).[10] Yet, it took several decades and the decisive contribution of HTE methods to ultimately identify well-working molecular catalyst formulations, which seem to be rare.[9,10]

From the kinetic standpoint, 'Chain Shuttling Copolymerization' (CSC) represents a special case of 'Coordinative Chain Transfer Polymerization' (CCTP).[15,16] An olefin CCTP process (Figure 6.3-A) can be described as one in which fast and reversible trans-alkylation between a transition metal (^tM) polymerization catalyst and a conveniently large excess of a main group metal (^{mg}M) alkyl such as e.g. diethyl-Zn (DEZ), acting as a Chain Transfer Agent (CTA), generates a pool of 'dormant' ^{mg}M-Polymeryls which undergo intermittent growth when temporarily delivered to ^tM centers. The average chain growth time on the ^tM catalyst in the absence of the ^{mg}M species (t_{cg}) is extended by a factor $\tau \geq n[^{mg}M]/[^tM]$, where n is the average number of polymeryls bound to each ^{mg}M center. As long as the experiment time t for a (semi)batch process, or the average catalyst residence time for a continuous process, is (well) below τt_{cg}, a linear relationship between polymer yield (Y) and average molecular weight (MW) holds. If, additionally,

chain initiation is fast relative to propagation, the process mimics a living polymerization, and the molecular weight distribution (MWD) of the polymer produced in (semi)batch experiments approaches the Poisson function (PDI = $M_w/M_n = 1.0$).[15–17]

In the CSC variant (Figure 6.3-B),[9,10,17] a combination of two [t]M catalysts is used along with a CTA (CSA) to copolymerize ethene and a 1-alkene. When the catalysts differ in their 1-alkene incorporation ability, OBCs with an alternation of blocks with different compositions can be produced. At odds with the well-defined architectures achievable by controlled ('living') catalysis,[7] CSC products have statistically distributed block numbers and lengths; on the other hand, a large excess of copolymer chains can be obtained with respect to the (usually expensive) [t]M species, which is a tremendous advantage for practical application.
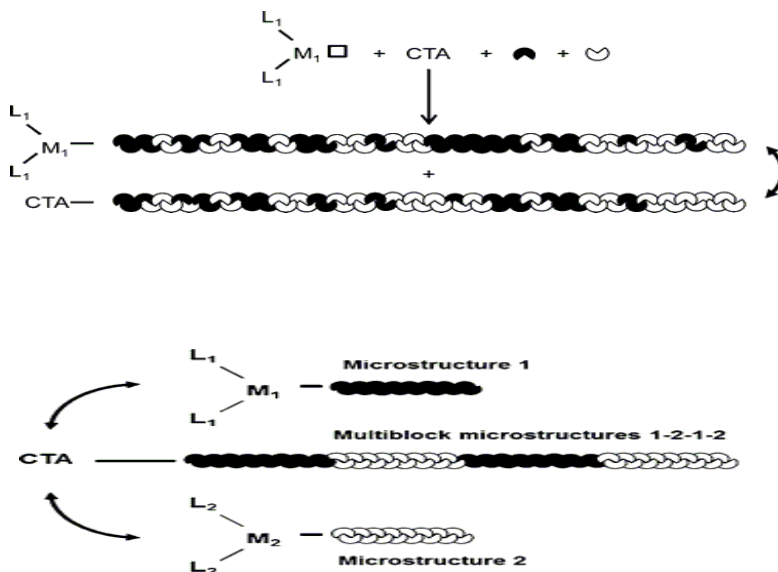
Figure 6.3. Schematic representation of (A) Coordinative Chain Transfer Polymerization (CCTP, Top) and (B) Chain Shuttling Copolymerization (CSC, Bottom).[15] See text for details.

The CSC route is now used commercially by Dow Chemical to produce ethene/1-octene (E/O) OBCs under the Infuse™ tradename.[4] Copolymerization occurs in a single reactor in the presence of a bis(phenoxyimine)Zr catalyst[9,18] (e.g. CAT-1 of

Scheme 6.1) and a (pyridylamido)Hf catalyst[9,19] (e.g. CAT-2 of Scheme 6.1), with diethyl-Zn (DEZ) as the CSA.[9,10,17] Notably, both catalysts are characterized by multiple active species: CAT-1 can speciate into several isomers,[18] whereas CAT-2 undergoes an in-situ ligand diversification by comonomer insertion into the strained *ortho*-metalated bond of the naphthyl fragment.[20,21] CAT-1 is much less reactive towards O than CAT-2;[9,10] therefore, at a given [E]/[O] feeding ratio, O-poor ('hard') and O-rich ('soft') copolymers are produced at CAT-1 and CAT-2, respectively. Fast and reversible trans-alkylation of the growing chains with the CSA results into statistically distributed hard-soft multiblock architectures.[9,10] The relative amounts of hard and soft blocks, as well as their average numbers, lengths and compositions, can be tuned (within the constraints inherent in the nature of the catalyst pair[22]) by adjusting the relative amounts of the two catalysts and of the CSA, as well as monomer concentrations.[10,17]
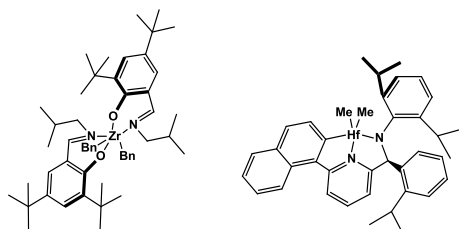
Scheme 6.1. The bis(phenoxyimine)Zr (CAT-1, left) and (pyridylamido)Hf (CAT-2, right) precatalysts.

Infuse™ OBCs are unique materials. As already noted, they escape the long-standing correlation between density and melting temperature of conventional LLDPE.[4,8–10,23] Self-separation of the hard and soft blocks into semicrystalline and amorphous domains is typically observed;[23–25] grades with long hard blocks and an excess of soft blocks behave as thermoplastic elastomers.[4,8–10,23]

Whereas the general kinetic aspects of the polymerization process[8,10] and the physical properties of the products[23–25] are rather well understood, the details are still poorly defined. To the best of our knowledge, even average block numbers and lengths of commercial Infuse™ grades are not available in the public domain, which hampers a thorough elucidation of structure-properties relationships.

We can only speculate on the reasons for this impasse, which is unusual considering that more than ten years have passed since the initial discovery. One is likely the technical complexity of the catalytic reaction. CCTP and CSC can only

occur in solution, because the mobility of the M-polymeryl species is a necessary condition. For chains with high-melting hard blocks, this requires high-temperature operation (e.g. 100°C or above); yet, the vast majority of the literature studies were carried out at moderate temperature[7,8], probably because controlling olefin polymerization reactions under conditions at which catalytic activities are exceedingly high, all deactivation processes are very fast, and the reaction is over in few minutes is challenging even for industry, and very few academic laboratories are equipped to do that well enough.

The microstructural and structural assessment of OBCs is also deceptive. Most polyolefin materials on the market are physical blends that can be separated into the different components prior to the characterizations. With block copolymers this approach is conceptually hampered, because the different blocks are chemically bound, and therefore inseparable. On the other hand, typical Infuse™ samples can be separated into comparable amounts of a completely amorphous fraction and a high-melting semicrystalline fraction,[26,27] which highlights an extensive inter-chain disuniformity of yet unclear origin(s).

In this Chapter we report the results of a novel HTE approach to the question. The polyolefin workflow introduced in Chapter 2 was used for rapid and thorough explorations of the chemical and physical variables of the Dow dual catalyst system (Scheme 6.1), in order to extract detailed mechanistic information. The two catalysts were first screened individually in ethene/1-hexene (E/H) CCTP, and then together in E/H CSC, in both cases at 100°C. The robust database resulting from the screening enabled us to effectively factor the problem, and ultimately disambiguate data interpretation, ending up with a semi-quantitative description of OBC microstructure and architecture, and a mechanistic interpretation thereof.

This part of the project has been recently published.[28]

6.2. Experimental part

6.2.1. *Materials*

All air-/moisture-sensitive chemicals were manipulated under argon or nitrogen using Schlenk techniques and/or MBraun LabMaster 130 glove boxes.

The bis(phenoxyimine)Zr[29] and (pyridylamide)Hf precatalysts[30] were prepared according to the literature. All liquid and gaseous reagents used for the polymerization experiments were purified by passing them through mixed-bed activated-Cu/A4-molecular-sieves columns. All other chemicals were purchased and used as received, unless stated otherwise.

6.2.2. *Copolymerization experiments and copolymer characterizations*

The ethene/1-hexene copolymerization experiments were conducted following the general protocol presented in Section 2.3. ISOPAR-G was used as the solvent, methylaluminoxane (MAO, [Al]=0.1M) as the scavenger, N,N-dimethylanilinium tetrakis-perfluorophenylborate (AB) as the activator, and DEZ as the CSA.

The copolymer samples as obtained after the drying step can be macroscopically disuniform; therefore, a homogenization treatment was carried out prior to the characterizations. Each sample was dissolved in 5.0 mL of xylene containing 0.40 g L^{-1} of 2,6-di-*tert*-butyl-phenol (BHT) as a stabilizer. After 2 h at 135°C under gentle stirring, to ensure complete dissolution, the solutions were sequentially poured into an excess of acetone to coagulate the copolymers, which were then recovered by decantation and transferred to a Genevac EZ2-Plus centrifugal evaporator for final drying.

Rapid-GPC, ^{1}H and ^{13}C NMR analyses were carried out as reported in Section 2.3.3. A-CEF curves were collected with a Polymer Char setup equipped with a column cooling unit. This feature allows to extend the crystallization ramp down to a temperature as low as -20°C (below which the ODCB solvent itself crystallizes). With robotic operation, pre-weighed copolymer samples (typically 8-16 mg) were dissolved in ODCB added with 0.40 mg mL^{-1} of BHT stabilizer, so as to achieve a concentration of 2.0 mg mL^{-1}. After 90 min at 150°C under vortexing in sealed vials to ensure complete dissolution, the samples were sequentially charged into

the injection loop, where they were held at 95°C for 5 min and then moved into the column. The crystallization step entailed a 2.0°C min^{-1} cooling ramp down to -20°C at a flow rate of 0.065 mL min^{-1}; sample elution was started 1 min after reaching -20°C, with a 4°C min^{-1} heating ramp up to 140°C at a flow rate of 1.0 mL min^{-1}. The analysis time was 60 min per sample. The amount of material eluted at -20°C will be referred to as the Amorphous Fraction (AF). Elution peaks at higher temperature will be associated with the temperature at the maximum ($T_{el,max}$).

6.2.3. *Preparative fractionation*

Two commercial Infuse™ samples[4] (grades 9107 and 9507) were fractionated by exhaustive Kumagawa extraction with boiling hexane. The raw samples and fractions thereof were then characterized as previously described for the copolymers made in the PPR.

6.3.   Results and discussion

The A-CEF trace of a representative commercial Infuse™ sample (grade 9107) is shown in Figure 6.4-A. Upon elution, the sample separated into an amorphous fraction (AF; 41 wt-%), and a semicrystalline fraction featuring a broad peak; as was noted above, these observations are consistent with the previous literature.[26,27]

Preparative fractionation by Kumagawa extraction with boiling hexane confirmed the A-CEF results (Table 6.1 and Figure 6.4-B). For each fraction, the comonomer triad distribution was determined by ^{13}C NMR,[31,32] and subjected to statistical analysis. The hexane-soluble (C6-s) fraction turned out to be a purely *random* E/O copolymer with a mole fraction of O units $x_O = 0.20$. In the hexane-insoluble (C6-i, Figure 6.4-B) semi-crystalline fraction, on the other hand, random E/O copolymer sequences and an excess of EEE triads were detected, which is compatible with an OBC nature. The triad distribution was well-reproduced in the framework of a stochastic two-site model assuming the sample to be a physical blend of an ethene homopolymer (30 wt%) and a random E/O copolymer with the same composition of the C6-s fraction ($x_O = 0.20$).[33] No improvement of the fit was obtained when adopting a Coleman-Fox version of the two-site model[12–14] appropriate for block polymers; this means that the block junctures (if present) were scarce enough not to affect the triad distribution. It is worthy to note that the raw sample and the two individual fractions gave rather similar GPC traces (Figure 6.5), which implies that drawing conclusions on a possible (dis)uniformity of this and related samples based on MWD data is not always trivial.

An analogous picture was obtained for a sample of Infuse™ grade 9507 (Table 6.1 and Figure 6.4-C). Notwithstanding the multiple characterizations, based on such data it is not possible to determine unambiguously chain architecture for the two materials, nor to clarify the origin of the amorphous, purely random E/O copolymer fraction.
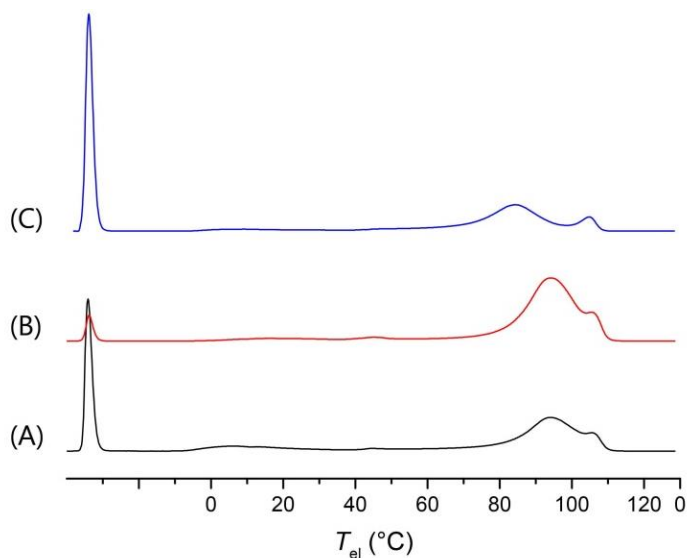
Figure 6.4. A-CEF curves of two commercial Infuse™ samples (grade 9107 (A) and 9507 (C)), and of the C6-i fraction of the former (B); see text.

Table 6.1. Results of analytical and preparative fractionation of commercial Infuse™ samples.

Fraction	(wt%)	x_0	w_s (wt%)	M_n (KDa)	M_w (KDa)	PDI	AF (wt%)	$T_{el(max)}$ (°C)
Grade 9107								
Raw		0.16	0.86	63	156	2.5	41.0	94.1 ; 107.0
s-C_6	41.1	0.20		43	113	2.6		
i-C_6	58.9	0.14		90	188	2.1		
Grade 9507								
Raw		0.17	0.89	38	101	2.7	46.1	84.3 ; 104.7
s-C_6	53.0	0.20		35	89	2.5		
i-C_6	47.0	0.14		49	117	2.4		
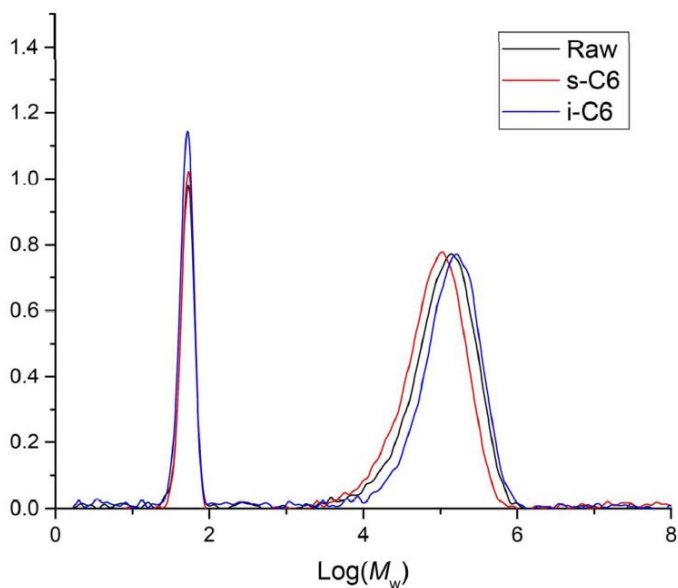
Figure 6.5. GPC curves of Infuse™ grade 9107 sample and two fractions thereof.

To disambiguate the problem, we first studied the two catalysts of Scheme 6.1 *individually* in random E/H copolymerization with and without DEZ, and then *together* in E/H CSC (Table 6.2). All experiments were carried out in alkane solution at 100°C. The catalyst system formulation included the precatalyst(s), N,N-dimethylanilinium tetrakis-perfluorophenylborate (AB), methylalumoxane (MAO), and DEZ as the CSA where applicable. In preliminary multiple-activation studies, said formulation was identified as the one ensuring the best reaction control in our setup.

The results of E/H random copolymerization (at [E]/[H] = 0.60) in the absence of DEZ are summarized at entries 1-2 (CAT-1) and 25-26 (CAT-2) of Table 6.2. Both catalysts yielded copolymers with PDI > 2.0, which is consistent with their reported non-single-center nature.[18,20,21]

Table 6.2. E/H copolymerization results with CAT-1 and CAT-2 (n.d.= not determined).

Catalyst	Entry	[Zn]/[^{t}M]	Y (mg)	M_n (KDa)	M_w (KDa)	M_w/M_n	x_H (%)
CAT-1	1	0	23	109	629	5.8	0.37
	2		28	108	638	5.9	0.35
	3	100	28	6	11	1.8	0.36
	4		41	10	17	1.6	0.35
	5		54	11	18	1.6	0.36
	6		59	14	21	1.6	0.34
	7		74	17	26	1.6	n.d.
	8		80	16	27	1.7	n.d.
	9		83	15	25	1.6	n.d.
	10		87	16	26	1.6	n.d.
	11		91	19	30	1.6	n.d.
	12		104	20	31	1.5	0.36
	13		105	23	37	1.6	0.36
	14		117	20	32	1.6	n.d.
	15		117	25	39	1.6	n.d.
	16		121	19	31	1.6	n.d.
	17		122	23	37	1.6	n.d.
	18		134	22	34	1.6	n.d.
	19		136	26	41	1.6	0.36
	20		141	24	37	1.5	n.d.
	21		168	30	45	1.5	n.d.
	22		170	29	45	1.6	n.d.
	23		209	29	47	1.6	0.36
	24		222	38	60	1.6	0.35
CAT-2	25	0	35	734	1.6×10^3	2.2	13.0
	26		41	843	1.9×10^3	2.3	14.0
	27	100	50	13	22	1.8	12.9
	28		72	19	34	1.8	12.8
	29		84	20	35	1.7	14.6
	30		92	20	36	1.8	14.7
	31		120	25	44	1.7	12.4
	32		121	25	43	1.6	13.6
	33		122	23	41	1.7	14.0
	34		126	28	46	1.6	13.4
	35		141	26	45	1.7	15.2
	36		164	38	63	1.6	14.9
	37		171	33	54	1.6	15.5
	38		190	35	58	1.6	14.2
	39		215	51	80	1.6	15.3
	40		234	45	72	1.6	16.6
	41		236	44	71	1.6	14.8
	42		250	49	80	1.6	22.0
	43		256	45	74	1.6	18.7
	44		271	50	79	1.6	20.7

The copolymers produced with CAT-1 featured a comparatively low average MW; ^{1}H NMR chain end analysis demonstrated that this can be entirely traced to β-H elimination (Figure 6.6).
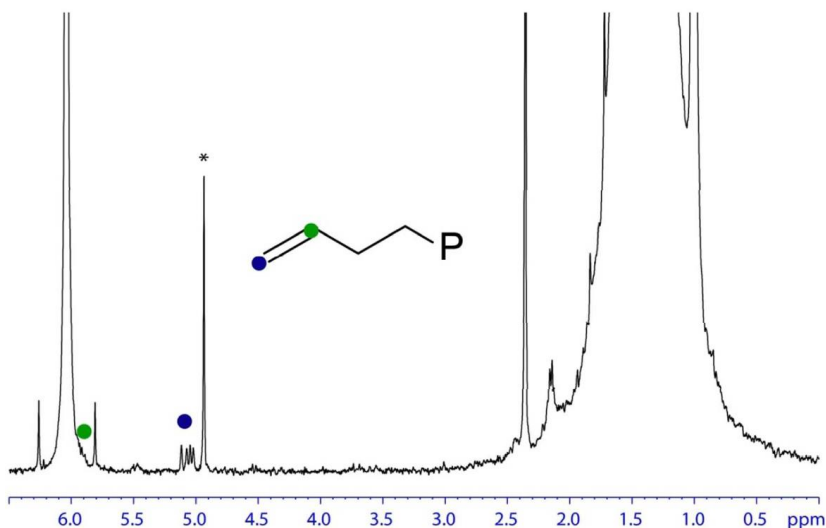
Figure 6.6. ^{1}H NMR spectrum of a typical E/H copolymer prepared with CAT-1 (*=stabilizer). The green and blue dots represent the vinyl-chain ends coming from B-H elimitaion.

The mole fraction of H units in the copolymers, as measured by ^{13}C NMR,[31] was $x_H = 0.0036$ for CAT-1, $x_H = 0.135$ for CAT-2. In the latter case, the A-CEF curves revealed the co-presence of an AF and a weakly crystalline fraction with a broad elution peak (Figure 6.7); the multi-sited nature of the catalyst, and a non-negligible amount of crystallizable $(E)_n$ sequences $(w(E)_{n \geq 10}) \approx 10$ wt%) along with a very high average MW, can both account for this observation.

Upon addition of DEZ (entries 3-24 and 27-44 of Table 6.2), copolymer MWD narrowed (to PDI <2.0), and average MW dropped dramatically. M_n *vs* Y plots (Figure 6.8) are clearly indicative of CCTP: the function is quasi-linear for CAT2, whereas the asymptotic behavior observed for CAT-1 can be ascribed to the interference of β-H elimination (in fact, the upper limit of M_n = 90 kDa determined by extrapolation agreed nicely with the value measured in the absence of DEZ).
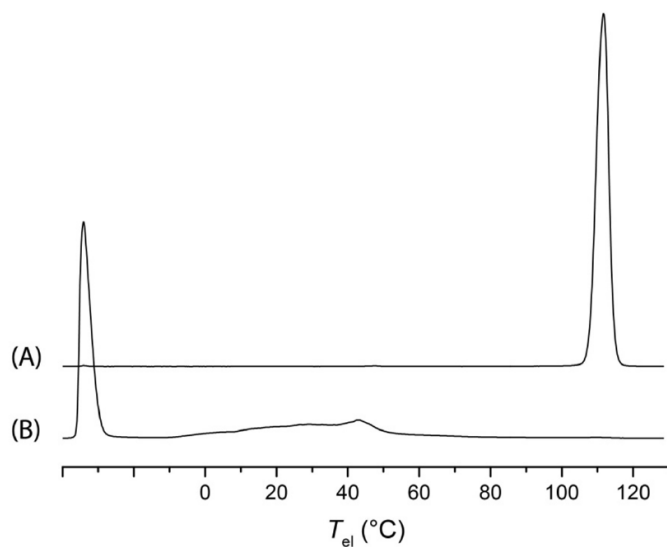
Figure 6.7. A-CEF elution curves of typical E/H random copolymer samples prepared with CAT-1 (A) and CAT-2 (B).
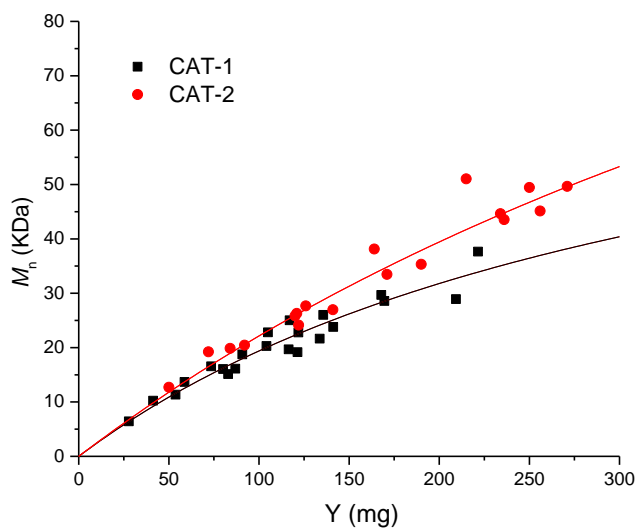
Figure 6.8. M_n *vs* Y for random E/H copolymers prepared with CAT-1 and CAT-2 under CCTP at [Zn]/[^{t}M] = 100. Data from Table 6.2.

The observed trend of the PDI, which decreases with increasing Y (Table 6.2), is typical of CCTP with a slow initiation,[15,16] possibly due to the initial buildup of 'dormant' chains on Zn starting from DEZ and the complex pool of catalytic species in each system; similar PDI values for E/O CCTP in the presence of CAT-2 with trioctyl-Al as the CSA were reported before.[34] Attaining the theoretical limit of PDI = 1.0 was not possible for CAT-1 due to the short t_{cg}, and for CAT-2 because H conversion at high Y was not negligible with our semibatch protocol. No significant effects of DEZ on copolymer composition were observed; we trace the slight tendency of x_H to increase with increasing Y (and average MW) for the copolymers made with CAT-2 (Figure 6.9) to the onset of a modest ethene mass transfer limitation from the gas to the liquid phase when the latter became very viscous (which more than compensated the effect of H conversion).
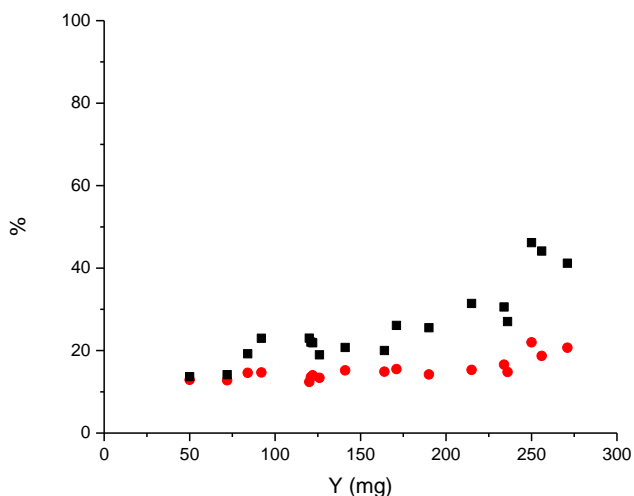
Figure 6.9. Plots of x_H (●) and $x_{H,OH}$ (■) *vs* Y for E/H copolymers prepared with CAT-2 under CCTP at [Zn]/[^tM] = 100.

It is known that the chemical structure of the growing chain is an important variable in the trans-alkylation behavior of a given catalyst.[15,16] CAT-2, in particular, was shown to be far less prone to the shuttling of polypropylene[35] or polyhexene[36] chains compared with polyethylene ones; moreover, in the previously cited E/O CCTP investigation,[34] trans-alkylation by trioctyl-Al of chains with a last-inserted O unit was reported to be negligible, which was attributed to

an excessive steric demand of the hetero-dinuclear dimer. Therefore, addressing the question how E/H CCTP is impacted by the nature of the last-inserted unit in a growing copolymer chains is important. For the system investigated here, valuable information came from ^{1}H NMR chain end analysis data. Our quenching protocol with dry air (see Chapter 2) generated OH-terminated chains, due to the reaction of O_2 with all M-Polymeryl species present in the system (M = Hf and ^{mg}M) followed by hydrolysis during the workup. Terminal HO-containing structures give idiosyncratic ^{1}H NMR signals in the region of δ = 3.5 to 4.0 ppm downfield of TMS (Figure 6.10), whose assignment was reported before;[37] differentiating and quantifying chains quenched at a last-inserted E or H unit was straightforward.
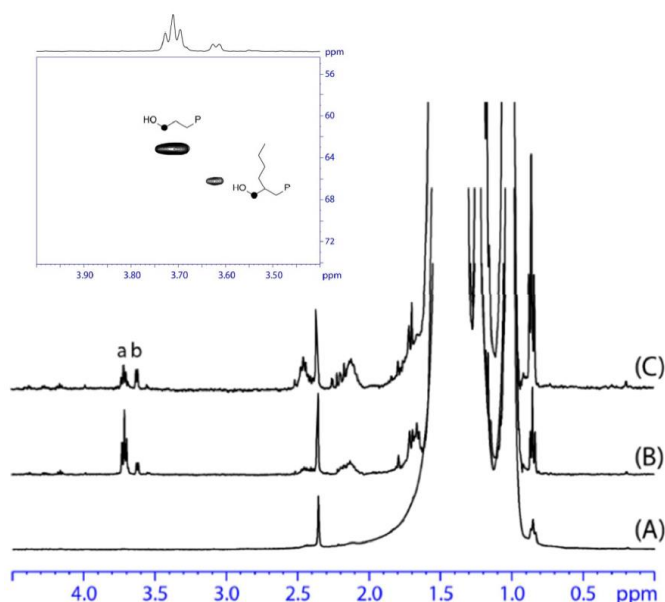
Figure 6.10. ^{1}H NMR spectra of E/H copolymer samples produced with CAT-2 in the absence (A) or in the presence of DEZ at two different yields (Y = 50 mg (B); 271 mg (C)). Signals labelled as (a) and (b) can be assigned to HO-C**H$_2$**-CH2(P) and HO-C**H$_2$**-CH(Bu)(P) chain ends, respectively.[37] In the insert, part of the HSQC-DEPT map of sample B is also shown.

With no DEZ in the catalyst system, OH-terminated copolymer chains were undetectable in the products; this is an indication that (irreversible) chain transfer to MAO (and/or to trimethyl-Al in equilibrium with it) was negligible. On the other hand, copolymers produced in the presence of DEZ featured clear ^{1}H

NMR signals due to HO-CH$_2$-CH$_2$P as well as HO-CH$_2$-CH(Bu)P chain ends (Bu = butyl). At low Y, the mole fraction of the latter ($x_{H,OH}$) was close to x_H (as measured by ^{13}C NMR); with increasing Y, though, a clear tendency of $x_{H,OH}$ to increase was observed (Figure 6.9). We conclude that, in our conditions, the shuttling of chains with a last-inserted H unit was slightly slower than that of chains with a last-inserted E unit, possibly due to the more open environment of Zn compared with Al centers.[34,36]

The data in Table 6.2 and Figure 6.9 can be used to determine the mole amounts of total and OH-terminated copolymer chains (n_P and $n_{P,OH}$, respectively) as a function of Y, and compare them with the mole amount of Zn (n_{Zn}) (Figure 6.11). For both catalysts, at low Y we estimated $n_P/n_{Zn} \approx 2$ and $n_{P,OH}/n_{Zn} \approx 1$ or slightly less; a plausible interpretation is that the pool of 'dormant' chains mainly consisted of ZnP$_2$ species (P = Polymeryl),[10,15,16] and reaction with O$_2$ (which is very complex[38]) generated on average about one P-OH moiety per Zn. For CAT-1, the increase of n_P/n_{Zn} with increasing Y was expected, in view of the comparatively fast β-H elimination process which generated 'dead' chains. On the other hand, the observation of a similar trend for both n_P/n_{Zn} and $n_{P,OH}/n_{Zn}$ with CAT-2 is not obvious: tentatively, we ascribe it to a minor contribution of Al-bound chains to the 'dormant' pool, particularly when this is enriched in chains with a last-inserted H unit. If this interpretation is correct, the fact that trans-alkylation with MAO and/or trimethyl-Al was not observed in the absence of DEZ points to trans-alkylation between Zn and Al species as the most likely source of such chains.
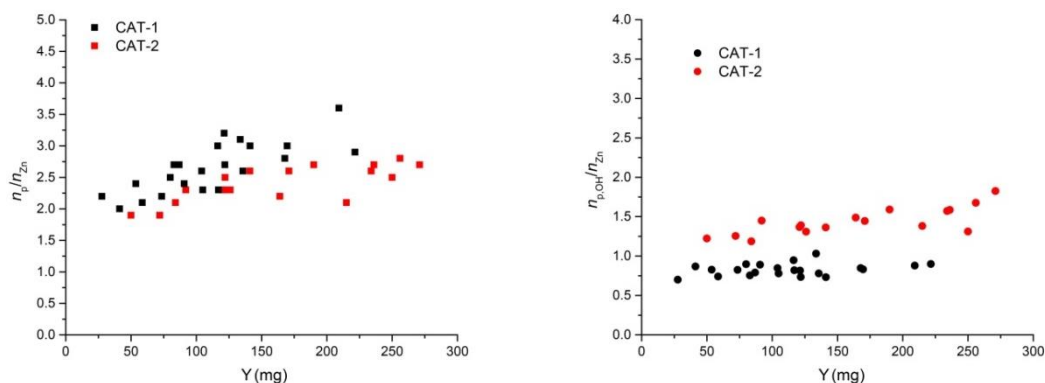

Figure 6.11. Plots of n_P/n_{Zn} (left) and $n_{P,OH}/n_{Zn}$ (right) *vs* Y for for E/H copolymers prepared with CAT-1 and CAT-2 under CCTP conditions at [Zn]/[^{t}M] = 100.

Moving from the above results, a library of experiments was designed to produce E/H OBCs by CSC. The [E]/[H] feeding ratio was set at a value of 0.35, so as to achieve a composition of the soft blocks similar to that for commercial Infuse™ products ($x_{H,s}$ = 0.20; Table 6.1). Four [CAT-1]/[CAT-2] ratios were screened, i.e. 1:1, 1:2, 1:3, 1:4; the interest for an excess of CAT-2 over CAT-1 was because commercial Infuse™ OBCs typically feature a weight fraction of soft blocks in the range of w_s = 70-80 wt% (Table 6.1). At each catalyst ratio, the [Zn]/[^{t}M] ratio was set at 0 (physical blends), 50 and 100 ([^{t}M]=[CAT-1]+[CAT-2]). A summary of the copolymerization and copolymer characterization results is reported in Table 6.3. The GPC and A-CEF curves are shown in Figures 6.12 and 6.13. For all products, the ^{13}C NMR triad distributions were subjected to statistical analysis in the framework of the two-site stochastic model described before for the commercial Infuse™ samples, in order to calculate the composition of the soft chains (blocks) and their weight fraction ($x_{H,s}$ and w_s, respectively).

Table 6.3. Main results of the E/H CSC experiments (see text). In all cases, $n(^t$M$)$ = 20 nmol.

| Entry	Catalyst system	[Zn]/[^{t}M]	Y (mg)	M_n (KDa)	M_w (KDa)	PDI	x_H (%)	w_s (wt%)	$x_{H,s}$ (%)	AF (wt%)	$T_{el(max)}$ (°C)
1	CAT-1	0	61	61	283	4.6	0.7				109.4
2	CAT-2	0	122	357	1.7×10^3	4.8	23.8				
3	[CAT-1]/[CAT-2] = 1:1 ; x_{CAT-2} = 0.50	0	137	86	758	8.8	8.7	39.6	27.7	16.1	108.6
4		50	145	36	68	1.9	7.9	42.6	22.3	1.0	107.5
5		100	165	26	45	1.7	5.9	33.0	22.0	0.4	108.1
6	[CAT-1]/[CAT-2] = 1:2; x_{CAT-2} = 0.67	0	68	158	1.5×10^3	9.6	15.7	72.6	24.1	49.6	108.7
7		50	127	35	71	2.1	12.7	66.4	21.2	6.4	105.8
8		100	129	28	50	1.8	12.9	67.7	21.0	5.0	95.4
9	[CAT-1]/[CAT-2] = 1:3 ; x_{CAT-2} = 0.75	0	97	269	1.7×10^3	6.1	16.2	77.1	22.9	67.3	108.7
10		50	154	45	90	2.0	16.0	76.7	22.4	25.8	99.6
11		100	173	29	53	1.8	15.3	79.0	21.0	21.0	94.0
12	[CAT-1]/[CAT-2] = 1:4 ; x_{CAT-2} = 0.80	0	94	299	1.9×10^3	6.5	22.1	86.7	27.0	86.9	107.9
13		50	121	38	82	2.1	17.2	83.4	21.8	39.1	94.8
14		100	182	32	58	1.8	16.5	81.3	21.3	28.3	91.2
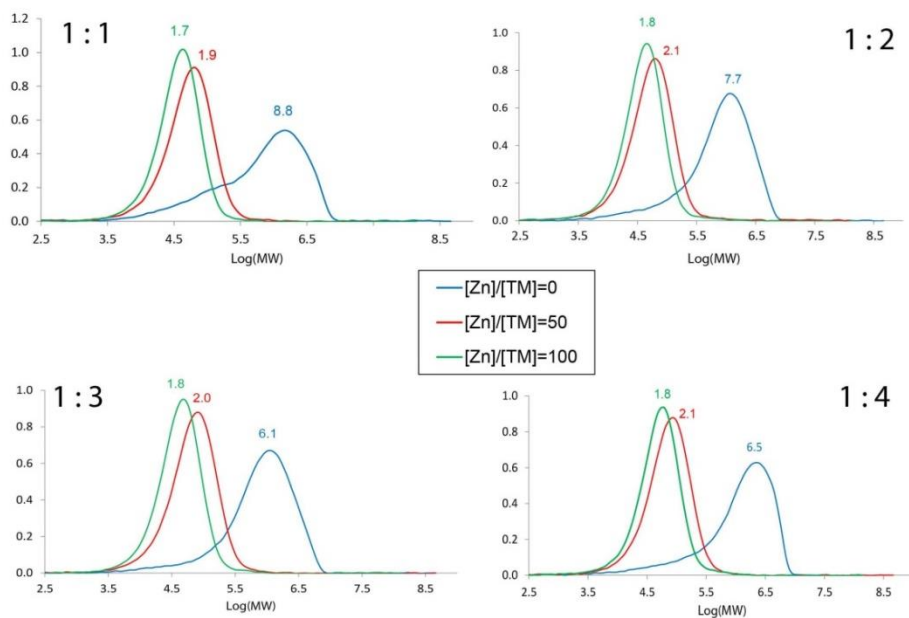
Figure 6.12 GPC traces of the E/H copolymers of Table 6.3. The [CAT-1]/[CAT-2] ratio, and the PDI values for the various MWDs, are indicated in each graph.
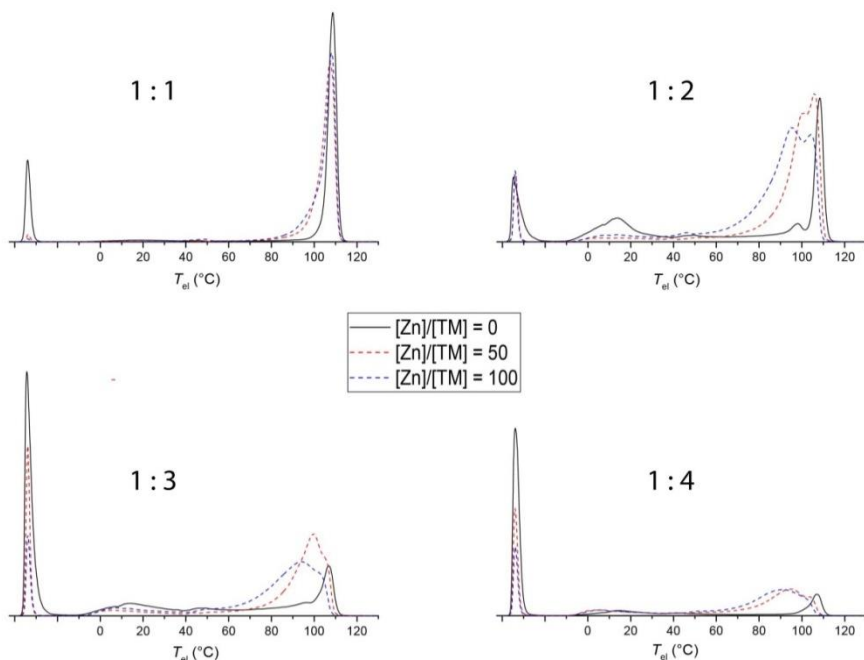

Figure 6.13. A-CEF profiles of the E/H copolymers of Table 6.3. The [CAT-1]/[CAT-2] ratio is indicated in each graph.

Ironically, the most problematic experiments to carry out and interpret were those with CAT-2 (either alone or in combination with CAT-1) and no DEZ in the catalyst formulation, because the very high average MW of the soft copolymer (component) made it difficult to prevent the aforementioned ethene mass transfer limitation issues. As a matter of fact, an E/H random copolymer sample produced with CAT-2 alone (entry 2 of Table 6.3) featured $x_H = 0.238$, and the soft component of the physical blends (entries 3, 6, 9, 12 of Table 6.3) was even richer in H ($x_{H,s}$ up to 0.28). Moreover, partial co-crystallization of the hard and soft chains prevented their complete A-CEF separation (AF < w_s). The most valuable piece of information obtained from these experiments concerned the hard copolymer component: for the E/H random copolymer sample produced with CAT-1 alone (entry 1 of Table 6.3) we measured $x_H = 0.007$ by ^{13}C NMR, and $T_{el(max)}$ = 109.4°C by A-CEF. For the physical blends (entries 3, 6, 9, 12 of Table 6.3), the $T_{el(max)}$ values were similarly high (108.5±0.6°C); therefore, in the statistical analyses of all ^{13}C NMR triad distributions we set $x_{H,h} = 0.007$.

The CSC experiments (entries 4-5, 7-8, 10-11, 13-14 of Table 6.3), on the other hand, highlighted consistent and clear trends. The following main facts should be noted:

i) The composition of the soft sequences, calculated by statistical analysis of the ^{13}C NMR triad distributions as previously described, was $x_{H,s} = 0.216±0.008$, i.e. always very close to the target ($x_{H,s} = 0.20$);

ii) The ^{13}C NMR calculated weight fraction of the soft component (w_s) was in all cases close to the mole fraction of CAT-2 (x_{CAT-2}). As a matter of fact, the two catalysts featured similar polymerization rates when used individually in E/H CCTP experiments (Table 6.2 and Figure 6.8).

iii) All GPC traces (Figure 6.12) were narrow and very symmetrical, and the PDI values were close to those measured with the individual catalysts in E/H CCTP (Table 6.2).

iv) The A-CEF traces (Figure 6.13) revealed a progressive decrease of AF and a corresponding increase of $T_{el(max)}$ with decreasing x_{CAT-2}. At $x_{CAT-2} = 0.5$, practically no AF was observed, and $T_{el(max)}$ ultimately reached the value for the random copolymer produced with CAT-1 (entries 1, 3, 6, 9, 12 of Table 6.3) within the error bar.

v) At a given x_{CAT-2}, rising [Zn]/[^tM] from 50 to 100 resulted into a decrease of $T_{el(max)}$, and of sample average MW too (due to the fact that $n_P \approx 2n_{Zn}$).

To interpret the above facts, it is worth recalling that a chain shuttling event can exchange two chains that underwent their last extension period at the same (a) or different (b) catalyst types; we will refer to case (a) as 'self-shuttling', and to case (b) as 'cross-shuttling'[25,39] Then, the number average length of a block of type-i (i = 1 or 2) can be $\underline{BL}_i$ = n($\underline{EL}_i$) (n = 1, 2, 3...), where $\underline{EL}_i$ is the number average chain extension length at CAT-i (i.e. the average polymerization degree of the chain segment grown during one extension period at said catalyst under the given experimental conditions). Let us now make the following simplifying assumptions:

I. For each catalyst, nominal and active catalyst concentration coincide

II. $k_{p1} = k_{p2} = k_p$

III. $k_{cs-ii} = k_{cs-ij} = k_{cs}$ (i.e., the specific rates of all chain shuttling events are the same)

Then, the following simple relationships should hold:

$\underline{BL}_1/\underline{BL}_2 \approx$ [CAT-1]/[CAT-2]   (at a given [Zn])   (Rel.6.1)

$\underline{EL}_1 = \underline{EL}_2 = \underline{EL}$ (Rel.6.2)

$\underline{EL} \propto 1/$[Zn]   (at given [CAT-1] or [CAT-2])   (Rel.6.3)

$\underline{BL}_i \rightarrow \underline{EL}$ for $x_{CAT-i} \rightarrow 0$ (Rel.6.4)

Of course, $\underline{BL}_1 = \underline{BL}_h$; $\underline{BL}_2 = \underline{BL}_s$; $M_{n,i} = \underline{BL}_i M^0_i$ (where M^0_i is the reduced monomer mass of a block of type-i: in our conditions, $M^0_h \approx 28$ Da, $M^0_s \approx 39$ Da).

Furthermore, we will assume that $T_{el(max)}$ in the aCEF profile of an OBC sample is determined solely by the average length of the ethene homosequences in the hard blocks (made at CAT-1). Then, we should observe $T_{el(max)} \approx 109°$C when $\underline{BL}_h >$ 1/0.007; otherwise, for $\underline{BL}_h \leq 1/0.007$, the value of $T_{el(max)}$ should be close to that for an E/H random copolymer with $1/x_H = \underline{BL}_h$ (corrected for the average length of the ethene homosequences in the soft blocks in case $\underline{BL}_h$ is not much greater than $1/x_{H,s}$). An experimental $\{1/x_H, T_{el(max)}\}$ correlation plot for a series of E/H random copolymers prepared with a molecular catalyst is shown in Figure 6.14.

Based on the above, for all E/H CSC products of Table 3 we estimated $\underline{BL}_h$ from $T_{el(max)}$ (Table 6.3), and then $\underline{BL}_s$ according to Rel.6.1. The results are given in Table 6.4. In view of Rels. 6.2 and 6.4, for the samples produced at the lowest x_{CAT-1} (entries 11 and 12 of Table 6.3) we suggest that $\underline{BL}_h \approx \underline{EL}$, i.e. ca. 40 monomeric units at [Zn]/[^{t}M] = 50; ca. 20 monomeric units at [Zn]/[^{t}M] = 100.
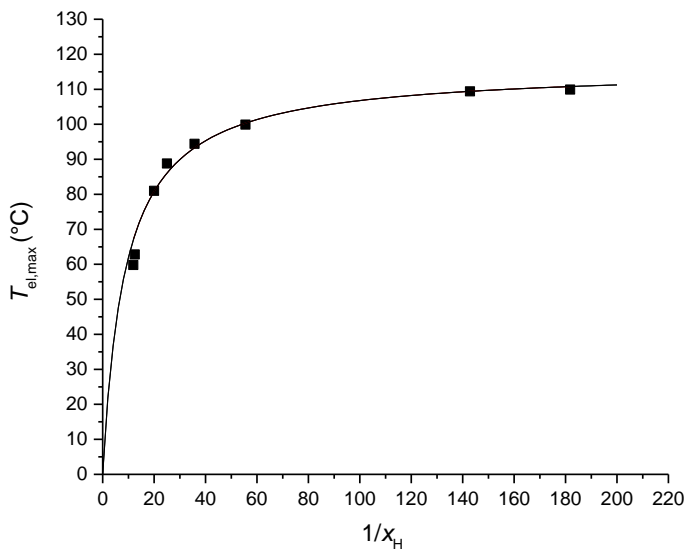
Figure 6.14. $T_{el(max)}$ *vs* $1/x_H$ for a series of E/H random copolymers.

Table 4. Estimated values of $\underline{BL}_h$ and $\underline{BL}_s$ for the E/H CSC samples of Table 3 (see text).

Entry	x_{CAT-2}	$[Zn]/[{}^tM]$	$\underline{BL}_h$ (monom. units)	$\underline{BL}_s$ (monom. units)	$\underline{M}_{n,h}$ (KDa)	$\underline{M}_{n,s}$ (KDa)
4	0.50	50	>1.4×10²	>1.4×10²	>3.9	>5.5
5	0.50	100	≥1.4×10²	≥1.4×10²	≥3.9	≥5.5
7	0.67	50	90	180	2.5	7.0
8	0.67	100	40	80	1.1	3.1
10	0.75	50	55	165	1.5	6.4
11	0.75	100	30*	90	0.84	3.5
13	0.80	50	40	160	1.1	6.2
14	0.80	100	20*	80	0.56	3.1

*Corrected for the number average length of the ethene homosequences in the soft blocks (4 monomeric units; see text)

Despite of the very rough approximations and within the large experimental uncertainties, the values in Table 6.4 seem rather consistent, internally and with respect to Rel.6.3. Therefore, we will take them as a plausible semi-quantitative basis to describe sample architecture in the produced copolymers.

Our first conclusion is that all samples are true OBCs; the pronounced inter-chain disuniformity observed for most of them is the result of a low number of blocks per chain (between 1 and 10, indicatively).[39] In particular, the AF is made of purely random copolymer chains which underwent exclusively 'self-shuttling' at CAT-2, and as such only contain one soft block. In line with this interpretation, the AF turned out to decrease with decreasing x_{CAT-2}, and was practically absent at $x_{CAT-2} = 0.5$. Concerning the semicrystalline fraction, we trace the peculiar bimodal shape of the A-CEF elution peak to the presence of chains in which the longest hard block had $BL_h = \underline{EL}$ (that were eluted at the $T_{el(max)}$ corresponding to the absolute peak maximum), or $BL_h = 2\underline{EL}$ (eluted at the $T_{el(max)}$ corresponding to the shoulder at the higher temperature side of the peak); the position of said shoulder is consistent with the correlation plot of Figure 6.14. Simulation models in the literature are in line with this interpretation.[40]

6.4.   Concluding remarks

The scope and objectives of HTE[41] as applied to polyolefin catalysis have been changing with time. Initially introduced for catalyst discovery purposes[42] with remarkable results (among which CAT-2 is an outstanding example[19]), later on HTE tools and methods proved to be ideally suited to screen complex catalyst formulations for desired applications.[43–46] The one of interest here is an exemplary case history[9]: its identification at Dow Chemical as one of the rare cases enabling ethene/1-octene CSC was like finding a needle in the haystack (as a matter of fact, decades of previous searches with conventional methods failed[10]).

In the present investigation, we made use of HTE with yet another purpose, that is the rapid semi-quantitative exploration of the variable space for a complex catalytic process, so as to highlight its molecular kinetics and mechanistic features.

We gave experimental evidence that the molecular architecture of statistical ethene/1-hexene OBCs produced by CSC is governed by the relative probabilities of 'self-shuttling' and 'cross-shuttling'. We concluded in particular that, with the original catalyst formulation disclosed in ref [9], OBCs featuring long hard blocks and an excess of soft blocks (which are those with the most desirable application properties[4,8–10,23–25]) are necessarily characterized by a pronounced inter-chain disuniformity.[26,27,39,40] As a matter of fact, the excess of CAT-2 over CAT-1 and the rather low $[Zn]/[^tM]$ ratio required for the purpose result in the formation of a comparatively large amount of random copolymer chains which underwent exclusively 'self-shuttling' events at CAT-2, and therefore consist of only one soft block.

We are fully aware that running CSC in HTE semibatch mini-reactors is a very delicate and difficult exercise, and therefore our results can only be regarded as semi-quantitative. This notwithstanding, we were able to closely reproduce the features of commercial Infuse™ OBCs,[4] as the aCEF profile overlay in Figure 6.15 and a comparative examination of the results in Tables 6.1 and 6.3 suggest.
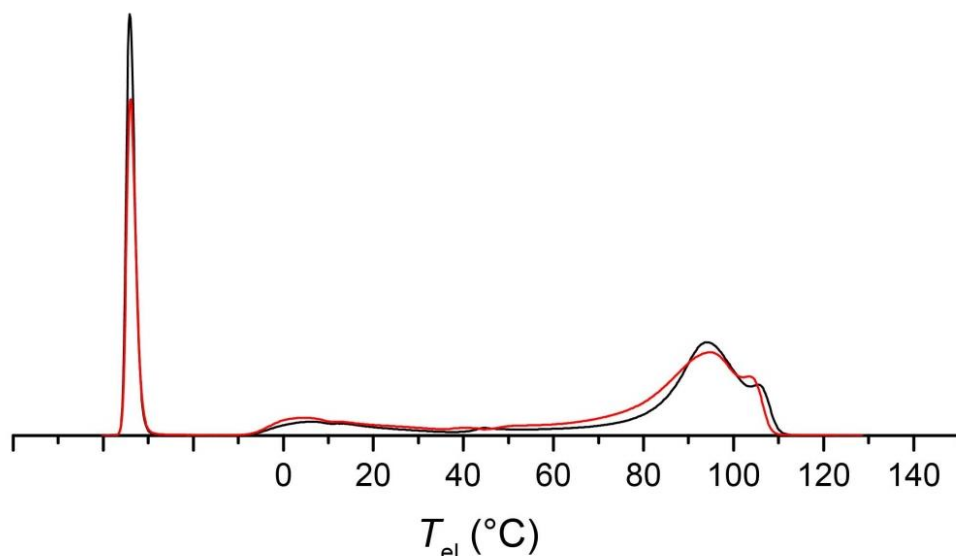
Figure 6.15. Overlay of the aCEF profiles of a commercial Infuse™ sample (Grade 9107; black trace) and the OBC sample at entry 13 of Table 6.3 (red trace).

The fundamental understanding provided by the present study can be useful for further product development. Using homologues of CAT-1 with a lower propensity to β-H elimination is a first obvious improvement, that indeed has already been reported in more recent Dow Chemical papers.[22] Homologues of CAT-2 with a higher activity compared with their counterpart in the catalyst pair, in turn, would help reducing inter-chain disuniformity, if desired.

On the other hand, we believe that the HTE strategy introduced in this investigation can find wider application, and has the potential to become a paradigm for elucidating other complex catalytic processes and products where drawing mechanistic conclusions can be completely nontrivial without a properly designed, robust experimental database.

References

(1)   *Tailor-Made Polymers*; Severn, J. R., Chadwick, J. C., Eds.; Wiley-VCH Verlag GmbH & Co. KGaA: Weinheim, Germany, 2008.

(2)   Coates, G. W. Precise Control of Polyolefin Stereochemistry Using Single-Site Metal Catalysts. *Chem. Rev.* **2000**, *100* (4), 1223–1252.

(3)   Resconi, L.; Cavallo, L.; Fait, A.; Piemontesi, F. Selectivity in Propene Polymerization with Metallocene Catalysts. *Chem. Rev.* **2000**, *100* (4), 1253–1346.

(4)   Chum, P. S.; Swogger, K. W. Olefin Polymer Technologies-History and Recent Progress at The Dow Chemical Company. *Prog. Polym. Sci.* **2008**, *33* (8), 797–819.

(5)   Hsieh, H. L.; Quirk, R. P. *Anionic Polymerization : Principles and Practical Applications*; Marcel Dekker: New York, 1996.

(6)   Matyjaszewski, K. *Cationic Polymerizations: Mechanisms, Synthesis, and Applications*; Marcel Dekker: New York, 1996.

(7)   Coates, G. W.; Hustad, P. D.; Reinartz, S. Catalysts for the Living Insertion Polymerization of Alkenes: Access to New Polyolefin Architectures Using Ziegler–Natta Chemistry. *Angew. Chemie Int. Ed.* **2002**, *41* (13), 2236–2257.

(8)   Hustad, P. D. Frontiers in Olefin Polymerization: Reinventing the World's Most Common Synthetic Polymers. *Science (80-.).* **2009**, *325* (5941), 704–707.

(9)   Arriola, D. J.; Carnahan, E. M.; Hustad, P. D.; Kuhlman, R. L.; Wenzel, T. T. Catalytic Production of Olefin Block Copolymers via Chain Shuttling Polymerization. *Science (80-.).* **2006**, *312*, 714–719.

(10)   Wenzel, T. T.; Arriola, D. J.; Carnahan, E. M.; Hustad, P. D.; Kuhlman, R. L. Chain Shuttling Catalysis and Olefin Block Copolymers (OBCs). In *Metal Catalysts in Olefin Polymerization*; Guan, Z., Ed.; Springer Berlin Heidelberg: Berlin, Heidelberg, 2009; pp 65–104.

(11)   Natta, G. Properties of Isotactic, Atactic, and Stereoblock Homopolymers, Random and Block Copolymers of α-Olefins. *J Polym Sci* **1959**, *34*, 531–549.

(12)   Busico, V.; Cipullo, R. Microstructure of Polypropylene. *Prog. Polym. Sci.* **2001**, *26* (3), 443–533.

(13)   Busico, V. Stereoblock Polypropylene. In *Stereoselective Polymerization with Single-Site Catalysts*; Baugh, L. S., Canich, J. A. M., Eds.; CRC Press: Boca Raton, Fla, 2008; pp 203–229.

(14)   Busico, V.; Cipullo, R.; Monaco, G.; Talarico, G.; Vacatello, M.; Chadwick, J. C.; Segre, A. L.; Sudmeijer, O. High-Resolution 13 C NMR Configurational Analysis of Polypropylene Made with MgCl$_2$-Supported Ziegler–Natta Catalysts. 1. The "Model" System MgCl$_2$/TiCl$_4$–2,6-Dimethylpyridine/Al(C$_2$H$_5$)$_3$. *Macromolecules* **1999**, *32* (13), 4173–4182.

(15)   Valente, A.; Mortreux, A.; Visseaux, M.; Zinck, P. Coordinative Chain Transfer Polymerization. *Chem. Rev.* **2013**, *113* (5), 3836–3857.

(16)   Kempe, R. How to Polymerize Ethylene in a Highly Controlled Fashion? *Chem. – A Eur. J.* **2007**, *13* (10), 2764–2773.

(17)   Hustad, P. D.; Kuhlman, R. L.; Carnahan, E. M.; Wenzel, T. T.; Arriola, D. J. An Exploration of the Effects of Reversibility in Chain Transfer to Metal in Olefin

Polymerization. *Macromolecules* **2008**, *41* (12), 4081–4089.

(18)   Makio, H.; Kashiwa, N.; Fujita, T. FI Catalysts: A New Family of High Performance Catalysts for Olefin Polymerization. *Adv. Synth. Catal.* **2002**, *344* (5), 477–493.

(19)   Boussie, T. R.; Diamond, G. M.; Goh, C.; Hall, K. A.; LaPointe, A. M.; Leclerc, M. K.; Murphy, V.; Shoemaker, J. A. W.; Turner, H.; Rosen, R. K.; et al. Nonconventional Catalysts for Isotactic Propene Polymerization in Solution Developed by Using High-Throughput-Screening Technologies. *Angew. Chemie Int. Ed.* **2006**, *45* (20), 3278–3283.

(20)   Froese, R. D. J.; Hustad, P. D.; Kuhlman, R. L.; Wenzel, T. T. Mechanism of Activation of a Hafnium Pyridyl–Amide Olefin Polymerization Catalyst: Ligand Modification by Monomer. *J Am Chem Soc* **2007**, *129* (25), 7831–7840.

(21)   Busico, V.; Cipullo, R.; Pellecchia, R.; Rongo, L.; Talarico, G.; Macchioni, A.; Zuccaccia, C.; Froese, R. D. J.; Hustad, P. D. "Uni et Trini": In Situ Diversification of (Pyridylamide)Hafnium(IV) Catalysts. *Macromolecules* **2009**, *42* (13), 4369–4373.

(22)   Kuhlman, R. L.; Klosin, J. Tuning Block Compositions of Polyethylene Multi-Block Copolymers by Catalyst Selection. *Macromolecules* **2010**, *43* (19), 7903–7904.

(23)   Liu, G.; Guan, Y.; Wen, T.; Wang, X.; Zhang, X.; Wang, D.; Li, X.; Loos, J.; Chen, H.; Walton, K.; et al. Effect of Mesophase Separation and Crystallization on the Elastomeric Behavior of Olefin Multi-Block Copolymers. *Polymer (Guildf).* **2011**, *52* (22), 5221–5230.

(24)   Park, H. E.; Dealy, J. M.; Marchand, G. R.; Wang, J.; Li, S.; Register, R. A. Rheology and Structure of Molten, Olefin Multiblock Copolymers. *Macromolecules* **2010**, *43* (16), 6789–6799.

(25)   Li, S.; Register, R. A.; Weinhold, J. D.; Landes, B. G. Melt and Solid-State Structures of Polydisperse Polyolefin Multiblock Copolymers. *Macromolecules* **2012**, *45* (14), 5773–5781.

(26)   Shan, C. L. P.; Hazlitt, L. G. Block Index for Characterizing Olefin Block Copolymers. *Macromol. Symp.* **2007**, *257*, 80–93.

(27)   Zhou, Z.; Miller, M. D.; Lee, D.; Cong, R.; Klinker, C.; Huang, T.; Li Pi Shan, C.; Winniford, B.; Degroot, A. W.; Fan, L.; et al. NMR Study of the Separation Mechanism of Polyethylene-Octene Block Copolymer by HT-LC with Graphite. *Macromolecules* **2015**, *48* (20), 7727–7732.

(28)   Vittoria, A.; Busico, V.; Cannavacciuolo, F. D.; Cipullo, R. Molecular Kinetic Study of "Chain Shuttling" Olefin Copolymerization. *ACS Catal.* **2018**, *8* (6), 5051–5061.

(29)   Frazier, K. A.; Boone, H. W.; Vosejpka, P. C.; Stevens, J. C. High Activity Olefin Polymerization Catalyst and Process. US2004/0220050 A1.

(30)   Arriola, D. J.; Carnahan, E. M.; Cheung, Y. W.; Devore, D. D.; Graf, D. D.; Hustad, P. D.; Kuhlman, R. L.; Li Pi Shan, C.; Roof, G. R.; Stevens, J. C.; et al. Catalyst Composition Comprising Shuttling Agent for Ethylene Multi-Block Copolymer Formation. WO2005/090427 A2.

(31)   Randall, J. C. A Review Of High Resolution Liquid [13]Carbon Nuclear Magnetic Resonance Characterizations Of Ethylene-Based Polymers. *J. Macromol.*

Sci. Part C **1989**, *29* (2–3), 201–317.

(32)   Liu, W.; Rinaldi, P. L.; McIntosh, L. H.; Quirk, R. P. Poly(Ethylene-Co-1-Octene) Characterization by High-Temperature Multidimensional NMR at 750 MHz. *Macromolecules* **2001**, *34* (14), 4757–4767.

(33)   Tong, Z. Z.; Huang, J.; Zhou, B.; Xu, J. T.; Fan, Z. Q. Chain Microstructure, Crystallization, and Morphology of Olefinic Blocky Copolymers. *Macromol. Chem. Phys.* **2013**, *214* (5), 605–616.

(34)   Kuhlman, R. L.; Wenzel, T. T. Investigations of Chain Shuttling Olefin Polymerization Using Deuterium Labeling. *Macromolecules* **2008**, *41* (12), 4090–4094.

(35)   Alfano, F.; Boone, H. W.; Busico, V.; Cipullo, R.; Stevens, J. C. Polypropylene "Chain Shuttling" at Enantiomorphous and Enantiopure Catalytic Species: Direct and Quantitative Evidence from Polymer Microstructure. *Macromolecules* **2007**, *40* (22), 7736–7738.

(36)   Cueny, E. S.; Johnson, H. C.; Anding, B. J.; Landis, C. R. Mechanistic Studies of Hafnium-Pyridyl Amido-Catalyzed 1-Octene Polymerization and Chain Transfer Using Quench-Labeling Methods. *J Am Chem Soc* **2017**, *139* (34), 11903–11912.

(37)   Cipullo, R.; Mellino, S.; Busico, V. Identification and Count of the Active Sites in Olefin Polymerization Catalysis by Oxygen Quench. *Macromol. Chem. Phys.* **2014**, *215* (18), 1728–1734.

(38)   Maury, J.; Feray, L.; Bazin, S.; Clément, J.-L.; Marque, S. R. A.; Siri, D.; Bertrand, M. P. Spin-Trapping Evidence for the Formation of Alkyl, Alkoxyl, and Alkylperoxyl Radicals in the Reactions of Dialkylzincs with Oxygen. *Chem. – A Eur. J.* **2011**, *17* (5), 1586–1595.

(39)   Tongtummachat, T.; Anantawaraskul, S.; Soares, J. B. P. Understanding the Formation of Linear Olefin Block Copolymers with Dynamic Monte Carlo Simulation. *Macromol. React. Eng.* **2016**, *10* (6), 535–550.

(40)   Anantawaraskul, S.; Sottesakul, S.; Siriwongsarn, E.; Soares, J. B. P. Chemical Composition Distribution and Temperature Rising Elution Fractionation of Linear Olefin Block Copolymers. *Macromol. Symp.* **2013**, *330* (1), 123–131.

(41)   *High-Throughput Screening in Heterogeneous Catalysis*; Hagmeyer, A., Strasser, P., Volpe, A. F., Eds.; Wiley-VCH Verlag GmbH & Co. KGaA: Weinheim, FRG, 2004.

(42)   Boussie, T. R.; Diamond, G. M.; Goh, C.; Hall, K. A.; LaPointe, A. M.; Leclerc, M.; Lund, C.; Murphy, V.; Shoemaker, J. A. W.; Tracht, U.; et al. A Fully Integrated High-Throughput Screening Methodology for the Discovery of New Polyolefin Catalysts: Discovery of a New Class of High Temperature Single-Site Group (IV) Copolymerization Catalysts. *J. Am. Chem. Soc.* **2003**, *125* (14), 4306–4317.

(43)   Busico, V.; Cipullo, R.; Mingione, A.; Rongo, L. Accelerating the Research Approach to Ziegler–Natta Catalysts. *Ind. Eng. Chem. Res.* **2016**, *55* (10), 2686–2695.

(44)   Busico, V.; Pellecchia, R.; Cutillo, F.; Cipullo, R. High-Throughput Screening in Olefinpolymerization Catalysis: From Serendipitous Discovery towards Rational Understanding. *Macromol. Rapid Commun.* **2009**, *30* (20), 1697–1708.

(45)   Vittoria, A.; Meppelder, A.; Friederichs, N.; Busico, V.; Cipullo, R.

Demystifying Ziegler-Natta Catalysts: The Origin of Stereoselectivity. *ACS Catal.* **2017**, *7* (7), 4509–4518.

(46)   Peil, K. P.; Neithamer, D. R.; Patrick, D. W.; Wilson, B. E.; Tucker, C. J. Applications of High Throughput Research at the Dow Chemical Company. *Macromol. Rapid Commun.* **2004**, *25* (1), 119–126.

7. Concluding Remarks

Chemistry in general is not an exact science. Chemical catalysis, moreover, is a purely kinetic phenomenon. This means that discovering and even optimizing a catalyst for a desired application heavily relies on trial-and-error, and serendipitous advances are not rare.

In view of the above, this PhD project aimed to improve the effectiveness of a trial-and-error approach to olefin polymerization catalysis, one of the most important chemical technologies, by means of High Throughput Experimentation (HTE) methodologies. The project was hosted at the Laboratory of Stereoselective Polymerizations (LSP) of the Federico II University, which is world-leading in HTE catalyst screenings with optimization purposes, and sponsored by HTExplore srl, an academic spin-off of LSP delivering HTE services to polyolefin producers. The general aim was to introduce protocols for 'smart' applications of the existing HTE workflow of LSP to complex chemical problems in polyolefin catalysis. In particular, methods for the rapid and accurate determination of the Quantitative Structure-Activity Relationship (QSAR) of representative molecular or heterogeneous catalyst formulations were implemented as the basis for statistical modeling with predictive ability.

The HTE toolkit was the subject of Chapter 2. Due to the extensive miniaturization and robotic automation, a HTE platform is not a push-button setup, and a complete HTE workflow may include several platforms and a number of integrated analytical tools amenable to high-throughput operation, so as not to

create bottlenecks. At several industrial laboratories throughput was admittedly traded for accuracy, and a comparatively coarse HTE screening is still followed by finer evaluations with conventional methods in larger scale. At LSP the choice was different, and major efforts were undertaken in order to bring the HTE workflow to the precision and accuracy of conventional tools, for the polymerization part as well as at the polymer characterization stage. The ultimate goal is simplify the approach to catalysis research by removing the intermediate conventional large scale QSAR determination step between the HTE exploration upstream and (pre-)pilot optimization downstream (Figure 7.1). That this is possible was demonstrated by the benchmarking studies reported in the same Chapter 2.
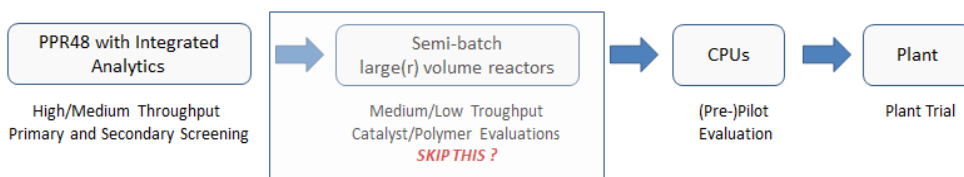
Figure 7.1. Catalyst research and optimization workflow according to LSP.

Chapters 3 and 4 illustrate the aforementioned approach to what is probably the most complicated and challenging problem in polyolefin catalysis, that is the discovery and optimization of heterogeneous Ziegler-Natta (ZN) systems for the industrial production of isotactic polypropylene (i-PP). These systems are complex formulations which include a nanostructured $MgCl_2$ support, a Ti precursor compound (typically $TiCl_4$), one or more organic electron donors as selective surface stabilizers and modifiers, and an Al-alkyl compound as an activator and scavenger. Huge research efforts have been spent in order to identify and tailor novel formulations, which is not surprising if one considers that i-PP is now the 2nd largest volume polymer on the global market, with an installed capacity of over 60 million tons per year. Yet, innovation in the field was rather slow (a new catalyst generation every 10 years on average), because the inner workings of these catalysts are elusive. The quest for novel formulations has recently become more acute, because the most widely used systems in industry containing phthalates as surface modifiers have been threatened by a recent

REACH ban for toxicity concerns, and even though said concerns likely are not justified the market calls for phthalate-free solutions.

In this project, two original and proprietary HTE workflows have been implemented and utilized to screen ZN PP systems in propene polymerization, and follow the evolution of catalyst composition with time upon activation and use. QSAR databases of unprecedented size and accuracy have been built with focus on polymer stereoselectivity (Chapter 3) and regioselectivity (Chapter 4). The overall results highlighted the basic principles governing the behavior of the multiple classes of ZN catalytic species, led to a refinement of qualitative 'clear-box' QSAR models, and opened the door to quantitative 'black-box' QSAR models with predictive ability. The investigation was part of a collaborative effort with SABIC (in particular, 'black-box' QSAR modeling was out of the scope of the thesis).

Compared with ZN systems, molecular olefin polymerization catalysts have the reputation to be easier to investigate and customize. There is some truth in that, because the precursor molecules are better-defined and amenable to targeted modifications. On the other hand, ligand synthesis and metalation can be extremely difficult to pursue, and the highly electrophilic character of the active cations can trigger a variety of undesired side reactions. Metallocene catalysts have been the first molecular catalysts to show the ability to mediate the stereoselective polymerization of propene in homogeneous phase, and industry has invested many billions of dollars (a conservative estimate is in the range of 30 to 50 between 1985 and 2000) to identify structures able to challenge ZN catalysts for the industrial production of i-PP. Success has been limited though, because the outstanding cost-to-performance balance of ZN systems has not even been approached. In recent times, the opinion has spread in the scientific community that there is no scope for further explorations of catalyst space, in particular for the intensively scouted C_2-symmetric Group 4 *ansa*-metallocenes. It is important to note, however, that HTE was only marginally exploited in these searches, because parallel routes for the synthesis of metallocene precursors have not been available for a long time.

The scenario has changed for the better only in recent years. In the framework of a research project sponsored by the Dutch Polymer Institute (DPI) and involving a collaboration between LSP and the group of Prof. Alexander Voskoboynikov at Moscow State University (pioneer of parallel metallocene synthesis), the potential of HTE in metallocene catalysts is being thoroughly assessed. The present PhD

project contributed to the endeavor by implementing and applying screening protocols for Group 4 *ansa*-metallocenes in isotactic-selective propene polymerizations. Chapter 5 reports how a feed-back loop connecting precatalyst synthesis and catalyst testing, aided by a 'white-box' model analyzing the QSAR, led to the rapid identification of several C_2-symmetric bis-(1-Indenyl) *ansa*-zirconocenes with improved performance compared to the champions in the field. In our opinion, this is a striking demonstration of the ability of HTE to navigate the catalyst variables hyperspace and discover new promising territories.

Last but not least, Chapter 6 highlights one more important utilization of HTE, that is the rapid generation of accurate and reliable experimental data for molecular kinetic investigations of complex olefin polymerization processes. The chosen case history was the synthesis of olefin block copolymers (OBCs) by means of tandem catalysis under coordinative chain transfer polymerization (CCTP) regime. This process, disclosed by Dow Chemical in 2006 and commonly known as 'Chain Shuttling', is a real break-through, as it represents the first commercially viable process to produce thermoplastic elastomers with HDPE and LLDPE blocks (Infuse™) that escape the paradigmatic correlation between density and melting temperature of LLDPE. Dow Chemical was the first to introduce HTE tools and methods in polyolefin R&D, and the discovery of Chain Shuttling was entirely HTE-based. On the other hand, the details of Infuse™ OBC microstructure and architecture have remained unknown for over 10 years past the discovery, likely because the catalytic process for their synthesis is too technically demanding for reliable investigations in an academic environment.

In the present project, a 'smart' protocol for the molecular kinetic exploration of Chain Shuttling reactions by means of the HTE workflow of LSP has been implemented and applied to the catalyst system and under the process conditions declared by Dow Chemical. In a very short time, a database of kinetic data was assembled and used to sort out the mechanistic details of the system, ending up with the first reliable estimates of average block numbers and lengths, and distributions thereof, for Infuse™-type OBC materials.

We are confident that the present thesis demonstrates that innovation in chemistry is not over even in areas that are considered mature, like e.g. catalytic olefin polymerization. Many chemical problems, including long standing ones, can rapidly find a solution as soon as adequate information becomes available. This simple and – in a way – trivial concept is often overlooked because the actual complexity of chemical systems tends to be under-estimated. Just as an example,

an adequate QSAR database for ZN catalyst optimization (Chapters 3 and 4) requires to run a few hundred polymerization experiments under rigorously controlled conditions. With conventional methods these can take months, and involve various human operators that may randomly introduce irreproducibility or flaws. With the LSP HTE workflow and proper operating protocols, some weeks were enough.

In our opinion, HTE tools and methods represent a breakthrough in chemical research, and can foster innovation in all areas of chemistry, including seemingly exhausted ones (see e.g. Chapter 5). The growing complexity of advanced materials for post-industrial societies will make processes like that illustrated in Chapter 6 more frequent. We firmly believe that the real question is not whether HTE should be used, but how the HTE approach can be extended further along the entire knowledge and value chains of the chemical industry (see e.g. the problem discussed in the Appendix to this thesis).

Appendix – A new method for active site counts in Ziegler Natta catalysis

A.1 Introduction

In Chapter 1 we have discussed why the fraction of active metal in any organometallic coordination catalyst is very likely to be lower than unity. This is particularly true with heterogeneous catalysts, and ZN PP systems are an exemplary case also in this respect.

Measuring how much of the Ti is involved in chain growth is experimentally difficult, and also – to some extent – a matter of definition and time scale, because the question of 'dormant' sites need to be tackled. We will consider this at a later stage.

Two basic approaches to active site counts in ZN catalysis have been proposed. One has been defined as 'Quench-Labeling' (QL), and consists in the introduction of a well-recognizable label at the end of the growing chains by means of a reaction that quenches further chain growth. Typical labels are strong poisons such as ^{14}CO,[1,2] ^{13}CO,[3] CH_3O^3H,[4,5] (functional) alkyne (e.g. Figure A1-a),[6] or other functional molecules bearing a UV chromophore or a fluorescent fragment (e.g. Figure A1-b,c,d).[7]
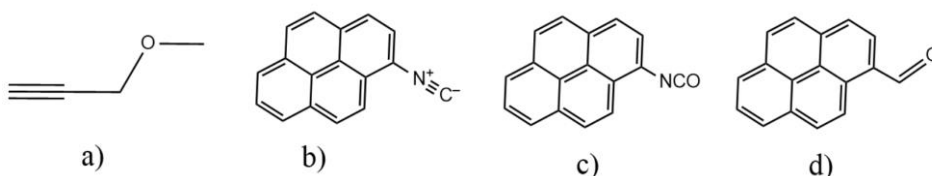
Figure A.1. New generations of quench-labeling agents: a) propargyl ether, b) pyrene-isonitrile, c) pyrene-isocyanate, d) pyrene-aldehyde.

The use of radioactive QL agents such as ^{14}CO and CH_3O^3H has been popular until the 1970s,[8] that is when spectroscopic detection methods were still rather

primitive and safety concerns were less stringent. From the mechanistic standpoint, the main limitation of the approach is that its chemistry is 'blind', and it is not possible to rule out the hypothesis that the poison reacted with both growing Ti-Polymeryls and 'dead' Al-Polymeryls formed by trans-alkylation with the Al-alkyl cocatalyst; indeed, the method requires a complicated and somehow questionable extrapolation of the measurements to [Al]→0.[8] Moreover, a recent NMR QL study of *ansa*-zirconocene catalysts using [13]CO demonstrated that multiple CO insertions into growing Zr-Polyethylenyl bonds with the formation of alternated $-(CH_2)_2-CO)_n-$ segments can occur;[9] whether this is the case with ZN catalytic species remains to be seen. Typical QL estimates of the active Ti in ZN catalyst systems are around 10-20%,[5,8,10] but in view of the above remarks it is well-possible that they represent over-estimations.

The second approach is based on 'Quenched-Flow' (QF) techniques. The elegant and simple idea, introduced by Keii et al.[11,12] (who referred to their method as 'Stopped-Flow') is to operate at the very early stages of the polymerization process, when chain growth is still within the 'controlled' kinetic regime (that is before chain transfer processes become appreciable). Under this regime the following equations, originally derived by Natta[2], hold:

$$Y = R_p t = \langle k_p \rangle x^* [\text{Ti}][C_n H_{2n}] t \qquad \text{(EqA.1)}$$

$$\frac{1}{P_n} = \frac{\langle f_{tr} \rangle}{\left(\langle k_p \rangle [C_n H_{2n}] \right)} + \frac{1}{\left(\langle k_p \rangle [C_n H_{2n}] \right)} \cdot \frac{1}{t} \qquad \text{(EqA.2)}$$

where R_p is average catalyst productivity; $\langle k_p \rangle$ is the average specific rate of polymerization; $\langle f_{tr} \rangle$ is the average (cumulative) frequency of chain transfer; $[C_n H_{2n}]$ is monomer concentration (a 1st-order kinetics is assumed); [Ti] is the analytical 'concentration' of Ti in the catalyst slurry; x^* is the active fraction of Ti; t is polymerization time; P_n is the number-average degree of polymerization. Measurements of $P_n = f(t)$ give access to x^*, $\langle k_p \rangle$ and $\langle f_{tr} \rangle$ by interpolating the experimental data points in terms of EqsA.1, A.2. A technical drawback of the QF approach is that it requires to operate at reaction times of the order of the average chain growth time; for competent ZN catalysts, even under mild conditions this is < 1s. Moreover, a conceptual question is whether or not the kinetic information collected at such an early stage of a heterogeneous process is representative of the behavior of the system at later stages, when particle

fragmentation has occurred (typical residence times of ZN catalyst particles in industrial reactors are a few hours).

Almost invariably, QF studies concluded that $x^* < 5\%$.[11–15] In particular, a recent study on propene polymerization in the presence of catalyst system **C1**-TEA/**ED5** (coding from Chapter 3) in heptane slurry at 40°C ended up with the results of Table A.1.[16]

Table A.1 Best-fit values of the kinetic parameters for QF propene polymerization experiments in the presence of catalyst system **C1**-TEA/**ED5** at 40°C in heptane slurry.[16]

ID/ED	$<k_p>$ [s^{-1} M^{-1}]	x^* (%)	$\langle f_{tr} \rangle$ [s^{-1}]
DBP/DIBDMS	$(9.4\pm0.9) \times 10^3$	0.21 ± 0.02	6 ± 1

In the last few years, the QL approach has been re-visited by introducing 'smart' labels, at least some of which are claimed *not* to react with 'dead' Al-polymeryls and can be reliably quantified by means of modern spectroscopic methods.

One such label is the propargyl ether of Figure A1-a[6]. Group 4 M-R species are known to insert alkynes with a Cossee-type mechanism without further propagation;[17,18] the foreseeable back-biting of the ether moiety should further inhibit monomer insertion until system workup with a Brønsted acid. The unsaturated chain ends can be detected and quantified by means of ^{1}H/^{13}C NMR spectroscopy.[6]

A number of UV-Vis labels (Figure A1-b,c,d) have been recently proposed by Prof. Clark Landis.[7,19] The advantage of Landis' 'Chromophore Quench-Labeling' (CQL) is that a UV-Vis detector can be installed on a GPC setup in addition to the standard one(s) (e.g. IR, RI, or LS), and therefore it is possible to obtain two GPC curves from a CQL experiment: one corresponding to the overall MWD (i.e., the untagged polymer chains), another referring exclusively to the MWD of the tagged chains. The comparison between the two curves is very informative; in particular, in case the two MWDs coincide one can rule out the hypothesis that the label reacted selectively with only part of the growing chains.

In Landis' group, CQL has only been applied to molecular olefin polymerization catalysts[7,19,20] (e.g., the (pyridylamido)Hf species discussed in Chapter 6 of this thesis). Prof. Landis has graciously agreed to host A.V. in his research group at the

University of Wisconsin at Madison (USA) for a three-month internship, with the aim to try the CQL approach for the first time in ZN catalysis. The results are presented in the following sections of this Appendix to the PhD Thesis.

A.2 Chromophore Quench-Labeling of ZN Catalysts

The ZN catalyst system selected for this study was **C1**-TEA (Chapter 3). 1-Hexene was used as the monomer (instead of propene), mainly because the available UV-GPC setup in Landis' group operates at 40°C with THF as the eluent, and an amorphous polymer is necessary. Isotactic polyhexene (PH) melts below RT, and therefore matches the requirement.

The chosen CQL agent was the pyrene-isonitrile (PyrNC) shown in Figure A.1-b. Its quenching ability was tested by running a series of experiments at variable [PyrNC]/[Ti] mol ratio (Figure A.2). The results indicated that at [PyrNC]/[Ti] ≥ 6 the polymerization is effectively shut down.
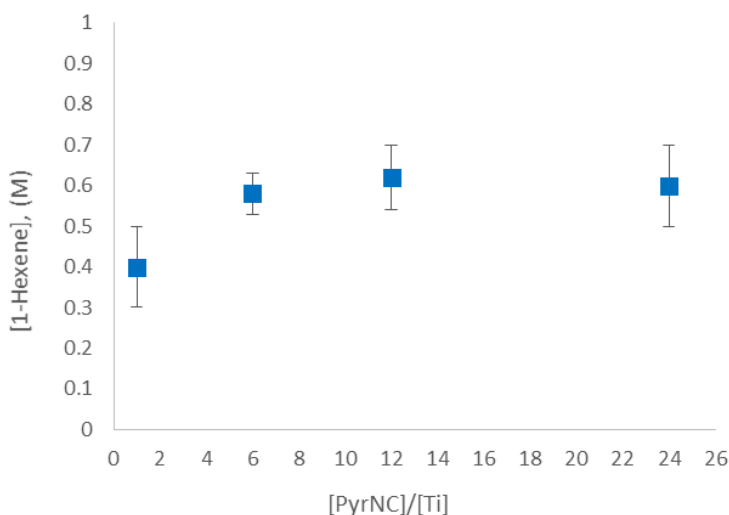
Figure A.2. Monomer conversion as a function of quencher loading for CQL 1-hexene polymerization experiments at 40°C and 90 s quenching time ([1-hexene]$_0$ = 1.0 M, [Ti]$_0$ = 1.04 mM, [Al]/[Ti] = 30, pre-activation time = 5 min).

Above said threshold, quantitative integration of the UV-Vis signal of the quench-labeled polymer by UV-GPC yielded x^* values in the range of 0.4-0.7%, independently of the actual [PyrNC]/[Ti] value (Figure A.3).

The MWD of the labeled polymer is rather 'noisy' because the average MW is high and the label is highly diluted. Yet, Figure A.4 shows that the GPC curves of the untagged and tagged polymer are very similar, which indicates that the method is

sound, and suggests that the label is able to react with the 'dormant' sites with a 2,1 last-inserted monomeric unit (Chapter 4). The latter conclusion is consistent with previous CQL studies on molecular catalysts.[21]
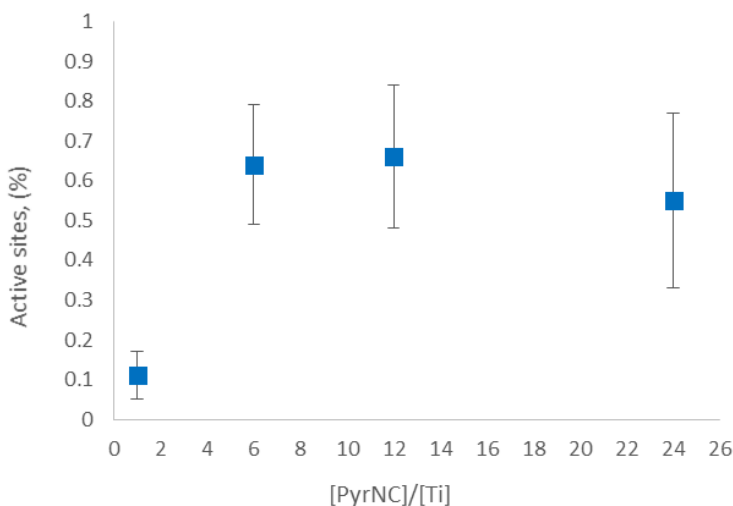

Figure A.3. Values of x^* measured by UV-GPC as a function of [PyrNC]/[Ti] for CQL 1-hexene polymerization experiments at 40°C and 90 s quenching time ([1-hexene]$_0$ = 1.0 M, [Ti]$_0$ = 1.04 mM, [Al]/[Ti] = 30, pre-activation time = 5 min).
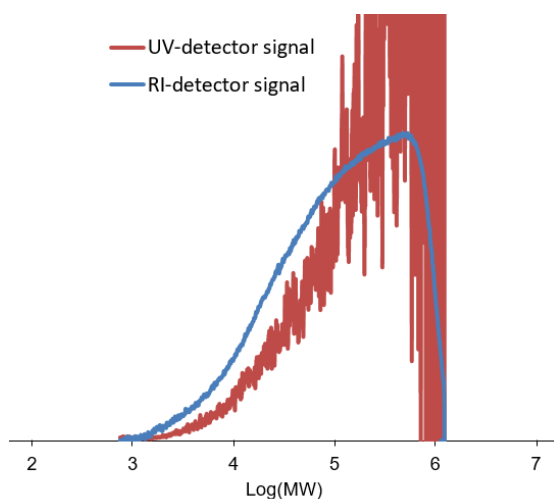
Figure A.4. Representative molecular weight distribution (MWD) curve obtained on a labeled polyhexene sample showing the contribution coming from the total polymer mass (RI signal) and from its quench-labeled fraction UV-detected.

After this verification, a series of experiments at variable quenching time was performed in order to follow the time evolution of x^*. Monomer conversion (Figure A.5) was well-reproduced assuming a first-order polymerization rate with respect to the monomer (dashed line through the data points), which is in line with most of the literature. All polymer samples were characterized by means of UV-GPC, with the results of Table A.2.

Table A.2. Main results of the CQL 1-hexene polymerizations experiments of Figure A.5.

t (s)	Y (mg)	M_n (kDa)	M_w (kDa)	PDI	x^* (%)
10	13	73	411	5.6	0.68
20	22	119	469	3.9	0.36
30	28	68	419	6.2	0.42
45	29	70	390	5.6	0.48
60	37	67	384	5.7	0.52
90	42	49	341	7.0	0.55
120	46	47	346	7.4	0.52
300	56	28	265	9.5	0.52
600	72	19	222	11.7	0.44
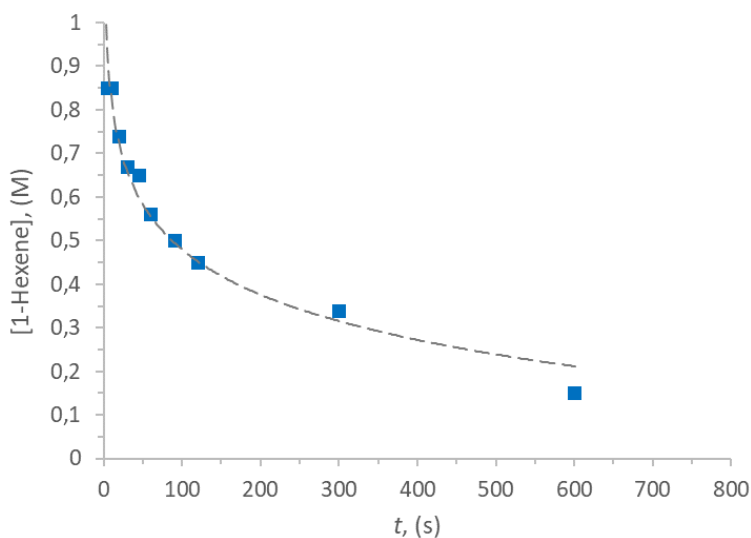
Figure A.5. Monomer conversion *vs* reaction time for CQL 1-hexene polymerization experiments at 40°C ([1-hexene]$_0$ = 1.0 M, [Ti]$_0$ = 0.84 mM, [Al]/[Ti] = 30, pre-activation time = 5 min, [PyrNC]/[Ti] = 6.0).

The value of x^* turned out to be time-independent and constant at $(0.49\pm0.09)\%$ in the explored range. Importantly, the finding of $x^* < 1\%$ agrees well with the latest QF estimates for a closely related catalyst system. The slight decrease of average polymer MW with time can be ascribed to slow, monomer-independent chain transfer process(es), such as e.g. trans-alkylation by TEA. From the experimental rate of polymerization at $t\to0$ and the average value of x^* the average values of $\langle k_p \rangle$ and $\langle f_{tr} \rangle$ were calculated (Table A.3). Said values are moderately lower than the corresponding ones for QF propene polymerization experiments with the same catalyst system under very similar conditions[16] (Table A.1), which is plausible in view of the different steric demand of the two monomers. To the best of our knowledge, this is the first comparative kinetic study of a ZN PP catalyst system with a QF and a CQL approach; in our opinion, the agreement is truly remarkable.

Table A.3. Average values of the kinetic parameters for the CQL experiments of Figure A3.

$\langle k_p \rangle$ [s^{-1} M^{-1}]	$\langle f_{tr} \rangle$ [s^{-1}]
2.0×10^3	2.5

A.3   Concluding remarks

Finding that the fraction of active transition metal (x^*) in a heterogeneous coordination catalyst is well below unity is neither unusual nor surprising. On the other hand, the CQL measurements of the previous section, ending up with a value of x^* <1% for an industrial ZN PP catalyst system, highlighted an admittedly extreme case. The agreement with previous independent QF estimates suggests that the results are not flawed; therefore, a mechanistic interpretation is desirable.

It has long been suspected that the QF approach under-estimates x^* because in the very short experiment times (few s) typical of the method the catalyst particles cannot undergo fragmentation and therefore part of the Ti is not accessible to the monomer. This however cannot be the case for the present CQL study, with longer experiment times (up to 10 min) and polymer yields up to ≈50 g g(catalyst)$^{-1}$ at which some fragmentation does occur. Moreover, the precatalyst activation studies described in Chapter 3 demonstrated that without producing polymer and therefore causing any fragmentation the entire catalyst surface is accessible to TEA in less than 10 min.

Our interpretation is that x^* measured by QF or CQL corresponds to the fraction of Ti bearing a polymeryl (either growing or 'dormant' due to a last-inserted 2,1 monomeric unit) at any given moment. What escapes the count instead are the Ti species with Ti-R (e.g. R = Et) and Ti-H bonds, which are less sterically crowded and can form rather stable adducts with $AlR_{3-x}Cl_x$ species and/or co-adsorbed donors. Examples of the former case can be found in Figure A.6.[22] For a model of the second case see e.g. Figure 3.7 of Chapter 3.

All such adducts can ultimately change into active sites as soon they open up, thus liberating the coordination site necessary for the π-coordination of the monomer. The process is highly endergonic, and the steady-state fraction of adducts x_{add} can be expected to be (much) larger than x^*. Indeed, a recent high-resolution EPR investigation of catalyst **C1** after activation with $AlMe_3$ vapor ended up with $x_{add} \approx$ 10%.[23]
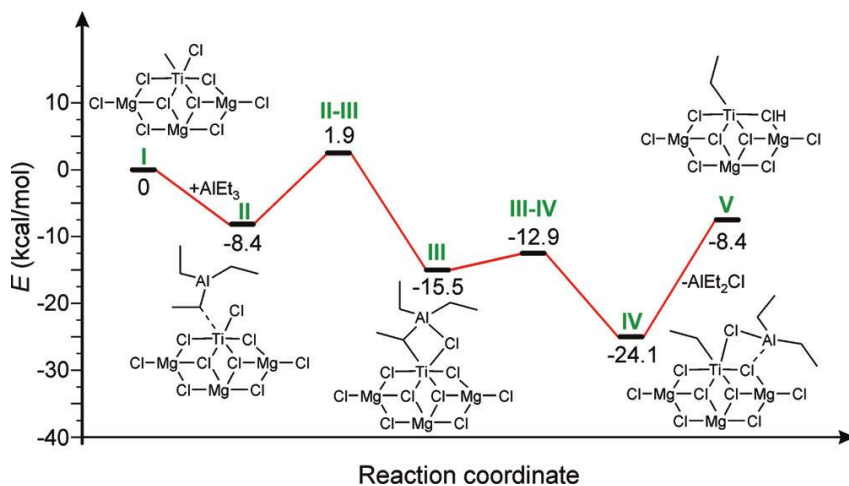
Figure A.6. Models of adducts between adsorbed Ti(III) and AlR$_{3-x}$Cl$_x$ species.[22]

From the methodological standpoint, an important and intriguing challenge is to implement CQL protocols usable with HTE platforms. As was already noted, labels b, c, d of Figure A.1 are fluorescent; hyphenating a fluorescence detector with a high-temperature Rapid-GPC may represent an effective solution, that will be explored in the near future.

A.4 Experimental part

All polymerizations were carried out under nitrogen atmosphere using a glove box. Toluene and 1-hexene were dried by passing through a column packed with commercially available Q-5 catalyst (13 % Cu(II) oxide on Al_2O_3), stored inside the glove box over silica and filtered before usage. The ZN precatalyst was kindly donated by SABIC and used as received. TEA was purchased and used as received. PyrNC was synthesized according to the literature.[24,25]

NMR spectra were recorded at 298 K using Bruker AV-400 MHz spectrometer fitted with a SmartProbe. Quantitative NMR spectra to measure 1-hexene monomer conversion were collected using a relaxation delay of 10 s.

GPC analyses were performed using a Viscotek GPCmax/VE 2001 instrument fitted with PolyPore columns (2×300×7.5 mm) featuring 5 μm particle size from Polymer Laboratories. Samples were eluted with THF at a flow rate of 1 mL/min at 40 °C. Polymers were characterized by differential refractive index (RI) and UV (λ 344 nm) detection using a Viscotek Model 302-050 Tetra Detector Array. Omnisec software (Viscotek, Inc.) was used for initial data processing such as positioning the baseline, setting limits, and applying the molecular weight calibration. Further processing was carried out using Microsoft Excel.

The 1-hexene polymerization protocol was as follows. In a 1 mL vial a solution of triethylaluminum (TEA) is prepared (100-150 mM). The polymerizations are carried out at 40°C in 1 mL vials, stirred with a magnet at 500 rpm, using the following order of addition: toluene solvent, TEA solution ([Al]/[Ti] = 30), catalyst suspension (1.25-5 mg of catalyst dispensed). The reaction-vial is kept under stirring at 40°C for the desired pre-activation time before the addition of 1-hexene (1.0 M, 125 μL) which starts the polymerization. At the desired reaction time, the polymerization is quenched by adding PyrNC ([PyrNC]/[Ti] = 6.0, 50mM solution in toluene). The mixture is allowed to react for at least 30 minutes.

Quenched solutions were first analyzed for monomer conversion; each vial was charged with a standard (40 μL of diphenylmethane solution in toluene, 0.69 M), and approximately 50 μL of the resulting solution was analyzed by ^{1}H NMR in $CDCl_3$. Next, reaction solutions including NMR aliquots were recollected and prepared for UV-GPC analysis. The reaction mixture was poured into an excess of MeOH to remove the excess of unreacted quenching label. After polymer

decantation, the supernatant was removed and one more MeOH washing cycle was performed. The polymers were then dissolved in THF (1.0 mg mL-1), filtered using disposable syringe filters with 0.2 μm pore size, and submitted to GPC analysis.

References

(1)   Natta, G. Kinetic Studies of α-Olefin Polymerzation. *J. Polym. Sci.* **1959**, *34* (127), 21–48.

(2)   Natta, G.; Pasquon, I. The Kinetics of the Stereospecific Polymerization of α-Olefins. *Adv Catal* **1959**, No. 11, 1–66.

(3)   Shiono, T.; Ohgizawa, M.; Soga, K. Reaction between Carbon Monoxide and and a Ti-Polyethylene Bond with a $MgCl_2$-Supported $TiCl_4$ Catalyst System. *Makromol. Chem* **1993**, *194*, 2075–2085.

(4)   Feldman, C. F.; Perry, E. Active Centers in the Polymerization of Ethylene Using Titatium Tetrachloride-Alkylaluminium Catalysts. *J Polym Sci* **1960**, *46* (147), 217–231.

(5)   Yaluma, A. K.; Tait, P. J. T.; Chadwick, J. C. Active Center Determinations on $MgCl_2$-Supported Fourth- and Fifth-Generation Ziegler-Natta Catalysts for Propylene Polymerization. *J. Polym. Sci. Part A Polym. Chem.* **2006**, *44* (5), 1635–1647.

(6)   Yu, Y. Alkynyl Ether Labeling: A Selective and Efficient Approach to Determine Active Sites Content of Olefin Polymerization Catalysts. In *6th International Conference on the Reaction Engeenering of Polyolefins (InCoREP)*; Geleen/Maastricht, Netherlands, 2017.

(7)   Nelsen, D. L.; Anding, B. J.; Sawicki, J. L.; Christianson, M. D.; Arriola, D. J.; Landis, C. R. Chromophore Quench-Labeling: An Approach to Quantifying Catalyst Speciation As Demonstrated for (EBI)ZrMe2/B(C_6F_5)$_3$-Catalyzed Polymerization of 1-Hexene. *ACS Catal.* **2016**, *6* (11), 7398–7408.

(8)   Mejzlik, J.; Lesna, M.; Kratochvila, J. Determination of the Number of Active-Centers in Ziegler-Natta Polymerization of Olefns. *Adv Polym Sci* **1986**, No. 81, 83–120.

(9)   Budzelaar, P. H. M. CO/Ethene Copolymerization at Zirconocene Centers? *Organometallics* **2004**, *23* (4), 855–860.

(10)   Yang, H.; Zhang, L.; Zang, D.; Fu, Z.; Fan, Z. Effects of Alkylaluminum as Cocatalyst on the Active Center Distribution of 1-Hexene Polymerization with $MgCl_2$-Supported Ziegler–Natta Catalysts. *Catal. Commun.* **2015**, *62*, 104–106.

(11)   Keii, T.; Terano, M.; Kimura, K.; Ishii, K. A Kinetic Argument for a Quasi-Living Polymerization of Propene with a Magnesium Chloride-Supported Catalyst. *Makromol. Chemie, Rapid Commun.* **1987**, *8* (11), 583–587.

(12)   Taniike, T.; Sano, S.; Ikeya, M.; Thang, V. Q.; Terano, M. Development of a Large-Scale Stopped-Flow System for Heterogeneous Olefin Polymerization Kinetics. *Macromol. React. Eng.* **2012**, *6* (6–7), 275–279.

(13)   Terano, M.; Kataoka, T. A Kinetic Study of Propene Polymerization Using Magnesium Chloride-Supported Catalysts. *Makromol. Chemie, Rapid Commun.* **1989**, *10* (2), 97–102.

(14)   Mori, H.; Iguchi, H.; Hasebe, K.; Terano, M. Kinetic Study of Isospecific Active Sites Formed by Various Alkylaluminiums on MgCl2-Supported Ziegler Catalyst at the Initial Stage of Propene Polymerization. *Macromol. Chem. Phys.* **1997**, *198* (4), 1249–1255.

(15)   Matsuoka, H.; Liu, B.; Nakatani, H.; Terano, M. Variation in the Isospecific Active Sites of Internal Donor-Free MgCl$_2$-Supported Ziegler Catalysts: Effect of External Electron Donors. *Macromol. Rapid Commun.* **2001**, *22* (5), 326–328.

(16)   Yu, Y.; Busico, V.; Budzelaar, P. H. M.; Vittoria, A.; Cipullo, R. Of Poisons and Antidotes in Polypropylene Catalysis. *Angew. Chemie Int. Ed.* **2016**, *55* (30), 8590–8594.

(17)   Eisch, J. J.; Piotrowski, A. M.; Brownstein, S. K.; Gabe, E. J.; Lee, F. L. Direct Observation of the Initial Insertion of an Unsaturated Hydrocarbon into the Titanium-Carbon Bond of the Soluble Ziegler Polymerization Catalyst, Cp$_2$TiCl$_2$-MeAlCl. *J. Am. Chem. Soc.* **1985**, *107* (24), 7219–7221.

(18)   Clarke, T. C.; Yannoni, C. S.; Katz, T. J. Mechanism of Ziegler-Natta Polymerization of Acetylene: A Nutation NMR Study. *J. Am. Chem. Soc.* **1983**, *105* (26), 7787–7789.

(19)   Cueny, E. S.; Johnson, H. C.; Anding, B. J.; Landis, C. R. Mechanistic Studies of Hafnium-Pyridyl Amido-Catalyzed 1-Octene Polymerization and Chain Transfer Using Quench-Labeling Methods. *J Am Chem Soc* **2017**, *139* (34), 11903–11912.

(20)   Cueny, E. S.; Johnson, H. C.; Landis, C. R. Selective Quench-Labeling of the Hafnium-Pyridyl Amido-Catalyzed Polymerization of 1-Octene in the Presence of Trialkyl-Aluminum Chain-Transfer Reagents. *ACS Catal.* **2018**, acscatal.8b03615.

(21)   Landis, C. R.; Cueny, E. S.; McDaniel, T. Personal Communication.

(22)   Bahri-Laleh, N.; Correa, A.; Mehdipour-Ataei, S.; Arabi, H.; Haghighi, M. N.; Zohuri, G.; Cavallo, L. Moving up and down the Titanium Oxidation State in Ziegler–Natta Catalysis. *Macromolecules* **2011**, *44* (4), 778–783.

(23)   Morra, E.; Giamello, E.; Van Doorslaer, S.; Antinucci, G.; D'Amore, M.; Busico, V.; Chiesa, M. Probing the Coordinative Unsaturation and Local Environment of Ti^{3+} Sites in an Activated High-Yield Ziegler–Natta Catalyst. *Angew. Chemie Int. Ed.* **2015**, *54* (16), 4857–4860.

(24)   Wang, X.; Wang, Q. G.; Luo, Q. L. Synthesis of Isonitriles from N-Substituted Formamides Using Triphenylphosphine and Iodine. *Synth.* **2015**, *47* (1), 49–54.

(25)   Wanzlick, H. W.; Lehmann-Horchler; M., Mohrmann, S.; Gritzky, R.; Heidepriem, H.; Pankow, B. New Methods in Preparative Organic Chemistry IV. *Angew. Chemie Int. Ed.* **1964**, *3* (6), 401–408.

Annex - PhD School Activity Summary

Candidate: Antonio Vittoria   **Supervisor:** Prof. Vincenzo Busico

1) **Attended Courses (6 minimum, 8 hours each):**

- *Techniques of Solid-Liquid Extraction Used in the Preparation of Samples for Chemical Analysis and Production of Extracts for Industrial Uses* (Prof. Daniele Naviglio, February-March 2016).

- *Structural Analysis of Materials at Nanometer Length Scale with Small Angle X-ray Scattering* (Prof. Finizia Auriemma, September and November 2016).

- *Chemical Reactors for Solid–Gas Processes Aimed at Energy Production* (Prof. Fabio Montagnaro, May 2017).

- *Selective Organometallic Catalysis: systems and advanced techiques* (Prof. Peter H.M. Budzelaar, May 2017).

- *Recombinant Production of Natural and Mutant Proteins* (Prof. Angela Duilio, March 2018).

- *Advanced Mass Spectrometry* (Prof. Piero Pucci, June 2018).

2) **Attended Seminars:**

Title	Speaker	Date	Place
Bioeconomy in the Circular Economy	Prof. Giovanni Sannia	29/01/2016	DSC-UniNa
Multimodal Approaches for Preclinical Molecular Imaging	Dr. Menichetti and Dr. Chiariello	05/02/2016	DSC-UniNa
Industria e ricerca nel settore biofarmaceutico: bisogni attuali e sviluppi futuri	Dr. Sara Carillo	25/02/2016	DSC-UniNa
The versatility of Mesoscopic Solar Cells	Prof. Anders Hagfeldt	14/04/2016	DSC-UniNa
EPDM: back to basics	Prof. Martin Van Duin	29/04/2016	DSC-UniNa
Supramolecular Chemistry of Chiral Calixarenes	Prof. Mauro Mocerino	13/01/2017	DSC-UniNa
La Chimica tra le Biotecnologie e la Bioeconomia	Dott. Piero Bellofiore	10/04/2017	DSC-UniNa

Density Functional Theory	Prof. Carlo Adamo	09/06/2017	DSC-UniNa
Using ab-initio methods to describe ground and excited state reactivity	Dr. Ilaria Ciofini	31/10/2017	DSC-UniNa
Chain Shuttling Polymerization – A Powerful Tool for the Design of Multiblock Polymers	Prof. Philippe Zinck	20/02/2018	DSC-UniNa

DSC-UniNa = Dept. of Chemical Sciences – University of Naples Federico II

3) Attended Integration Exams (for candidates not graduated in Chemical Science):

Title	Professor	Date
-	-	-

4) Visiting periods in Institutions different from the University of Naples Federico II:

Host Institution	Country	Start Date	End Date
University of Madison-Wisconsin	USA	01/07/2018	30/09/2018

5) Publications (include submitted and in preparation):

- Yu, Y.; Busico, V.; Budzelaar, P. H. M.; Vittoria, A.; Cipullo, R. Of Poisons and Antidotes in Polypropylene Catalysis. *Angew. Chemie Int. Ed.* **2016**, *55* (30), 8590–8594.

- Vittoria, A.; Meppelder, A.; Friederichs, N.; Busico, V.; Cipullo, R. Demystifying Ziegler–Natta Catalysts: The Origin of Stereoselectivity. *ACS Catal.* **2017**, *7* (7), 4509–4518.

- Zaccaria, F.; Vittoria, A.; Correa, A.; Ehm, C.; Budzelaar, P. H. M.; Busico, V.; Cipullo, R. Internal Donors in Ziegler-Natta Systems: Is Reduction by AlR3 a Requirement for Donor Clean-Up? *ChemCatChem* **2018**, *10* (5), 984–988.

- Vittoria, A.; Busico, V.; Cannavacciuolo, F. D.; Cipullo, R. Molecular Kinetic Study of "Chain Shuttling" Olefin Copolymerization. *ACS Catal.* **2018**, *8* (6), 5051–5061.

- Cipullo, R.; Vittoria, A.; Busico, V. Assignment of Regioirregular Sequences in the 13C NMR Spectrum of Syndiotactic Polypropylene. *Polymers (Basel).* **2018**, *10* (8), 863

- Ehm, C.; Vittoria, A.; Goryunov, G. P.; Kulyabin, P. S.; Budzelaar, P. H. M.; Voskoboynikov, A. Z.; Busico, V.; Uborsky, D. V; Cipullo, R. Connection of Stereoselectivity, Regioselectivity, and Molecular Weight Capability in *rac*-R′$_2$Si(2-Me-4-R-Indenyl)$_2$ZrCl$_2$ Type Catalysts. *Macromolecules* **2018**.

- Cipullo, R.*; Busico, V.; Vittoria, A. *Stereoselectivity of regioirregular 2,1 insertion in Ziegler-Natta propene polymerization catalysis*. To be submitted.

- Vittoria, A; Busico, V.; Cipullo, R.* *A HTE protocol for regioselectivity measurements in Ziegler-Natta propene polymerization catalysis*. To be submitted.

- Cipullo, R.*; Meppelder, A.; Friederichs, N.; Busico, V.; Vittoria, A. *Demystifying Ziegler-Natta catalysts: Regioselectivity and Hydrogen Response*. To be submitted.

6) Attended congresses/workshops/summer schools:

- *Dutch Polymer Institute Research Training Course in Polyolefins Block 1. Chemistry / Catalysis / Polymer Microstructure – Advanced Module,* Sorrento (I), June 2016.

- Poster presentation (selected among the best-10) at the *4th Blue Sky Conference on Catalytic Olefin Polymerization*, Sorrento (I), July 2016.

- Invited speaker at the *11th Advances in Polyolefins* conference, Santa Rosa, California (USA), September 2017.

Acknowledgements